
Cell polarisation in geometry

The PAR protein system as a paradigmatic model for pattern formation

Clara Raphaela Gebele



München 2020

Cell polarisation in geometry

The PAR protein system as a paradigmatic model for pattern formation

Clara Raphaela Gebele

Dissertation

an der Fakultät für Physik
der Ludwig-Maximilians-Universität München

vorgelegt von

Clara Raphaela Gebele

aus Regensburg

München, den 15. April 2020

Erstgutachter: Prof. Dr. Erwin Frey

Zweitgutachterin: Prof. Dr. Karen Alim

Tag der mündlichen Prüfung: 28. Mai 2020

Zusammenfassung

(Summary in German)

Intrazelluläre Musterbildung steuert lebenswichtige Funktionen in Prokaryoten und Eukaryoten, wie zum Beispiel Zellteilung und -differenzierung. Muster adaptieren die Zellgeometrie und können zellulären Prozessen eine Orientierung verleihen. Das PAR(-titioning defective)-Proteinsystem, ein Masse-erhaltendes Reaktions-Diffusions System, das in verschiedenen Zelltypen auftritt, wird seit Jahrzehnten im Nematoden *Caenorhabditis elegans* (*C. elegans*) untersucht. Im Zygoten definiert eine polarisierte Verteilung von zwei Gruppen der PARs die zukünftige Vorder- und Rückseite. Diese leitet die erste asymmetrische Zellteilung ein. Einige Fragen blieben bisher im Bezug auf das PAR- und auch allgemeiner im Bezug auf generell musterbildende Proteinsystemen, offen. Die vorliegende Arbeit beschäftigt sich daher mit folgenden Fragen: Wie kann das PAR-System eine polarisierte Verteilung erzeugen und wie wird gewährleistet, dass sich die Polarisierung entlang der langen Zellachse ausrichtet? Wie genau interagiert das Proteinsystem mit der Zellgeometrie? Lassen sich allgemeiner Mechanismen erkennen, die der Musterbildung in unterschiedlichen Zelltypen mit verschiedenen Geometrien zugrunde liegen? Um diese Fragen zu beantworten, habe ich mich vorwiegend auf das PAR-System konzentriert. Basierend auf bekannten bimolekularen Reaktionen formulierte ich ein Reaktions-Diffusions Modell in Geometrie. Insbesondere beschränkte ich mich nicht auf ein eindimensionales Membran-System, wie in bisherigen Modellen angewandt, sondern berücksichtigte die volle zytosolische Dynamik in realistischer Geometrie. Mit Hilfe von Stabilitätsanalysen in verschiedenen Geometrien konnte ich effizient die Bereiche der Musterbildung identifizieren und unter Verwendung der Finiten Elemente Methode die volle Dynamik und den Endzustand der Musterbildung erfassen. Zusammenfassend ergaben sich folgende Mechanismen zur Ausbildung der Polarisierung und der Selektion der Polarisationsachse: Erstens ist das lokale Verhältnis von Membranoberfläche zu zytosolischem Volumen ein entscheidender geometrischer Faktor für die initiale Ausrichtung von Proteinmustern. Zweitens wird die Wirkung dieses geometrischen Faktors maßgeblich von der Bindefähigkeit diffundierender Proteine beeinflusst. Die Diffusionslänge eines binde-inaktiven Zustands im Verhältnis zur Zellgröße ist daher ausschlaggebend für die anfängliche Musterausrichtung. Drittens kann ein zytosolisches Reservoir an aktiven Proteinen dem Effekt eines inaktiven Zustandes entgegenwirken. Viertens ist die endgültige Orientierung des Musters an eine Flussminimierung gekoppelt. Aus der Flussminimierung folgt für das PAR-System eine Minimierung des Grenzübergangs zwischen verschiedenen Proteindomänen auf der Membran. Dies gewährleistet eine robuste Langachsenpolarisierung im prolat-sphäroiden Zygoten. Allgemein lässt sich Folgendes aus der Arbeit schließen: Die Verfügbarkeit von Proteinen für Reaktionen auf der Membran wird durch die Geometrie und die zytosolischen Prozesse diktiert und beeinflusst daher die Musterbildung. Selbst wenn wegen schneller zytosolischer Diffusion ein System wohl-gemischt erscheint, sollte daher die volle zytosolische Dynamik und die Geometrie in Betracht gezogen werden.

Summary

Intracellular pattern formation in prokaryotic as well as eukaryotic cells guides processes essential for life such as cell division and differentiation. These protein patterns may also adapt to and alter with a cell's geometry.

The PAR(-titioning defective) system, a conserved protein system which is prevalent in many different cell types, has been well studied in the nematode *Caenorhabditis elegans* (*C. elegans*) in the past decades. There is experimental evidence that the conserved PAR reaction-diffusion system can establish and maintain a polarised distribution of two groups of proteins along the long axis of the worm's zygote. This polarisation of two subgroups of the PAR proteins, aPARs (anterior) and pPARs (posterior), then defines future front and back cells and guides the first cell division.

There are several open questions regarding the PAR and, more generally, other protein pattern forming system. The following ones specifically guided the research during my doctoral studies: How can the PAR protein system polarise so robustly and how does it select the long axis for its polarisation alignment? In that sense, what is the role of the reaction-network alone and how does it in detail interact with geometry? On a more general level, what is the role of geometric cues for protein pattern formation and alignment? Are there reoccurring reaction themes which underly pattern formation in different cell types?

To answer these questions, I focused on the PAR system in the first place. Based on known bimolecular reactions, I formulated a reaction-diffusion model in prolate spheroidal geometry, the natural geometry of the *C. elegans* zygote. In particular, I fully accounted for the cytosolic dynamics in contrast to previous, reduced models. Using mathematical tools (linear stability analysis in bounded geometries) and extensive simulations (Finite Element Method) in two- and three-dimensional geometries for the PAR protein model I have identified several distinct mechanisms for polarity axis selection: First, the local ratio of membrane surface to cytosolic volume is the main geometric cue that determines the initial alignment of a polarisation within cellular geometry; Second, the decisive parameter for geometry sensing through the cytosolic proteins' motility is the ratio between the diffusive length of an inactive protein state to cell length. Third, by altering protein numbers I found that a reservoir of active proteins counteracts this phosphorylated state. Fourth, simulating the full three-dimensional geometry is crucial for uncovering another principle for the selection of the final polarisation axis: the length of the aPAR-pPAR interface on the membrane is always minimised. This process is mediated by flux minimisation and ensures robust long-axis polarisation in the zygote.

With the in depth study of the PAR system and its comparison to other protein reaction-diffusion systems my work provides one building block towards a general understanding of intracellular protein pattern formation and its interaction with geometry: While recruitment enhances concentrations especially in regions of high curvature, mutual antagonism between different protein species promotes highest detachment rates in these regions. Furthermore, the availability for membrane reactions can be influenced strongly by the local cytosolic protein concentrations and dynamics

in the cytosol. For example, on the one hand an inactive phase in the cytosol after detachment can hinder local recycling and thus alter curvature effects. On the other hand, the effect of an inactive phase of proteins can be diminished by large cytosolic pools of active proteins. Furthermore, one can conclude that protein fluxes between membrane and cytosol highly impact pattern formation and location. This emphasises the importance of analysing models accounting for the full membrane-cytosol coupling and the cytosolic dynamics, even when it seems well mixed.

Outline for the reader of this thesis

The work presented in this thesis aims to shed light on self-organised protein pattern formation in specific (cellular) geometries. An in depth study of the PAR system, as a paradigmatic system for protein patterning, is provided. To put several pieces of the puzzle together the work divides into the following chapters:

1 Introduction to pattern formation and cell shape

This introductory chapter presents the background for biological pattern formation. It starts with a general and a historic introduction to the research field. Then, it introduces common themes of protein reaction-diffusion networks. In the end of the chapter, heuristic ideas how protein reaction-diffusion systems interact with the cellular geometry are presented.

2 Cell polarisation by the PAR protein system

Detailed background is given on cell polarisation by the PAR reaction-diffusion system in *Caneorhabditis elegans* (*C. elegans*). As the Min system is a thoroughly studied system from which I also learned during my doctoral studies, and which I compared to the PAR system, an overview on pole to pole oscillations in *Escherichia coli* (*E. coli*) is also provided.

3 Reaction-diffusion systems in geometry

This chapter provides a mathematical framework for reaction-diffusion systems in specific geometries. It starts with historically well known mathematical tools, which I acquired during my studies, and continues with the extension to spatial systems, which are very recent and ongoing research. A linear stability analysis of some toy reaction-diffusion systems is provided to exemplify how geometry is sensed and that the spatially extended cytosol is non-negligible for membrane patterning.

4 Geometric cues stabilise long-axis polarisation by the PAR system

with Jacob Halatek, Laeschkir Würthner, and Erwin Frey.

This chapter integrates my main project on the PAR system. Here, I worked with *Jacob Halatek, Laeschkir Würthner* and *Erwin Frey*. We published this work in Nature Communications with the title "Geometric cues stabilise long-axis polarisation of PAR protein patterns in *C. elegans*". The main findings can be summarised as follows: In the *C. elegans* embryo, (anterior) aPAR and (posterior) pPAR proteins are key to polarity maintenance. Which factors determine the selection of the polarity axis is an open question. In my publication in Nature Communications a reaction-diffusion model in realistic cell geometry is formulated. It is shown that long-axis polarisation is promoted by cytosolic dephosphorylation at onset of patterning from an initial uniform concentration. Its steady state is determined by a dynamic minimisation of the length of the aPAR-pPAR interface. This interface minimisation is driven by flux minimisation.

5 *In vivo* measurements of PAR membrane diffusion

In this chapter my work in the lab at the KITP in Santa Barbara is presented. Here, I was part of a summer school organised by *Boris Shraiman* and supervised by *Natan*

Goehring and *Lars Hubatsch*. We measured PAR membrane diffusion coefficients *in vivo*. The chapter introduces the methods used (highly inclined and laminated optical sheet (HILO) imaging, single-molecule tracking, and then calculation of diffusion constants by the mean-squared displacement). It is shown how the results were obtained. The results on PAR-3 and PAR-6 diffusion are presented and discussed.

6 Conclusion, discussion and outlook

Conclusions from this work are drawn and ideas for future theoretical as well as experimental projects are outlined.

Contents

| | | |
|----------|--|-----------|
| 1 | Introduction to pattern formation and cell shape | 1 |
| 1.1 | General background | 1 |
| 1.1.1 | Cellular pattern formation | 1 |
| 1.1.2 | Protein pattern formation and cell shape | 2 |
| 1.2 | Motivation and heuristic ideas | 4 |
| 1.2.1 | Reaction modules for intracellular pattern formation | 4 |
| 1.2.2 | The idea behind the interaction between membrane reactions and geometry | 6 |
| 2 | Cell polarisation by the PAR protein system | 9 |
| 2.1 | Cell polarisation | 9 |
| 2.1.1 | The history of PAR-titoning defective proteins in <i>C. elegans</i> | 9 |
| 2.1.2 | PAR polarisation across different cell types | 10 |
| 2.1.3 | Detailed chemical interactions for polarisation by PAR proteins | 10 |
| 2.1.4 | Establishment and maintenance of PAR polarisation | 10 |
| 2.2 | For comparison: pole to pole oscillations in <i>E. coli</i> | 13 |
| 3 | Reaction-diffusion systems in geometry | 15 |
| 3.1 | Turing's computational framework for pattern forming systems | 15 |
| 3.1.1 | Two-component system in one dimension | 16 |
| 3.2 | Reaction-diffusion systems with mass conservation in cellular geometry | 17 |
| 3.2.1 | Mass conservation | 18 |
| 3.2.2 | Rapid-mixing assumption | 18 |
| 3.2.3 | Simple one-dimensional model for PAR polarity in <i>C. elegans</i> | 19 |
| 3.2.4 | Break-down of rapid-mixing assumption | 20 |
| 3.3 | Reaction-diffusion systems in cellular geometry | 22 |
| 3.3.1 | Linear stability analysis in rectangular geometry | 23 |
| 3.3.2 | Ellipsoidal cell geometry | 26 |
| 3.3.3 | Linear stability analysis in elliptical geometry | 27 |
| 3.3.4 | Recruitment in elliptical geometry | 31 |
| 3.3.5 | Mutual antagonism in elliptical geometry | 34 |
| 3.4 | Conclusion of linear stability analysis in geometry | 37 |
| 4 | Geometric cues stabilise long-axis polarisation by the PAR system | 39 |
| 4.1 | Abstract | 39 |
| 4.2 | Introduction | 40 |
| 4.3 | Results | 43 |
| 4.3.1 | Model | 43 |

| | | |
|----------|---|-----------|
| 4.3.2 | Dephosphorylation plays a key role for axis determination . . . | 44 |
| 4.3.3 | Growth rates of long versus short-axis polarisation | 46 |
| 4.3.4 | Cytosolic reactivation length is crucial for axis selection | 47 |
| 4.3.5 | Role of phosphorylation rates | 48 |
| 4.3.6 | Axis selection depends on relative protein densities | 50 |
| 4.3.7 | Role of interface length in three-dimensional cell geometry . . . | 51 |
| 4.4 | Discussion | 54 |
| 4.5 | Methods | 56 |
| 4.5.1 | Model | 56 |
| 4.5.2 | Cytosolic dynamics | 56 |
| 4.5.3 | Membrane dynamics | 56 |
| 4.5.4 | Reactive boundary conditions | 57 |
| 4.5.5 | Mass conservation | 57 |
| 4.5.6 | Linear Stability Analysis | 58 |
| 4.5.7 | Reaction-diffusion equations in elliptical geometry | 58 |
| 4.5.8 | Finite Element Simulations (FEM) | 60 |
| 4.5.9 | Setup for FEM simulations | 60 |
| 4.5.10 | The critical reactivation rate | 60 |
| 4.5.11 | FEM simulations for 3d system | 61 |
| 4.6 | Tables for the main sections | 63 |
| 4.7 | Supplementary Information | 65 |
| 4.7.1 | Stimulus-induced polarisation and transient polarisation alignment | 65 |
| 4.7.2 | Total and relative protein numbers | 67 |
| 4.7.3 | Planar geometry: the characteristic length scale does not select the axis | 67 |
| 4.7.4 | Membrane-to-bulk ratio for ellipses and prolate spheroids | 69 |
| 4.7.5 | The role of interface length for the selection of the polarity axis | 70 |
| 4.7.6 | Minimisation of the average net cytosolic protein flux onto the membrane explains interface minimisation | 73 |
| 4.7.7 | Cytosolic fluxes depend on the cytosolic diffusion and dictate the transition time from short to long axis polarisation | 74 |
| 4.7.8 | Time scales for the formation of cell polarisation | 75 |
| 4.8 | Supplementary Tables | 78 |
| 5 | <i>In vivo</i> measurements of PAR membrane diffusion | 83 |
| 5.1 | Motivation and background | 83 |
| 5.1.1 | Theory and experiment | 83 |
| 5.1.2 | Methods to measure PAR protein motilities | 83 |
| 5.1.3 | Motivation for experiments | 84 |
| 5.2 | Experimental procedure | 84 |
| 5.2.1 | Preparation of embryos | 84 |
| 5.2.2 | Imaging using HILO | 85 |
| 5.2.3 | Single-molecule tracking to obtain mean-squared displacement. . | 86 |

| | | |
|----------|--|------------|
| 5.2.4 | Simulations to test against artefacts | 87 |
| 5.3 | Results | 88 |
| 5.3.1 | Diffusion constant measurements of PAR-3 and PAR-6 | 88 |
| 5.3.2 | Seemingly abnormal diffusion and limitations by image resolution | 89 |
| 5.3.3 | Selection for PAR-3 clusters by decreased light sensitivity | 90 |
| 5.4 | Conclusion and discussion | 91 |
| 6 | Conclusion, discussion and outlook | 93 |
| 6.1 | Conclusion and discussion | 93 |
| 6.1.1 | Summary and conclusion of the main results | 93 |
| 6.1.2 | Discussion of the PAR system compared to the Min protein system | 94 |
| 6.2 | Theoretical outlook | 95 |
| 6.2.1 | Details in the PAR reaction-diffusion model | 96 |
| 6.2.2 | Interaction with mechanical and hydrodynamic mechanisms | 97 |
| 6.2.3 | The PAR reaction-diffusion system in a deforming geometry | 97 |
| 6.2.4 | Flux and interface minimisation | 98 |
| 6.3 | Experimental outlook | 98 |
| 6.3.1 | Suggestions for experiments | 98 |
| | Bibliography | 101 |
| | Acknowledgements | 111 |

*[...] can thinking and feeling emerge from patterns of activity in different sorts of substrate?
Organic, electronic, or otherwise?*

— Andrew Hodges, PHYSICIST, in memorial of Alan Turing

Chapter 1

Introduction to pattern formation and cell shape

1.1 General background

1.1.1 Cellular pattern formation

Patterns are beautiful for the human eye, and they are even more useful for living organisms. In a world without patterns, a uniform everything, life would not exist. Patterns are not only observed in large formats such as in flocks of birds, or in the fur of zebra, but also cells organise themselves in patterns and hidden intracellular patterns fulfill important tasks (for illustration see **Fig. 1.1**).

The fascination with and the investigation of cellular patterns has a long history: One of the first milestones was set by Hans Driesch (1867-1941), German biologist and master experimenter, who showed that animals can develop from a "[...] patternless single cell, rather than growing from a microscopic, preformed version of the adult body[...]" [1]. Nowadays it is known that protein pattern formation guides the growth and healing of tissues. Furthermore, it is important for cell differentiation, it breaks down during the progression of cancer [2], and last but not least it determines the location of cell division in many prokaryotes and eukaryotes.

However, how patterns can grow in a self-organised manner - meaning without guiding cues - is an actual and thrilling research question. Since systems which form patterns in a self-organised manner include non-linear interactions, the mathematical techniques to investigate such systems were not yet developed far enough in the nineteenth century. Even now, with the help of powerful computers the dynamics of non-linear systems is still challenging to describe and grasp. Non-linear partial differential equations, which are used to describe pattern forming systems, are most of the times hard to solve. Despite of this complexity, research is shedding more and more light on cellular pattern formation on the experimental as well as the theoretical side. *In vivo* and *in vitro* experimental techniques have advanced from basic genetic variation by cultivation to very controllable techniques such as CRISPR/cas-9 genetic manipulation [7]. Furthermore, minimal synthetic cell units have been developed [8, 9] and are still in progress. Also the highly complex research field of non-linear dynamics is steadily growing [10–13].

Going from simpler to higher complexities has proven useful. Simple models paired with basic experiments in the most controllable single cell model organisms help to

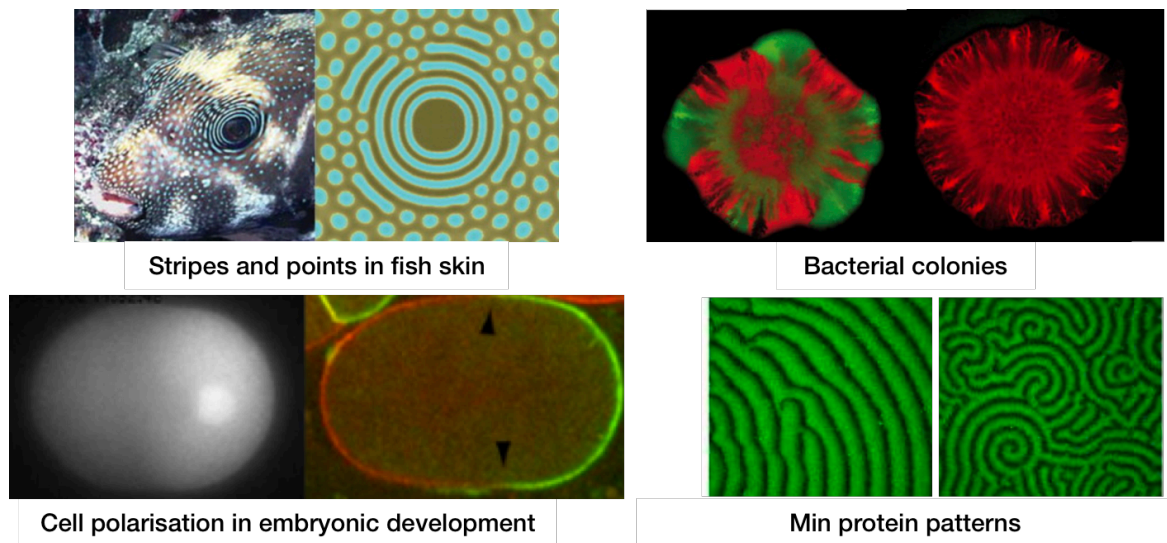


Figure 1.1 Patterns created by cells and proteins. Points and stripes on fish skin, image adopted from [3]; Bacterial colonies in different formations, image adopted from Weber et al [4]; PAR polarisation [5]; *In vitro* Min protein patterns, image adopted from [6].

gain insight on the role of pattern formation in life processes. Among the controllable and well studied eukaryotic model organisms are the *C. elegans* worm (especially its zygote), the fruit fly *Drosophila melanogaster* and the yeast *Saccharomyces cerevisiae*, and among the prokaryotic examples are culturable bacteria like *Escherichia coli* and *Bacillus subtilis*. While a first milestone for the mathematical pattern formation toolbox was already published in 1952 by Alan Turing [14], the time was not ready for Turing's deep understanding of pattern formation then. His work later became more famous when Gierer and Meinhard in 1972 [15] published theoretical models where they were inspired by gene-regulation and used Turing's framework. Also experimental methods were developed some years later. In 1980 Christiane Nüsslein-Volhard and Eric Wieschaus published their work on systematic searches for embryonic mutants where they could identify spatial organisation of specific genes and corresponding proteins [16]. In 1988 protein gradients became evident to guide the embryonic development of *Drosophila melanogaster* [17] and soon also work on *C. elegans* progressed strongly .

1.1.2 Protein pattern formation and cell shape

Not only patterns guide cells, but also cell shape guides patterns [18, 19]. The shape of cells of different type varies significantly. There are elongated neurons with axon and cell body [20], polygonal cells within epithelial sheets [21], irregularly shaped and adaptive migrating cells [22], as well as near perfectly spheroidal cells such as budding yeast [23–25]. As cells come along in different shapes, their internal protein systems adapt to their different cytoplasmic volume and membrane curvature. It is therefore appealing to ask, how does the shape influence a protein pattern? How is the pattern influenced within the shape (cellular cytosol) and on its boundaries (cellular

membrane)? More concretely, is the resulting protein pattern in a prolate spheroidal *C. elegans* embryo in its single cell state different from that of a squeezed embryo with, for example, oblate spheroidal geometry? Cell internal protein patterns have to align in some specific way with cell shape. This implies, if there is no external cue for alignment, signaling proteins need to sense geometry. And even if there is an external trigger, a robust patterning system would by itself align patterns within cell shape. However, it is known from several signaling protein systems, e.g. Min, PAR and Cdc42-Bem1 system, that proteins react and diffuse freely throughout cells [26]. How is the geometry sensed by signalling proteins? And how is an orientation within cellular geometry found by patterning proteins?

There is experimental evidence that pattern forming protein systems adapt to cell shape and some of them are even able to exhibit a plethora of different beautiful patterns, which also depend on the geometry they are allowed to spread in [19, 27]. Further complication arises considering that within cells there are compartments with different motilities of proteins. There are membrane bound proteins with slow diffusion, filament attached proteins which might travel along or are pulled with the filament [28], nucleoid bound and clustered proteins exposed to active translocation [29, 30], and fully cytoplasmic proteins diffusing more or less rapidly [26, 31]). Signalling proteins which can diffuse within cellular compartments react in certain ways with one another and also with structural elements of the cell, such as the cytoskeleton or the nucleoid. Examples for cell cortex/cytoskeleton binding proteins are among the PAR proteins and the POM XYZ system in the bacterium *Myxococcus xanthus* (*M. xanthus*) can bind to the nucleoid. Altogether, there is reaction and diffusion in cellular shapes and in their sub-shapes. This combines with mechanical and hydrodynamic interactions within the cells and from their surrounding. Intriguingly, many biochemical networks of signalling proteins can form patterns without macroscopic external stimuli. To understand protein patterns forming within cells the systematic procedure is to disentangle complex systems. One approach of disentanglement is to investigate the isolated reaction-diffusion systems in simple geometries first. Therefore, the focus in this thesis lies on pattern formation by protein reaction-diffusion systems (specifically the PAR system and the Min system for comparison) in simple, mathematically feasible geometries. In order to identify and disentangle mechanisms arising from different levels of interaction, the approach is always from the simple to the more complex: Therefore, the mathematical analysis in this thesis starts with one- and two-dimensional geometries and finally ends at three-dimensional ellipsoidal geometries (see chapters ?? and 4).

Another constraint, which is appropriate for many single cell reaction-diffusion systems including PAR, Min and Cdc42 system, is mass-conservation. In this thesis the focus therefore lies on mass-conserved (protein number) reaction-diffusion systems in mathematically feasible geometries.

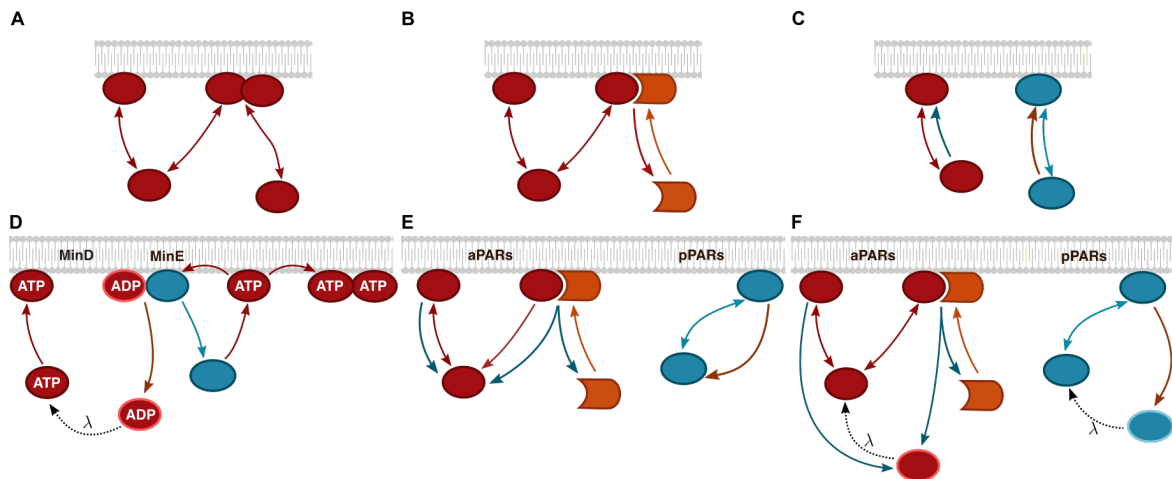


Figure 1.2 Simple reaction-schemes which promote pattern formation. (A) Self-recruitment: A protein promotes membrane-binding of its own kind possibly also by dimerisation. (B) Scaffolding: One protein species can only localise at the membrane while linking to another, membrane-bound protein. The protein species which binds directly is called "scaffold". (C) Mutual recruitment: Attachment of one protein species is enhanced in the presence of another species and vice versa (additional blue arrow for read species and red arrow for blue species). This is another example of cooperative binding among two species. (D) The "Skeleton" model for the Min protein system: MinD recruits itself to the membrane and it recruits MinE. MinE acts antagonistically as binding partner in the MinDE dimer. It induces detachment of itself and its binding partner by hydrolysis of MinD. MinD is thus inactivated (MinD-ADP) before it reactivates again at some point in the cytosol. (E) Mutual antagonism and scaffolding in a simplified version of my model for the PAR protein system: Among aPARs there is one scaffold species which binds directly to the membrane and another species which is recruited to the scaffold. Detachment of the scaffold species as well as the heterodimers is induced by pPARs. The single pPAR species binds and unbinds to and from the membrane. Its detachment is additionally induced by the aPAR heterodimer. (F) Mutual antagonism, scaffolding, and reactivation cycle in my model for the PAR protein system [32] (see also chapter 4): The same model as in (E), but additionally to the reactions there, the induced detachment of aPARs by pPARs deactivates the aPAR scaffold for binding. The scaffold reactivates with rate λ in the cytosol. The same holds for pPARs, when they are detached by aPAR antagonism they are inactive for binding at first in the cytosol.

1.2 Motivation and heuristic ideas

1.2.1 Reaction modules for intracellular pattern formation

Many reaction-diffusion systems can form patterns independently from guiding cues. The key for pattern formation in mass-conserved reaction-diffusion systems is that reactions which enhance local increase (decrease) of mass are combined with global reshuffling of mass by diffusion [13, 33]. The basic understanding of how reacting and diffusing particles are able to form patterns was set by Alan Turing. In his famous publication "The chemical basis of morphogenesis" [14] he shows a mathematical

framework to study which patterns emerge from uniformity solely due to the reaction-diffusion system. In our research group we built upon his work to not only find recurring themes in different model organisms [24, 34], but also to further develop the mathematical framework to understand how reaction-diffusion systems interact with different cellular geometries to form patterns with specific location and alignments [27, 35–37]. The mathematical framework developed by Turing and some of our extensional mathematical methods are introduced in chapter 3.

In order to gain an intuition an illustrative overview on pattern forming reaction-modules is instructive. This overview was inspired by Halatek and Frey [38] and Thompson et al [39]. Already simple protein reactions combined with diffusion can promote membrane patterns potentially. Pattern forming reactions need to be in some way non-linear, this means the output protein concentration is not directly proportional to the input concentration. Simple positive and negative feedback loops on the membrane can (some only in combination with others) create patterns on membranes.

First of all, there are different types of positive feedback loops for membrane binding. These are often called cooperative binding: a protein species binds more likely to the membrane, when there is a high protein concentration already. Multiple versions of binding cooperativity exist, here are some examples:

- Self-recruitment: A protein’s binding affinity increases with higher membrane concentration of its own species (see **Fig. 1.2 (A)**).
- Scaffolding: One protein species can bind to the membrane via another protein species - the scaffold protein (see **Fig. 1.2 (B)**).
- Mutual recruitment: Two protein species mutually promote the membrane binding of each other (see **Fig. 1.2 (C)**).

Second of all, negative feedback loops for membrane binding can promote pattern formation, i.e. the detachment likelihood of a membrane bound protein increases with the concentration of its own or another protein species. Examples of such negative feedback loops are the following:

- Antagonism: Proteins induce detachment, e.g. by inactivating the binding domain, among their locally binding neighbours or for their scaffolds (as an example see the skeleton model for the Min system in **Fig. 1.2 (D)**).
- Mutual antagonism: Different protein species inhibit the binding activity of one another (as example see the two PAR system models in **Fig. 1.2 (E)** and **(F)**).

Among the biological examples of protein reaction-diffusion networks which were investigated in our group thoroughly are the Cdc42-Bem1 system, the Min and the PAR system. All of these reaction-diffusion systems contain some of the introduced reaction modules and all are able to form patterns in a self-organised fashion.

The Cdc42-Bem1 system in budding yeast *S. cerevisiae* [24, 25, 40] contains mutual recruitment of Cdc42 and Bem1 (a simplified version is sketched in **Fig. 1.2 (C)**).

In the Min system MinD recruits itself and also recruits MinE [35]. Key for a dynamic pattern in the Min system is the combination of recruitment of MinE by MinD followed by a MinE-induced detachment (hydrolysis from ATP to ADP bound MinD) of the MinDE complex (see also a sketch of the skeleton model for the Min system in Fig. 1.2 (D)).

In the PAR system, which consists of two subgroups aPARs and pPARs (red and blue, respectively in Fig. 1.2 (E,F)) a combination of scaffolding (among aPARs: PAR-3 scaffolds the PAR-6/PKC-3 complex) and mutual detachment of aPARs by pPARs and vice versa promotes the formation of separate aPAR-pPAR-domains. Details to the PAR system follow below and in chapter 4.

Intriguingly, many pattern-forming protein systems contain some protein species which undergo a cycle from active to inactive, e.g. the PAR system undergoes a phosphorylation-dephosphorylation cycle, while in the Min and the POM XYZ system one protein species exhibits a nucleotide exchange. For illustration of the Min system see the MinD inactivation in the MinDE complex followed by detachment and uncoupling of MinE and MinD in Fig. 1.2 (D). There are valuable hints that the PAR system integrates an activation-deactivation cycle: it is known that mutual antagonism of aPARs and pPARs is mediated by phosphorylation. However, the PAR system is a conserved protein system and once phosphorylated PAR proteins need to be able to function again. Therefore, a phosphorylation-dephosphorylation cycle is reasonable. For illustration compare Fig. 1.2 (E), which does not include a phosphorylated phase, with Fig. 1.2 (F), where phosphorylated aPARs and pPARs are dephosphorylated with rate λ in the cytosol. Further discussions of this phosphorylation-dephosphorylation cycle follow in chapter 4.

1.2.2 The idea behind the interaction between membrane reactions and geometry

Alan Turing has shown that simple reaction schemes can, in combination with diffusion, give rise to patterns formation. How are such pattern promoting reactions as those introduced above related to cell shape? In turn, what is the impact of an inactive phase?

The PAR and the Min system provide some prototypical reactions which are especially interesting to study in cellular geometry. The first milestone was set by Jacob Halatek with his theoretical work on pole to pole oscillations of the Min proteins in elliptical geometry in 2012[35]. This was followed by many more studies on the Min and some attempts on the PAR system [19, 27, 36, 41–43]. This thesis includes now an in depth study of the PAR system in cellular geometry. But before coming to the biological details and the publication on the study itself in chapter 4 a heuristic but intuitive explanation between the interplay of membrane curvature and membrane reactions will be outlined.

As introduced above, two opposing but both prototypical reaction schemes are recruitment and mutual antagonism. How do patterns which are promoted by recruit-

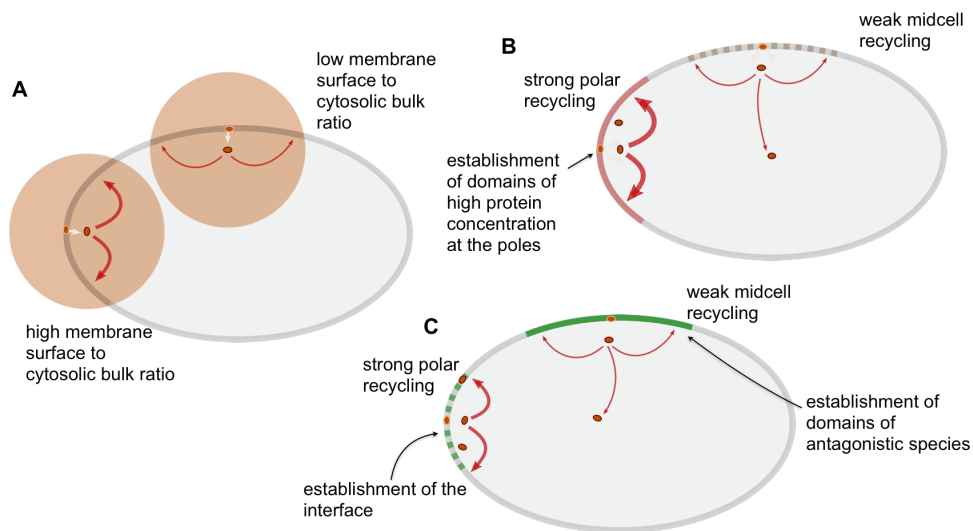


Figure 1.3 The interplay of curvature and reaction schemes. (A) Depending on the local curvature the diffusive region around a detached protein has a lower (mid-cell) or higher (poles) membrane to cytosolic bulk ratio. This implies local lower or higher recycling of proteins depending on curvature. (B) When the reaction network includes strong recruitment reactions on the membrane, simply the higher membrane-to-bulk ratio at the poles leads to higher concentrations of proteins there. (C) When two species of proteins mutually detach each other from the membrane a stronger recycling implies stronger disturbance of protein domains. Therefore, in a mutual antagonism driven system an interface between opposing species establishes at the poles, while domains of one group can form at mid-cell.

ment interact with geometry compared to patterns which are driven by antagonism? In order to keep the interactions with geometry as intuitive (and later mathematically feasible) as possible but include a variation in curvature consider an elliptical cell geometry as a first approach (see **Fig. 1.3 (A)**). The diffusive region around a recently detached protein has a lower or higher membrane to cytosolic bulk ratio depending on its detachment point. Around the cell poles there is a high membrane to cytosolic bulk ratio (high curvature) whereas around mid-cell there is a low membrane to cytosolic bulk ratio (low curvature). This implies higher or lower recycling of proteins. These different membrane to bulk ratios can affect the localisation of high and low protein concentrations depending on the reaction scheme.

At first, consider a recruitment reaction at the membrane, such as for example in **Fig. 1.2 (B)**. The high recycling rate at the highly curved poles (compared to mid-cell) promotes reattachment of proteins there. Combined with recruitment this can lead to a significant increase in the membrane concentration at the poles compared to mid-cell. For the skeleton model of the Min system the interaction of recruitment and geometry was studied by Thalmeier et al., where cooperative binding of MinD leads to strong bipolar patterns in elliptical geometry [36].

In contrast, consider two protein species which mutually induce detachment of each other. At the cell poles, when a protein is detached by its antagonistic partners it may

encounter the membrane here again with a high likelihood compared to mid-cell (see **Fig. 1.3 (C)**). This implies that most recycling of the antagonistic proteins occurs at the cell poles while a domain of a single protein species can grow with less disturbance at mid-cell. For more details on mutual antagonism in elliptical geometry see the results for my PAR model in chapter 4.

The summary of the heuristic picture above is, cellular geometry sensing by signalling proteins is conducted by sensing the local membrane surface to cytosolic bulk ratio and thus curvature. This ratio dictates the frequency with which cytosolic signalling proteins encounter the membrane locally, which then, in an interplay with the membrane binding and unbinding kinetics, determines the location of protein domains within a pattern. One can distinguish between two contrary kinetic mechanisms on the membrane which both promote pattern formation: recruitment (cooperative binding) and mutual antagonism (negative feedback) among signalling proteins. In the case of protein domain formation by recruitment most proteins bind where most (binding active) proteins encounter the membrane (see **Fig. 1.3 (B)**). Antagonism between proteins has the opposite effect on domain formation: the location where most proteins encounter the membrane is the location where antagonistic proteins induce detachment most often and thus an interface between domains forms here.

Hence, how can an inactive phase induced at detachment point alter a preferred localisation of protein domains? An inactive phase, if long enough, leads to a reshuffling of detached proteins throughout the cytosol before their binding ability is back. Therefore, it strongly impacts the localisation of concentration highs and lows on the membrane. For the case of mutual antagonism this is discussed in depth in my publication [32] printed in chapter 4.

The PAR and the Min system both contain recruitment and antagonism reactions as well as a reactivation cycle. In order to provide the biological details on this, the biochemical background of the PAR and the Min system are outlined in the following chapter.

Chapter 2

Cell polarisation by the PAR protein system

2.1 Cell polarisation

Cell polarisation names the polarised distribution of signalling proteins within cells, which guide multiple cellular processes. Among the various examples for cell polarisation are migrating cells, which reposition themselves to an outer signal, also called chemotaxis [44], the apico-basal polarisation in epithelial cells [45], and the polarised distribution of cell fate determinants in the *C. elegans* zygote, which determine future front and back [46]. Consequently, cell polarisation has to develop from and adapt to very different initial protein distributions within each cell type. The variability of cell polarisation can be exemplified as follows: while migrating cells repolarise many times again, in the embryo of the fruit fly *Drosophila melanogaster* polarisation establishes as a consequence of a maternally given source of proteins, which diffuse and degrade, and, in a *C. elegans* embryo polarisation establishes out of a near homogeneous distribution of signalling proteins. Besides *Drosophila melanogaster*, the *C. elegans* embryo is one of the most famous model organisms in which cell polarisation has been studied thoroughly. This relies on lineages which have shown to develop in an extremely controllable and reproducible fashion [47, 48]. Furthermore, the worms are easy to raise and practical to prepare in the lab. Despite of decades of investigation, open questions on the principle mechanisms of cell polarisation in the single cell embryo (zygote) remain. In the following, the biological evidence for cell polarisation by the PAR protein system in the *C. elegans* zygote is presented. Cell polarisation in the *C. elegans* zygote is introduced from its discovery to the biochemical interactions of the polarising proteins.

2.1.1 The history of PAR-titoning defective proteins in *C. elegans*

The PAR protein system was discovered for the first time in a mutant screen of *C. elegans* embryos [49]. In the early 1980s Ken Kemphues and Jim Priesst found a gene in *C. elegans*, later named *par-1*, which, when knocked out, prevents the embryo from proper cleavage. Subsequently, Kemphues and Priesst could identify six of such genes, which they called *par*-titoning defective (PAR) genes [50]. The name partitioning defective comes from the defect in partitioning important molecular players among the daughter cells in *par*-mutants [46]. The six *par* genes and the respective PAR proteins were called *par-1* through *par-6* (respective proteins PAR-1 through PAR-6). Intriguingly, the PAR proteins subdivide into two groups of proteins, the **aPARs**,

which localise at the **anterior** cortex of the embryo, and the **pPARs**, which localise in the **posterior**.

2.1.2 PAR polarisation across different cell types

Although the PAR system was discovered and mostly studied in *C. elegans*, evidence for its existence and function in other cells exist. One might even state that it is an evolutionary developed template, which functions in very diverse cell types. For example, PARs reoccurs in *Drosophila melanogaster* and in epithelial tissue [46]. Specifically, the scaffold protein PAR-3 has even been identified to function in a variety of polarised cellular events such as asymmetric cell division, epithelial polarisation, directional cell migration and neuronal specification [46]. It appears that, while some some functions of the PAR proteins have developed differently in different cell types, they keep their mutual antagonistic reactions to establish polarised protein distributions. Thereby PARs provide diverse cells an orientation.

2.1.3 Detailed chemical interactions for polarisation by PAR proteins

As outlined above, in the past decades molecular analyses revealed that the PAR proteins carry functional domains which are important for intracellular signalling [50] (see also chapter 4): PAR-1 and PAR-4 have serine/threonine kinase domains, i.e. they induce phosphorylation of serine/threonine proteins; PAR-3 and PAR-6 carry PDZ domains, i.e. they have binding domains which help complex building and membrane binding, as we explain below with their binding domains PAR-3 acts as a scaffold while PAR-6 acts as a linker; PKC-3 is an atypical protein kinase C, i.e. it phosphorylates other proteins; PAR-2 has a “ring finger” zinc binding domain, i.e. can act as ligase to colocalise PAR-1 in the cortex/membrane. Since it is not fully understood which and how the PAR proteins connect to the membrane or to the cell cortex, we will in the following use membrane and cortex binding interchangeably.

2.1.4 Establishment and maintenance of PAR polarisation

How is PAR polarisation established and how do these proteins maintain a polarised distribution on the cell membrane in *C. elegans* so robustly? Overall, this thesis focusses on the self-organised maintenance phase of PAR polarisation as a big step towards understanding robust development. For completeness, here we outline experimental evidence for interactions of the PAR protein reaction-diffusion system with cellular mechanical and hydrodynamical units such as the cell cortex and centrosome localisation.

After fertilisation the polarised distribution of PARs establishes out of a near homogeneous concentration. Before polarisation establishment the aPAR proteins cover the membrane uniformly and diffuse through the cytosol, while the pPAR proteins

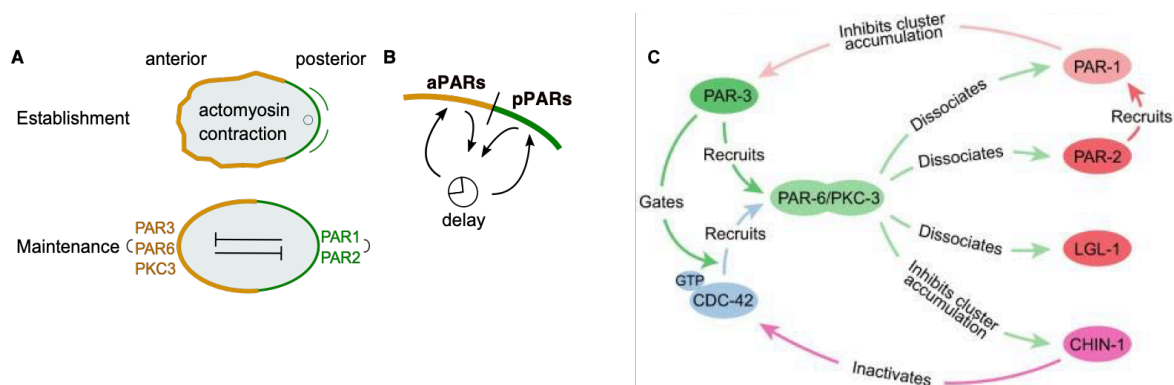


Figure 2.1 PAR polarisation (A) Top: Sketch of the establishment phase with the male centrosome close to the posterior pole and actomyosin contraction towards the anterior. Bottom: PAR domains maintain polarity by mutual antagonism/phosphorylation (arrows). aPARs are summarised on the left and pPARs on the right. **(B)** Sketch of a binding delay due to a cytosolic inactive phase. **(C)** Overview of detailed and partially redundant interactions of polarity determinants in *C. elegans* adopted from [51].

remain in the cytoplasm. In a healthy embryo the first symmetry breaking events are two redundant triggers (see also **Fig. 2.1 (A)**, top):

The first cue arises from the just entered male centrosome which often localises close to the posterior pole. The male centrosome seems to inhibit actomyosin contraction in the nearby cortex. This effect has been partially explained by a decreased concentration of ECT-2 [52, 53], which is a guanine exchange factor (GEF), and its effect on a decrease in activity of RhoA. RhoA increases the actomyosin contractility, therefore a decrease in RhoA activity close to the centrosome leads to a loss in actomyosin contraction [5]. In total, decreased actomyosin contraction close to the male centrosome on one side and regular contraction on the opposing cortical region leads to a net contraction towards the end of the embryo far away from the male centrosome. This enriches the membrane bound aPAR proteins there [54, 55]. The flow pulling aPARs towards one side in the embryo has been reported recently to be supported by clustering of PAR-3 and interactions with membrane binding Cdc42 [55, 56].

The second cue is associated with microtubules which connect the cortex with the male centrosome. The microtubule seem to protect pPARs (PAR-1 and PAR-2) from the exclusion by the aPAR kinase PKC-3 [5, 57], such that a pPAR domain can grow.

Despite of these interactions with the actomyosin network, polarisation is quite robust against disruption of the actomyosin network [31] while polarisation fails to develop in PAR mutants. This strong dependence on the PAR reaction-diffusion network relies on the mutual inhibition of aPARs versus pPARs for membrane binding rather than on any sorting mechanisms associated with the cell cortex [26, 58]. Currently, the biochemical reactions helping establishment and irreplaceable for maintaining cell polarisation can be summarised as follows (see also **Fig. 2.1 (A)**, bottom): All PAR proteins diffuse freely throughout the cell un- as well as polarised [26]. The scaffold protein PAR-3 [59, 60] directly binds to the membrane, PAR-6, also called adapter

| Regulating protein | substrate | regulatory mechanism | effect |
|--------------------|-----------|-------------------------------------|------------|
| PKC-3 | PAR-1 | phosphorylation | inhibition |
| PKC-3 | PAR-2 | phosphorylation | inhibition |
| PKC-3 | LGL-1 | phosphorylation | inhibition |
| PAR-1 | PAR-3 | phosphorylation | inhibition |
| LGL | PKC-3 | genetic and biochemical interaction | inhibition |
| PAR-2 | PAR-3 | unknown | inhibition |

Table 2.1 Evidence of mutual antagonism mainly by phosphorylation among PAR proteins, adapted from [51, 58].

protein, binds to PAR-3 and to the kinase PKC-3 [61, 62]. The kinase PKC-3 forms complexes with PAR-6 and can only this way connect to PAR-3 on the membrane [55, 63–65]. Only the kinase phosphorylates pPARs, i.e. unbinds them from the membrane. Therefore, only complexes of all three aPARs can bind to the membrane and unbind pPARs there by phosphorylation. Among pPARs there is the kinase PAR-1, which phosphorylates PAR-3 [57] and the RING-protein PAR-2, where it is known that both are required to exclude aPARs from the posterior membrane region [62, 66–69]. Furthermore, it has been shown that also LGL-1 can displace aPARs [58, 68, 70]. Also pPARs exclude aPARs from the membrane by phosphorylation. For a detailed network of interactions with some redundant mechanisms here we refer to Lang et al. [51] and an overview in **Fig. 2.1 (C)**.

Since mutual phosphorylation is evidently crucial for PAR polarisation and PAR proteins are conserved in number, i.e. there is no source of new proteins, one can assume a cytosolic dephosphorylation reaction (see also **Fig. 2.1 (B)**). This would enhance the proteins' binding affinity again. So far the cytoplasmic phosphorylated phase followed after detachment has not been studied. Typically, such a dephosphorylation process is regulated in cellular environment by (i) spontaneous dephosphorylation and (ii) by the cytosolic phosphatase concentration. In chapter 4 we show that, from a theoretical perspective, a cytosolic phosphorylated phase is not necessary for polarisation but it strongly affects axis alignment of polarisation in an elongated ellipsoidal (prolate spheroidal) embryo.

In summary, polarisation by the PAR protein system in *C. elegans* is needed for the cell division cycle. Current state of the art is that mechanical and hydrodynamic cues help the onset of PAR polarisation, but robust long-term polarisation is mediated by the PAR reaction-diffusion system. The main reaction module among PARs is mutual antagonism (mutual phosphorylation), while recruitment terms may also play a role. Furthermore, due to mutual inhibition by phosphorylation combined with protein number conservation, a cytosolic dephosphorylation is plausible. Up to date cellular alignment of polarisation driven by mutual antagonism has not been investigated and remains as one of the main research questions in this thesis.

2.2 For comparison: pole to pole oscillations in *E. coli*

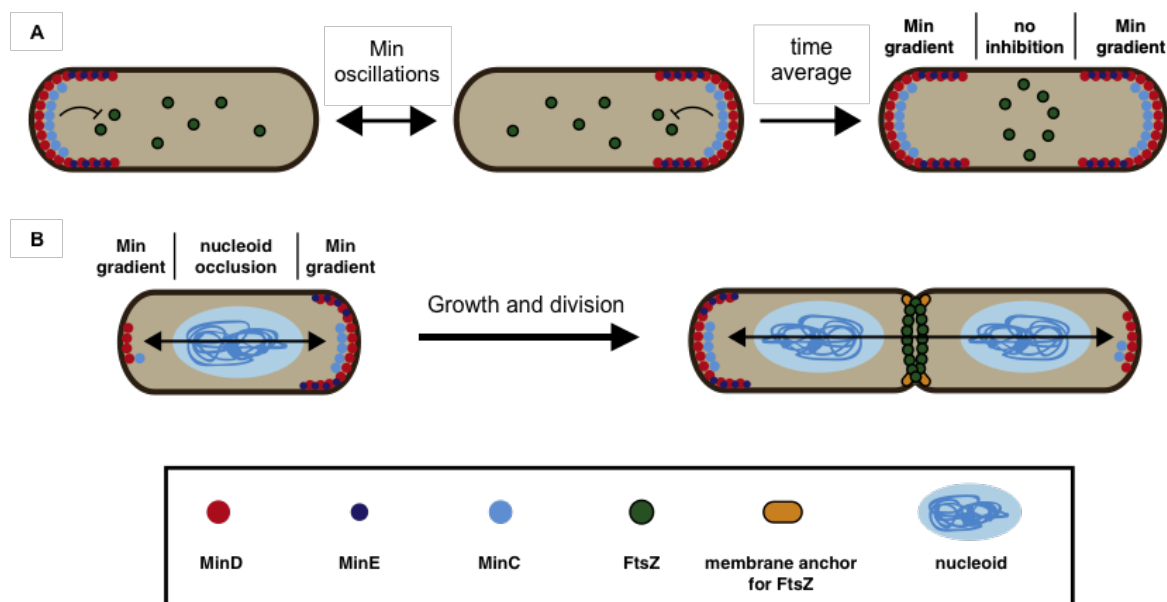


Figure 2.2 Min oscillations in *E. coli* guide cell division. Schematic adopted from [71]. **(A):** Min proteins oscillate from pole to pole, thereby exhibiting a time-averaged concentration minimum at midcell. FtsZ is inhibited by Min proteins. At first (left) FtsZ cannot polymerise on the membrane due to Min inhibition. When pole to pole oscillations have established well the minimum concentration at midcell is small enough such that FtsZ starts to assemble there. **(B):** The minimum concentration as well as the promoted FtsZ-ring formation may also be related to cell size and to an exclusion by the nucleoid.

Not only cell polarisation can guide cell division. When bacteria divide into two equal daughter cells an asymmetric division such as that of the *C. elegans* embryo would be unfavourable. The daughter cells should equalise two new bacteria. In the rod-shaped bacterium *E. coli* a protein system called the Min system has been identified to solve this task. The three Min proteins MinC, MinD and MinE oscillate from pole to pole [72, 73] thereby creating a time-average minimum of their concentration at midcell, the later location for bacterial division. The minimum concentration at midcell is important for cell division, because MinC, which coexists on the membrane and follows the other Min proteins, inhibits FtsZ polymerisation. FtsZ, in turn, is a protein which assembles into a curved formation [74]. It polymerises at midcell in a ring formed shape which then is the scaffold for further processes of cytokineses. Since this Z-ring formation is coupled to a minimum concentration, a single bacterium has to grow first to reach a certain size, such that the MinC concentration is low enough [35, 72, 73]. The oscillations of Min proteins develop in a self-organised fashion [35, 43]. Min proteins react with each other, bind and unbind to and from the membrane, and diffuse throughout the bacterial cytoplasm as well as on the membrane. The reaction-diffusion dynamics of the Min proteins is understood to act as follows: MinD in its ATP-bound

form has a strong binding affinity to the membrane. Once membrane bound, it further promotes binding of more MinD to the membrane. In addition, it recruits MinE to the membrane by forming MinDE complexes. Once in a complex, however, MinE inhibits the long term membrane binding of MinDE complexes by stimulating MinD-ATPase activity. Once MinD transforms from its ATP-bound form to the ADP-bound form, the MinDE complex dissociated into the cytosol [75]. Back in the cytosol MinD and MinE diffuse freely and MinD at some point exchanges nucleotides again from the inactive ADP-bound state to binding active ATP-bound form. Both, theoretical [27, 35] and experimental [19, 43] work provide evidence that this combination of first recruitment, then induced unbinding and release in the cytosol promotes oscillations, which, however, also depend on cell geometry. In other than rod-shaped geometry the Min system can exhibit a plethora of different patterns, from chaotic creation and destruction of concentration minima and maxima to standing and travelling wave patterns and spirals.

The Min system is of particular interest to compare with the PAR system as it was studied thoroughly *in vivo*, *in vitro*, and *in silico* [13, 19, 27, 35, 36, 38, 43, 76, 77]. *In vitro* investigation of the full PAR system was not possible until today, since some of the proteins cluster so strong that they could not be purified. As this work sheds light on the PAR reaction-diffusion system as a stand-alone in geometry, i.e. without other cellular cues, the system can be compared to the *in vitro*, and *in silico* Min system. The detailed discussion is postponed to chapter 6 in section 6.1.2.

The definition of genius is taking the complex and making it simple.

— Albert Einstein, THEORETICAL PHYSICIST

Chapter 3

Reaction-diffusion systems in geometry

This chapter presents the mathematical toolbox used for the investigation of protein pattern formation in cellular geometry. It includes examples of minimal reaction-diffusion networks in simple geometries and linear stability analysis of these. The mathematical toolbox presented here has grown over more than half a century and is still work in progress in our research group at LS Frey.

For a thorough understanding of intracellular protein pattern formation it is instructive to disentangle the protein reaction-diffusion system fully from cellular mechanical and hydrodynamic interactions. This chapter provides the theoretical background to analyse a reaction-diffusion system step by step. The chapter starts with an introduction of Alan Turing's pioneering framework for reaction-diffusion systems as pattern forming systems [14]. Then, mass- (i.e. global protein number) conservation is considered as an additional constraint which is present in many cellular reaction-diffusion systems. This constraint is added to the framework of linear stability analysis, first disregarding geometry. Then some downsides of neglecting geometry are presented. Afterwards, linear stability analysis in rectangular and elliptical geometry are discussed. Exemplifying this, two prototypical reaction-diffusion systems are introduced and a linear stability analysis is performed in elliptical geometry.

3.1 Turing's computational framework for pattern forming systems

How patterns can form from the interplay of reaction and diffusion has been studied with great effort over the past decades initiating also some scientific debates [38]. Alan Turing was the first one who had the idea that actually diffusion could promote pattern formation in an initially homogeneous reaction network. In 1952 he published his seminal work "The chemical basis of morphogenesis" [14], where he explains how a homogeneous concentration of morphogens (where he meant the reacting particles, e.g. signalling proteins) can grow into patterns of high and low concentration of these morphogens, and such a pattern can develop solely due to a small "irregularity" [14, 78]. The type of "irregularity" (perturbation) does not matter. Any irregularity will escalate as long as the system has nonlinear reactions.

Turing proposed a genius framework to investigate if an original uniform concentration of particles could develop patterned concentrations in a self-organised manner. Precisely, a network of diffusing and reacting particles could form some alternation of

low and high concentration when an initially uniform concentration was only randomly, small perturbed. In terms of a mathematical formulation, Turing proposed to first seek for a uniform solution to the ensuing reaction-diffusion equations. Then, a small perturbation, which is described in form of a Fourier decomposition in space and time, is added to the uniform solution. Such a perturbation, $\delta c(t, x)$, to a uniform concentration, \bar{c} , can be described with $\delta c(t, x) \propto e^{\sigma_q t} \cdot \cos(qx)$. This ansatz allows to calculate growth rates, σ_q , for each spacial Fourier mode. Precisely, in a linear regime around the uniform state those Fourier modes with $\sigma_q > 0$ grow away from the uniform concentration. They grow, at least initially, into the pattern resembling the mode with wave number q . Other modes with $\sigma_q < 0$ decay, i.e. do not lead to pattern formation for small perturbations. Not for nothing, an instability where the homogeneous solution is stable against homogeneous perturbations but unstable against some patterns (modes), i.e. the corresponding growth rate $\sigma_q > 0$, is up to now called "Turing instability".

A good summary in words was stated by Zhou et al [79]: "A Turing instability, first proposed by Turing (1952), occurs when a steady state, stable in the absence of diffusion, becomes unstable when diffusion is present, and patterns are temporally stable and spatially heterogeneous solutions of the reaction-diffusion system".

Intriguingly, with this mathematical framework Turing could show that a reaction network in a stable uniform state can become unstable simply under the presence of diffusion. For a two component system on a one-dimensional line he could further show that for such an instability to happen one diffusion constant has to be much greater than the other [14, 78].

3.1.1 Two-component system in one dimension

To provide a first mathematically detailed example, consider a two component system with component m and c diffusing on a one-dimensional line with length L . The ensuing reaction-diffusion equations read:

$$\partial_t m = D_{\text{mem}} \nabla^2 m + f_m(m, c) \quad (3.1)$$

and

$$\partial_t c = D_{\text{cyt}} \nabla^2 c + f_c(m, c) \quad (3.2)$$

where D_{mem} and D_{cyt} are the respective diffusion constants, ∇^2 is the Laplace operator, which in this one-dimensional case is just ∂_x^2 , and $f_{m/c}$ are the reaction terms of m and c , respectively. They may depend on both components. One searches for the simplest homogeneous solution at first, in order to check its stability later. For homogeneous solutions the time and space derivatives equalise zero. This results in the following system of (non-linear) equations:

$$f_m(\bar{m}, \bar{c}) = 0 \quad (3.3)$$

$$f_c(\bar{m}, \bar{c}) = 0. \quad (3.4)$$

The graphical solutions to these two equations are also called nullclines. Expressing the incremental time and space dependent perturbations, $\delta c(t, x)$ and $\delta m(t, x)$, in terms of Fourier modes, $\delta c/\delta m(t, x) \propto e^{\sigma t} \cdot \cos(qx)$ with $q = n\pi/L$ for this system of length L , the nonlinear reaction-diffusion system is then linearised around the homogeneous solution (\bar{m}, \bar{c}) resulting in the linear system of equations for $(m, c)(t, x) = (\bar{m} + \delta m, \bar{c} + \delta c)$. This reads in vector notation:

$$\partial_t \begin{pmatrix} \delta m \\ \delta c \end{pmatrix} = \sigma_n \begin{pmatrix} \delta m \\ \delta c \end{pmatrix} = J_n \cdot \begin{pmatrix} \delta m \\ \delta c \end{pmatrix}, \quad (3.5)$$

with

$$J_n = \begin{pmatrix} \partial_m f_m|_{(\bar{m}, \bar{c})} - D_{\text{mem}}(\frac{\pi n}{L})^2 & \partial_c f_c|_{(\bar{m}, \bar{c})} \\ -\partial_m f_m|_{(\bar{m}, \bar{c})} & -\partial_c f_m|_{(\bar{m}, \bar{c})} - D_{\text{cyt}}(\frac{\pi n}{L})^2 \end{pmatrix}. \quad (3.6)$$

Here we have employed that for the homogeneous solutions (\bar{m}, \bar{c}) $f_{m/c}|_{(\bar{m}, \bar{c})} = 0$ and $\partial_t(\bar{m}, \bar{c}) = 0$. This system of equations then can be solved as usual for σ_n by setting the determinant $\det(J_n) = 0$. The final expression for σ as a function of n (or of q) is called dispersion relation. The study of the dispersion relation predicts if patterns can emerge and which patterns (modes) grow strongest in a linear regime around the homogeneous solution. The dispersion relation, however, does not explain the pattern formation far away from the homogeneous fixed point.

3.2 Reaction-diffusion systems with mass conservation in cellular geometry

For pattern formation within cells, the reacting and diffusing particles are typically proteins which cycle between membrane-bound and cytosolic states. In the following membrane components are denoted as m and cytosolic components as c . Such protein species may also have further conformational states, such as an inactive state, e.g. denoted as c^* , in which they do not react or bind. Within one cell division cycle, a time scale on which also the cell size is approximately fixed, many protein systems are conserved in their number. In this section, we extend the just introduced mathematical framework in order to appropriately comprise mass-conserved protein reaction-diffusion systems in specific, fixed geometries.

3.2.1 Mass conservation

Analogously to the two-component system above, consider now a total number of S species, where each species consists of two components: one on the membrane (boundary) denoted with m_i , and one in the cytosol (bulk) denoted with c_i , where $i \in \{1, \dots, S\}$. Reactions and diffusion are confined to some general cellular geometry, so in mathematical terms all proteins are confined to a geometric space Ω (bulk) and its respective boundary $\partial\Omega$ (membrane). A general set of reaction-diffusion equations can then be stated. It reads on the membrane ($\partial\Omega$)

$$\partial_t m_i = D_{m_i} \nabla_{\parallel}^2 m_i + f_{m_i}(m_1, \dots, m_S; c_1, \dots, c_S), \quad (3.7)$$

where ∇_{\parallel}^2 is the Laplacian operator confined to the boundary, $\partial\Omega$, and D_{m_i} is the diffusion constant of the i^{th} species on the boundary. In the cytosol (Ω) the reaction-diffusion equations then read

$$\partial_t c_i = D_{c_i} \nabla^2 c_i + f_{c_i}(m_1, \dots, m_S; c_1, \dots, c_S), \quad (3.8)$$

with the bulk Laplacian operator ∇^2 and the cytosolic diffusion constant D_{c_i} for the i^{th} species in the cytosol. One finds that due to mass conservation $f_{c_i} = -f_{m_i} := f_i$. Furthermore, mass conservation limits the set of solutions to the reaction-diffusion system. Let us assume that mass is conserved and the total number of proteins is therefore the conserved number N_i for each species $i \in \{1, \dots, S\}$. N_i then can be calculated by integrating the space-dependent cytoplasmic concentrations and membrane concentrations over Ω and $\partial\Omega$, respectively:

$$N_i = \int_{\Omega} c_i + \int_{\partial\Omega} m_i \quad (3.9)$$

where \int_{Ω} and $\int_{\partial\Omega}$ denote integrals over the interior and the boundary. For a reaction-diffusion system in a specific geometry the boundary conditions also have to be considered. However, before integrating specific geometries into the mathematical framework, an often used trick to circumvent the geometry is introduced. It is then shown that this trick often veils parts of the pattern forming system.

3.2.2 Rapid-mixing assumption

Many examples of functional intracellular patterns are formed on the membrane of cells. Cytosolic diffusion constants are typically one to two orders higher than membrane diffusion constants, which implies that protein gradients on the membrane are significantly sharper than in the cytosol. Typical numbers for the cytoplasmic diffusion are of the order of $10\mu\text{m}^2\text{s}^{-1}$ while membrane bound diffusion typically ranges from 0.01 to $0.1\mu\text{m}^2\text{s}^{-1}$, i.e. for a generic system as described above $D_{c_i} \gg D_{m_i}$ [26, 38, 80, 81]. This finding makes a rapid-mixing assumption plausible, since the motility of cytosolic proteins is so high that the cytosolic concentrations could supposedly be assumed homogeneous for all times [82]. Then, within the well-mixed cellular bulk

volume, Ω , $c_i(x, t) = c_i(t)$. Thus, the mass-conservation can be simplified:

$$N_i = \int_{\Omega} c_i(x, t) + \int_{\partial\Omega} m_i(x, t) = c_i(t) \cdot \Omega + \int_{\partial\Omega} m_i(x, t) \quad (3.10)$$

Defining the global average $\langle m_i(x, t) \rangle = \langle m_i \rangle(t) = \int_{\partial\Omega} m_i(x, t)/\Omega$ and substituting $c_i(t) = N_i/\Omega - \int_{\partial\Omega} m_i(x, t)/\Omega$ into the reaction-diffusion equations, one finds integro membrane equations which only depend on the membrane concentrations and their spatial averages:

$$\partial_t m_i = D_{m_i} \nabla_{\parallel}^2 m_i + f_i(m_1, \dots, m_S; \langle m_1 \rangle, \dots, \langle m_S \rangle). \quad (3.11)$$

3.2.3 Simple one-dimensional model for PAR polarity in *C. elegans*

Several models [31, 83, 84] for cell polarisation in the *C. elegans* embryo are based on mutual antagonism on the membrane and rapid mixing in the cytosol. An often cited one-dimensional model was at first introduced and used by Goehring et al [31]. Trong et al. provide an analysis of the simplified model in mathematical detail [82]. The model is based on the mutual antagonistic detachment of two protein species, called *A*, for aPARs, and *P*, for pPARs. The model geometry is a one-dimensional line of length L . This is connected to a pool of cytoplasmic proteins which are conserved in number, but which are well mixed. Thus, each protein can exchange between a uniform cytoplasmic pool and a membrane bound state. Following the notation above, the ensuing integro reaction-diffusion equations read:

$$\partial_t m_A = D_{m_A} \partial_x^2 m_A + k_{\text{on},A} (\rho_{0,A} - \psi \cdot \langle m_A \rangle) - k_{\text{off},A} m_A - k_{AP} m_P^\beta m_A, \quad (3.12)$$

$$\partial_t m_P = D_{m_P} \partial_x^2 m_P + k_{\text{on},P} (\rho_{0,P} - \psi \cdot \langle m_P \rangle) - k_{\text{off},P} m_P - k_{PA} m_A^\alpha m_P. \quad (3.13)$$

Here $\psi = \int_{\partial\Omega} / \Omega$ is the membrane-surface-to-cytosolic-bulk ratio as introduced in 3.2.2, $k_{\text{off},A/P}, k_{\text{on},A/P}$ are de- and attachment rates of *A* and *P*, respectively, and the terms $k_{AP} m_P^\beta m_A$ and $k_{PA} m_A^\alpha m_P$ with $\alpha, \beta \in \mathbb{N}$ capture the mutual antagonistic detachment. In order to find polarised patterns, it is required to have either $\alpha \geq 2$ while $\beta \geq 1$ or vice versa [82]. It was shown that protein numbers as well as antagonistic rates have to balance such that polarised patterns can stabilise. In the region where these antagonistic forces balance three uniform solutions, two stable and one unstable, exist. As shown in [82] for this model and mathematically discussed in detail in [34], this bistability promotes the redistribution of proteins into a polarised (or other) pattern due to the two stable fronts. While this model was useful to define and analyse mutual antagonism as a polarity inducing reaction module, it veils any geometry dependence. In the following it will be discussed why finite diffusion and the cellular geometry can influence membrane patterns.

3.2.4 Break-down of rapid-mixing assumption

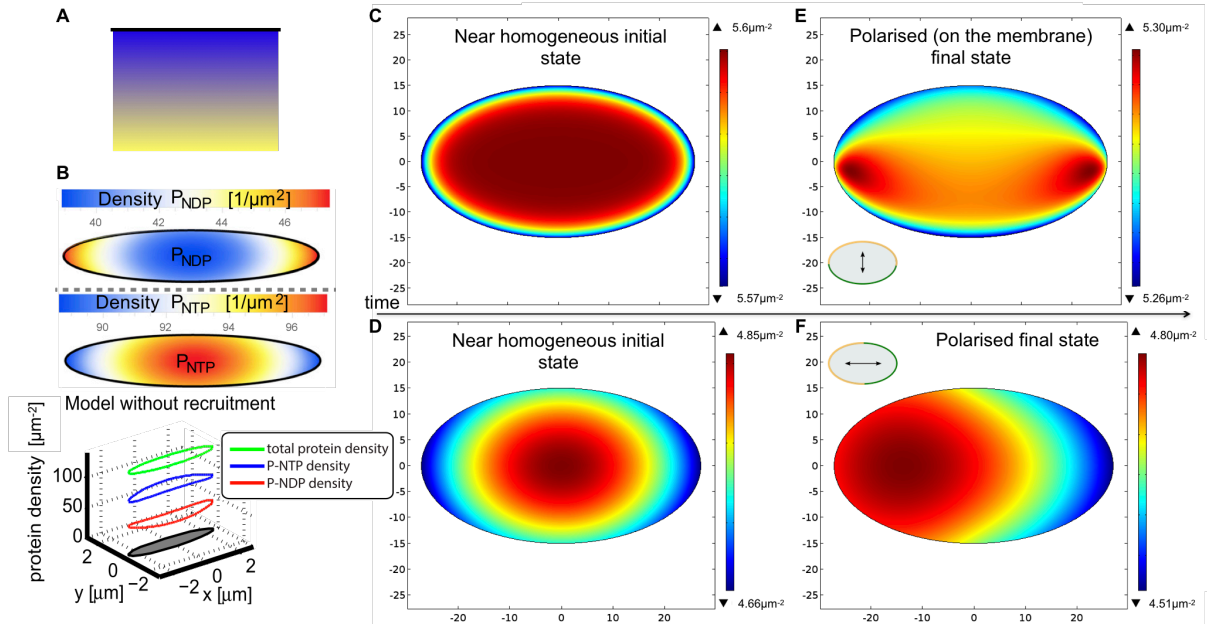


Figure 3.1 Cytosolic gradients corresponding to different membrane patterns (A) Sketch of a rectangular bulk geometry with the membrane at the top. Proteins become inactive for binding on the membrane, and diffuse through the cytosol where they are reactivated. Therefore, the concentration of active proteins gradients from a very low concentration of active proteins close to the membrane (deep blue) to high concentrations in the cytosolic bulk far away from the membrane (light yellow). **(B)** Cytosolic concentration profiles for MinD-ATP (active, top) and ADP (inactive, middle) are shown in colour code. The respective MinD membrane concentrations are plotted below. The elliptical geometry combined with inactivation on the membrane leads to a bipolar pattern even without recruitment in the membrane reaction terms. Image adapted from [36]. **(C-F)** Cytosolic gradients of active PAR-3 (A_1 for my PAR model which is discussed in detail in chapter 4) in initial near homogeneous **(C,D)**, and final short- **(E)** or long- **(F)** axis polarised state. Cytosolic diffusion is set to $D_{\text{cytosol}} = 30\mu\text{m}^2\text{s}^{-1} \approx 100 \cdot D_{\text{membrane}}$. The initial near homogeneous state exhibits a thin layer in front of the membrane with a lack of active proteins, when reactivation is fast ($\lambda = 10\text{s}^{-1}$, shown in **(C,E)**). In the corresponding final short-axis polarised state shown in **(E)** one can see the cytosolic recycling of proteins in the polar regions. This is different for slow reactivation ($\lambda = 0.05\text{s}^{-1}$, **(D,F)**). The penetration depth of inactivated proteins is deeper and most reactivation of proteins happens in the mid-cell regime. The corresponding final state shown in **(F)** is long-axis polarised.

Despite of typically fast cytosolic diffusion cytosolic gradients have been observed in different model organisms such as *D. melanogaster* and *C. elegans*. A rapid-mixing assumption and its mathematical implications are, due to their mathematical feasibility, a reasonable start for the investigation of pattern formation on cellular membranes. However, the question arises, if the limitations which are inherent to an analysis of a model with a rapid-mixing assumption are still acceptable in the context of analysing

the interaction with the specific geometry. In case of different cytoplasmic states, which can originate at the membrane, a completely homogeneous steady state does not necessarily exist. For example, when considering an inactive state of proteins which is induced at the membrane and reactivation occurs in the cytosol. In this case, the membrane is like a source of inactive proteins which degrade back to their active state while diffusing through the cytosol. For an illustration see **Fig. 3.1 (A)**: here, proteins become inactive for binding on the membrane. They diffuse through the cytosol where they reactivate according to some constant rate. Thus, the concentration gradients from a very low concentration of active proteins close to the membrane to a high concentration in the cytosolic bulk far away from the membrane. Mathematically this is described as a source degradation problem [15]. Cell biological examples for such a scenario are proteins which undergo a nucleotide exchange from NDP- to NTP-bound, such as MinD in *E. coli* [35] and Cdc42 in yeast [85], and also phosphorylation on the membrane such as among PAR [86] counteracted with dephosphorylation in the cytosol. Cytoplasmic gradients not only exhibit themselves a (weak) pattern but are able to influence membrane patterns significantly [32, 35, 36], see also chapter 4. Pattern formation on cellular membranes is driven by positive or/and negative feedback loops of membrane attachment (including dimerisation) and detachment [38, 39]. The attachment and detachment processes, however, depend on the availability of proteins which can attach or detach. This, in turn, depends also on cytosolic gradients. For illustration see **Fig. 3.1 (B)**: Thalmeier et al. could show that in an elliptical geometry the concentration profiles of binding inactive (top) and active (middle) MinD are associated with a bipolar MinD pattern on the membrane (bottom). Furthermore, in this work (see **Fig. 3.1 (C-F)** and for details see also chapter 4), it is shown that in two-dimensional elliptical geometry the depth of an inactive layer of proteins strongly impacts pattern formation and alignment. This depth can either be altered by the speed of cytosolic diffusion, i.e. how far does an inactive protein travel given some time interval, or by the time until reactivation, i.e. for how long can it travel before it is active for binding again. In **Fig. 3.1 (C,E)** reactivation is fast which results in a vanishingly thin inactive layer. For pattern formation based on mutually antagonistic membrane detachment and inactivation, this results into the highest recycling rates of proteins at the cell poles and thus a short-axis polarised cell. For slow reactivation as in **Fig. 3.1 (D,F)** the system exhibits a much wider inactive layer. In the polar regions least active proteins are available, so recycling is weakest here and strongest at mid-cell. Thus, in equilibrium the pattern is long-axis polarised.

For a pattern in equilibrium all attachment and detachment processes balance, however, the number of proteins that can attach locally depends on the local cytosolic concentrations, which, in turn, are affected by cytosolic gradients. Another example to support this understanding was given a recent work of Halatek et al. [13]. There the role of the cytosolic bulk height above a planar membrane was analysed. Intriguingly, the bulk height could be identified as a control parameter that enables a transformation of the system from a turbulent behaviour to the emergence of spiral patterns and to travelling waves. See also **Fig. 3.2**.

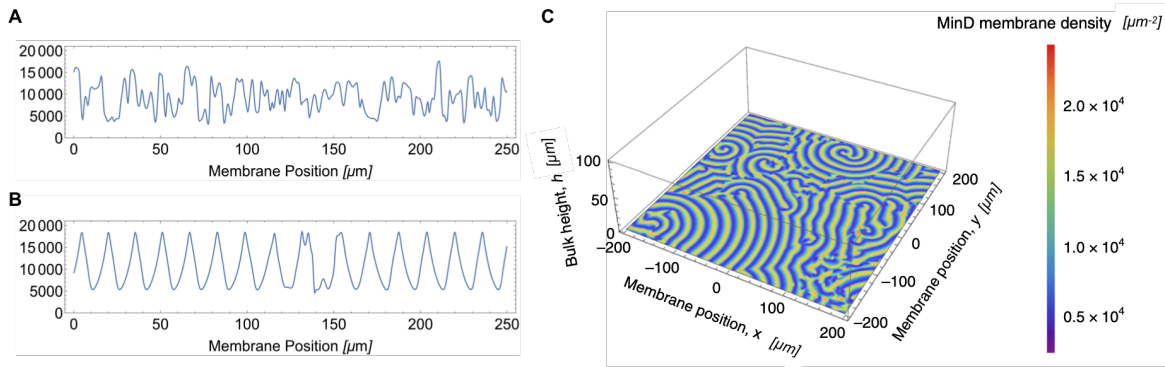


Figure 3.2 Halatek et al showed that for the Min system the bulk height above a membrane is a control parameter for patterns. While for low bulk heights there is chaotic behaviour, see (A), above a critical bulk height standing and travelling waves emerge. Adapted from [13].

All examples show that a rapid-mixing assumption makes it impossible to understand cytosolic gradients, and that it fully veils the impact of gradients on membrane patterning. More importantly, it fully masks the geometry. A geometry that covers features of cell shapes must include variations in local membrane surface to cytosolic bulk ratio. A rapid mixing assumption makes this obsolete.

In summary one can conclude two things from the examples above: (i) a cellular geometry is sensed by its membrane-to-bulk ratio and (ii) cytosolic processes influence membrane patterning, because they mediate between membrane reactions and the cellular geometry.

3.3 Reaction-diffusion systems in cellular geometry

The above examples point out that in cells not only the reactions of diffusing proteins, but also the specific cellular geometry influences where high and low protein concentrations equilibrate. As outlined above, a cellular geometry is always accompanied by varying membrane-to-bulk ratios throughout the system and passes these on to the reaction-diffusion system. In terms of the mathematical description, the geometry implies boundary conditions which any patterning solution must obey. The mathematical framework to analyse reaction-diffusion systems, as developed by Alan Turing, can be extended to reaction-diffusion systems in two- and three-dimensional geometry. Already a stability analysis in rectangular and circular geometry (see also [87]) can be insightful. In order to learn about axis alignment of patterns the implementation of a model in elliptical geometry is a helpful starting point (see also [32, 35]). However, the extension of linear stability analysis in geometry with bulk (cytosol) and boundary (membrane) brings some difficulties: Accounting for the shape and dimension of each, bulk and boundary, two distinct sets of reaction-diffusion systems are present, one set of equations for the membrane and one set for the cytosolic bulk. In order to perform the linear stability a common set of eigenfunctions (modes) must be found at first. In the following sections examples of simplified models in different geometries are used to

illustrate how to find common eigenfunctions of bulk and boundary, and then perform linear stability analysis in geometry.

3.3.1 Linear stability analysis in rectangular geometry

In this section, the mathematical tools for a linear stability analysis of one protein species which cycles between binding active and inactive state, e.g. an NTP- and an NDP-bound state, or a phosphorylated versus a dephosphorylated state, is provided in a rectangular geometry. Detachment on the membrane is accompanied by inactivation. The focus in this section lies on the boundary conditions between membrane and cytosol. These can imply cytosolic gradients, as will be shown.

The rectangular system is defined in the following manner: At $y = H$ and for $0 \leq x \leq L$ the membrane builds one boundary above the rectangular cytosolic bulk of height H . Thus, the rectangular cytosolic bulk fills the area $0 \leq x \leq L$, $0 \leq y < H$ (see also **Fig. 3.1 (A)**). At $y = H$, i.e. at the membrane, reactive boundary conditions, also called Robin boundary condition, are defined. In contrast, at the non-membrane boundaries, at $x = 0, L$, reflective boundary conditions are used.

3.3.1a Bulk diffusion and activation

In the bulk proteins diffuse with diffusion constant D_{cyt} . Furthermore, proteins which have turned inactive on the membrane can reactivate with rate λ in the cytosol. This is described mathematically by a diffusion-degradation (reactivation) problem:

$$\partial_t c^* = -\lambda c^* + D_{\text{cyt}} (\partial_x^2 + \partial_y^2) c^*. \quad (3.14)$$

An ansatz to find eigenfunctions to the bulk-diffusion with reactivation is to separate space and time coordinates. Using the ansatz $c^* \propto e^{\sigma t} X(x) Y(y)$ for some inactive cytosolic component c^* and plugging this into equation 3.14 one obtains:

$$\frac{\sigma + \lambda}{D_{\text{cyt}}} = \underbrace{\frac{\partial_x^2 X(x)}{X(x)}}_{=: A_x} + \underbrace{\frac{\partial_y^2 Y(y)}{Y(y)}}_{=: A_y}. \quad (3.15)$$

Since the left hand side is constant in the coordinates x and y one finds

$$\partial_x^2 X(x) = A_x X(x) \quad (3.16)$$

$$\partial_y^2 Y(y) = A_y Y(y), \quad (3.17)$$

where A_x and A_y are constant. Due to reflective boundary conditions at $x = 0, L$, i.e. $\partial_x X(x)|_{x=0,L} = 0$, the solution for $X(x)$ must be a cosine and A_x must fulfil $\sqrt{A_x} = i(\frac{2\pi}{L}n)$:

$$X(x) \propto \cos\left(\frac{2\pi}{L}nx\right). \quad (3.18)$$

From equation 3.15 one finds the expression for A_y :

$$A_y = \frac{\sigma + \lambda}{D_{\text{cyt}}} - A_x \quad (3.19)$$

$$= \frac{\sigma + \lambda}{D_{\text{cyt}}} + \left(\frac{2\pi}{L}n\right)^2. \quad (3.20)$$

From 3.17 we know that the solution for $Y(y)$ must be a linear combination of $e^{\sqrt{A_y}y}$ and $e^{-\sqrt{A_y}y}$. Together with zero flux at $y = 0$ we find

$$Y(y) \propto \cosh\left(\sqrt{\frac{\sigma + \lambda}{D_{\text{cyt}}} + \left(\frac{2\pi}{L}n\right)^2}y\right) \quad (3.21)$$

Thus the overall solution reads:

$$c^*(x, y, t) = \sum_n C_n e^{\sigma_n t} \cos\left(\frac{2\pi}{L}nx\right) \cosh\left(\sqrt{\frac{\sigma_n + \lambda}{D_{\text{cyt}}} + \left(\frac{2\pi}{L}n\right)^2}y\right) \quad (3.22)$$

Here, the growth rate σ_n is denoted with an n in order to link it with the corresponding spatial eigenmode.

Similarly, one finds the bulk solutions of the total (active and inactive) protein concentration $c_{\text{tot}} = c^*(x, y, t) + c(x, y, t)$:

$$c_{\text{tot}}(x, y, t) = c^*(x, y, t) + c(x, y, t) = \sum_n A_n e^{\sigma_n t} \cos\left(\frac{2\pi}{L}nx\right) \cosh\left(\sqrt{\frac{\sigma_n}{D_{\text{cyt}}} + \left(\frac{2\pi}{L}n\right)^2}y\right), \quad (3.23)$$

$$c(x, y, t) = \sum_n A_n e^{\sigma_n t} \cos\left(\frac{2\pi}{L}nx\right) \times \left(\cosh\left(\sqrt{\frac{\sigma_n}{D_{\text{cyt}}} + \left(\frac{2\pi}{L}n\right)^2}y\right) - \frac{\alpha_n}{A_n} \cosh\left(\sqrt{\frac{\sigma_n + \lambda}{D_{\text{cyt}}} + \left(\frac{2\pi}{L}n\right)^2}y\right) \right). \quad (3.24)$$

3.3.1b Boundary conditions

To perform the linear stability analysis with the above found bulk eigenfunctions the reactive boundary conditions need to be expressed in terms of the eigenfunctions. As an example, consider the boundary flux of the inactive concentration c^* . The flux of

inactive proteins into the cytosol must equalise the reactions on the membrane which drive proteins off and turn them inactive:

$$D_{\text{cyt}} \nabla_N c^*|_{y=H} = f(m, c), \quad (3.25)$$

where $f(m, c)$ are those membrane reactions which impact c^* in the cytosol locally, e.g. a membrane detachment term which arises from binding inactivation. For the total bulk concentration $c_{\text{tot}} = c^*(x, y, t) + c(x, y, t)$ reactions onto and from the membrane add up to zero. Thus, note that

$$D_{\text{cyt}} \nabla_N c_{\text{tot}}|_{y=H} = 0. \quad (3.26)$$

For the inactive component in rectangular geometry one finds an explicit coupling constant by plugging in the bulk solution:

$$\begin{aligned} D_{\text{cyt}} \nabla_N c^*|_{y=H} &= D_{\text{cyt}} \partial_y c^*|_{y=H} = D_{\text{cyt}} e^{\sigma n t} X(x) \partial_y Y(y)|_{y=H} \\ &= D_{\text{cyt}} \sqrt{\frac{\sigma + \lambda}{D_{\text{cyt}}} + \left(\frac{2\pi}{L} n\right)^2} \frac{\sinh\left(\sqrt{\frac{\sigma + \lambda}{D_{\text{cyt}}} + \left(\frac{2\pi}{L} n\right)^2} y\right)}{\cosh\left(\sqrt{\frac{\sigma + \lambda}{D_{\text{cyt}}} + \left(\frac{2\pi}{L} n\right)^2} y\right)} \\ &\quad \cdot \cosh\left(\sqrt{\frac{\sigma + \lambda}{D_{\text{cyt}}} + \left(\frac{2\pi}{L} n\right)^2} y\right) \Big|_{y=H} e^{\sigma n t} X(x) \\ &= \underbrace{D_{\text{cyt}} \sqrt{\frac{\sigma + \lambda}{D_{\text{cyt}}} + \left(\frac{2\pi}{L} n\right)^2} \tanh\left(\sqrt{\frac{\sigma + \lambda}{D_{\text{cyt}}} + \left(\frac{2\pi}{L} n\right)^2} H\right)}_{=: \mathcal{B}} c^* \Big|_{y=H} \\ &= \mathcal{B} \cdot c^*|_{y=H}. \end{aligned} \quad (3.27)$$

The coupling constant \mathcal{B} allows to linearise the reactive boundary condition. Having found the coupling constant one can linearise the reactive boundary condition and perform the linear stability analysis.

3.3.1c Stationary solutions

The stationary solutions are obtained by setting all time derivatives to zero, thereby implying $\sigma = 0$. In order to find the homogeneous solutions on the membrane consider cytosolic solutions which are homogeneous along the membrane, i.e. in x -direction. The zeroth mode in x -direction fulfils this condition. Setting $n = 0$, one can find homogeneous membrane solutions that match the cytosolic eigenfunctions with the reactive boundary conditions.

Investigating these solutions closer provides some more insight. Setting $\sigma = 0$ and $n = 0$ in the bulk solutions 3.22-3.24 shows that only the total concentration c_{tot}

is constant in the cytosol. The active and inactive components, c and c^* , include a cytosolic gradient:

$$c(x, y, t) \propto \left(1 - \frac{\alpha_0}{A_0} \cosh \left(\sqrt{\frac{\lambda}{D_{\text{cyt}}}} y \right) \right) \quad (3.28)$$

and

$$c^* \propto \cosh \left(\sqrt{\frac{\lambda}{D_{\text{cyt}}}} y \right). \quad (3.29)$$

A cytosolic gradient was expected as discussed in section 3.2.4.

3.3.1d Implication of the rectangular geometry

While the rectangular geometry does not resemble a realistic cellular geometry, it still has proven useful. Its analytical feasibility allows to investigate how the bulk to volume ratio, cytosolic gradients, and copy numbers of proteins are related to pattern formation [13, 33, 77]. However, which cellular axis is selected cannot be answered in such a geometry.

3.3.2 Ellipsoidal cell geometry

Many single-cellular organisms have a natural shape resembling a sphere or an ellipsoid. For example, the natural shape of a single cell *C. elegans* zygote resembles a prolate spheroid with approximate axis lengths $a = 27 \mu\text{m}$ and $b = 15 \mu\text{m}$. Here, a is the distance from centre to pole through a focus along the symmetry axis, also called the semi-major axis, while b is the equatorial radius of the spheroid, also called semi-minor axis. For visualisation, a rotation of an ellipse (e.g. the ellipse in **Fig. 3.3**) around the major axis would create a prolate spheroid.

One of the main goals in this thesis is to investigate how patterns of proteins form and how they thereby align with a cellular axis. An analysis of a model system in rectangular geometry does not allow any conclusions about axis selection in ellipsoidal geometry. For a detailed discussion on this see also the supplementary material of [32] in chapter 4. However, before implementing a model system resembling the real prolate spheroidal shape of a zygote it is extremely helpful to start with a two-dimensional model system for the following reasons:

- Cytosolic processes and cytosolic inhomogeneities in the protein concentrations can already be investigated in two dimensions (as shown above, this is already possible in rectangular geometry).
- In two-dimensional elliptical geometry the effect of varying membrane-to-bulk ratio (curvature) can be analysed. This obviously would not be possible in

rectangular systems. Furthermore, this does only make sense in systems which provide axes, such as an elliptical geometry. A circular geometry provides curvature but no differentiable axes.

- At the state of the art, we can perform large parameter sweeps of linear stability analysis computationally efficiently in two-dimensional elliptical geometry but not in ellipsoidal geometry.
- A three-dimensional model geometry already introduces more complex features, such as a shape and length of interfaces between protein domains in the pattern (see the results from [32] printed in chapter 4). This can veil the identification of mechanisms arising from the interplay between the membrane-to-bulk ratio and the reaction-diffusion system alone.

Therefore, the two-dimensional elliptical geometry offers just the right complexity to start an investigation of the impact of given membrane-to-bulk ratios and cytosolic processes on axis selection. Since the *C. elegans* zygote has the shape of a prolate spheroid with semi-major axis a (rotation axis) and semi-minor axis b , the two-dimensional model in elliptical geometry is implemented with the same semi-major and semi-minor axis a and b .

3.3.3 Linear stability analysis in elliptical geometry

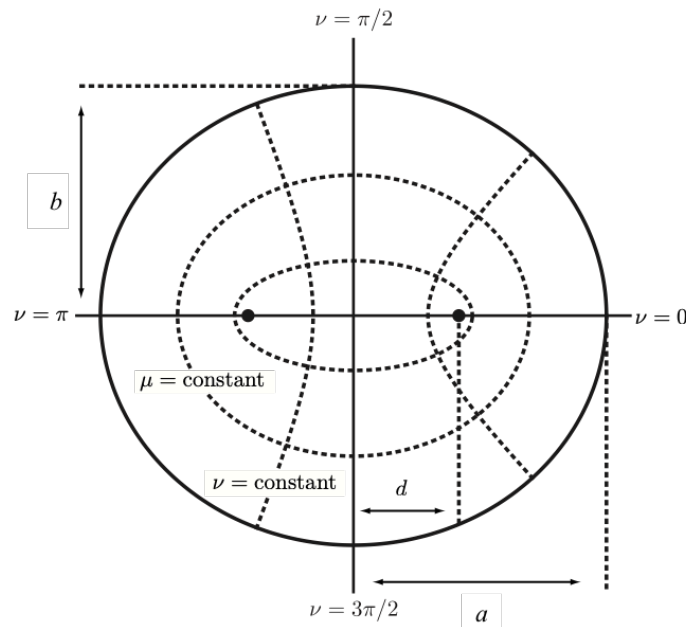


Figure 3.3 Visualisation of elliptical coordinates. Analogously to spherical coordinates $\mu > 0$ is called the 'radial' variable, $0 \leq \nu < 2\pi$ is the 'angular' variable. The elliptical eccentricity is defined $d = \sqrt{a^2 - b^2}$ with semi-major (long) axis a and semi-minor (short) axis b . Image adopted from [36].

This section presents linear stability analysis in elliptical coordinates. It hereby partially overlaps with the methods section in my publication [32] reprinted in chapter 4. This overlap is here for the readability of the sections afterwards. Then, in the following sections, the dispersion relation is approximated analytically for two minimal models, one based on recruitment and one based on antagonism (the two species model introduced in section 3.2.3). The approximated dispersion relation gives first a hint on a preferred pattern alignment.

Linear stability analysis in elliptical geometry was at first described by Halatek et al [35]. The key points how to obtain a set of joint membrane-bulk eigenfunctions in an ellipse are presented now, before they are used to approximate the dispersion relation in two minimal models.

Given orthogonal elliptical coordinates

$$x = d \cosh \mu \cos \nu, \quad (3.30)$$

$$y = d \sinh \mu \sin \nu, \quad (3.31)$$

with ‘radial’ variable $\mu > 0$, ‘angular’ variable $0 \leq \nu < 2\pi$, and elliptical eccentricity $d = \sqrt{a^2 - b^2}$ with semi-major (long) axis a and semi-minor (short) axis b (see also **Fig. 3.3**, the diffusion operator in the bulk $D_{\text{cyt}} \nabla^2$ reads:

$$D_{\text{cyt}} \frac{1}{d^2 (\sinh^2 \mu + \sin^2 \nu)} (\partial_\mu^2 + \partial_\nu^2). \quad (3.32)$$

On the boundary the diffusion operator $D_{\text{mem}} \nabla_{\parallel}^2$ acts along constant $\mu = \mu_0 = \arctan(b/a)$. It is the squared tangential derivative along the boundary and reads:

$$D_{\text{mem}} \left(- \frac{\cos \nu \sin \nu}{d (\sinh^2 \mu_0 + \sin^2 \nu)^{3/2}} \partial_\nu + \frac{1}{d^2 (\sinh^2 \mu_0 + \sin^2 \nu)} \partial_\nu^2 \right). \quad (3.33)$$

Due to these different diffusion operators the sets of reaction–diffusion equations in the bulk and on the boundary do not share the same set of canonical eigenfunctions (i.e. eigenfunction obtained from separation of variables). To overcome this problem the diffusion on the membrane can be more conveniently expressed in arclength parametrisation $s(\nu)$:

$$s(\nu) = \int_0^\nu d\tilde{\nu} \sqrt{b^2 + (a^2 - b^2) \sin^2 \tilde{\nu}}. \quad (3.34)$$

Then, the diffusion operator $D_{\text{mem}} \nabla_{\parallel}^2$ simplifies to $D_{\text{mem}} \partial_s^2$, and the eigenfunctions are obtained as

$$\Psi_{e,n}^{\text{mem}}(\mu_0, s(\nu)) = \cos \left(\frac{2\pi n}{S} s(\nu) \right), \quad (3.35)$$

$$\Psi_{o,n}^{\text{mem}}(\mu_0, s(\nu)) = \sin \left(\frac{2\pi n}{S} s(\nu) \right), \quad (3.36)$$

where $S = s(2\pi)$ is the circumference of the ellipse. The subscripts e/o denote even and odd according to their symmetry. A sketch of how these membrane eigenfunctions look like in terms of high and low concentrations is shown in **Fig. 3.4**. There it is depicted how sine and cosine functions fold around the circumference of the ellipse.

Then, the goal is to express these functions in terms of the orthogonal eigenfunctions of the bulk problem — the Mathieu functions, here denoted by $\Psi(\nu)$ and $R(\mu)$ — which are obtained as solutions of the Mathieu equations:

$$0 = \partial_\nu^2 \Psi(\nu) + [\alpha - 2q \cdot \cos(2\nu)] \Psi(\nu) \quad (3.37)$$

$$0 = \partial_\mu^2 R(\mu) - [\alpha - 2q \cdot \cosh(2\mu)] R(\mu). \quad (3.38)$$

Here, α is a constant of separation, and

$$q = -(\sigma + \lambda) \frac{d^2}{4D_{\text{cyt}}} \quad (3.39)$$

denotes a dimensionless parameter which depends on the growth rate σ and on an activation rate λ . Note that in a model without an activation cycle the parameter λ can just be set to zero. For small q , analytical approximations of the Mathieu functions can be obtained [35, 88, 89] and matched with the eigenfunctions $\Psi_{e,n}^{\text{mem}}$ and $\Psi_{o,n}^{\text{mem}}$ at the boundary, where $\mu = \mu_0$. The n^{th} even (e) or odd (o) membrane eigenfunction which is expressed in terms of a linear combination of the Mathieu functions is then the bulk-extended n^{th} even (e) or odd (o) membrane-bulk eigenfunction (mode). As the bulk eigenfunctions have an angular, $\Psi(\nu)$, and a radial, $R(\mu)$, part, the bulk-extended

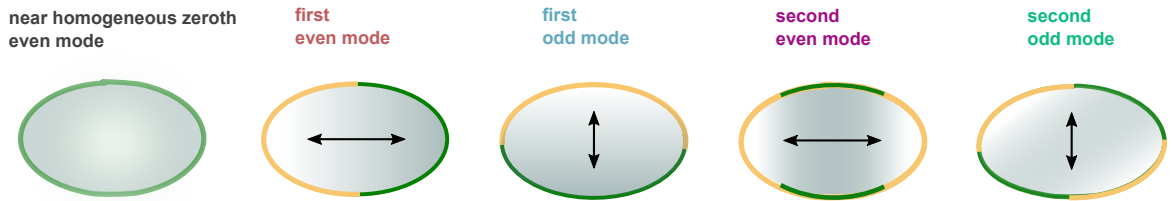


Figure 3.4 Sketch of membrane modes in elliptical geometry.

The first few even and odd membrane modes are sketched for a system with an inactive phase, i.e. $\lambda \neq 0$. For this case, the zeroth mode is non-uniform, but the membrane concentration is close to homogeneous. The first even and odd modes resemble long- and short-axis polarised concentrations.

membrane eigenfunctions result in a linear combination of these:

$$\Psi_{e,n}^{\text{mem-bulk}}(\mu, \nu, q_n) = \sum_{m=0}^{\infty} \gamma_{e,n,m} \frac{R_{e,m}(\mu, q_n)}{R_{e,m}(\mu_0, q_n)} \Psi_{e,m}(\nu, q_n), \quad (3.40)$$

$$\Psi_{o,n}^{\text{mem-bulk}}(\mu, \nu, q_n) = \sum_{m=1}^{\infty} \gamma_{o,n,m} \frac{R_{o,m}(\mu, q_n)}{R_{o,m}(\mu_0, q_n)} \Psi_{o,m}(\nu, q_n). \quad (3.41)$$

Here, $\gamma_{e/o,n,m}$ is the expansion coefficient for the membrane eigenfunctions as a linear combination of the angular and radial Matthieu functions. $\gamma_{e,n,m}$ is calculated numerically according to the integral expression given by Halatek et al [35]. Note that for $\mu = \mu_0$, i.e. a point on the boundary of the ellipse, the radial part $R(\mu)$ reduces, resulting in a μ -independent expression.

Before a linear stability analysis can be performed the boundary conditions have to be linearised. Here, another difficulty arises due to the flux operator. At the boundary the diffusive flux, which comes from the cytosol onto the membrane, equalises the reactive flux from the membrane into the cytosol. Following the notation introduced above, the corresponding equation for a general two-component system with cytosolic component c and membrane component m reads

$$D_{\text{cyt}} \nabla_N c|_{\mu=\mu_0} = f(m, c). \quad (3.42)$$

Consequently, to perform a stability analysis one needs to linearise the normal derivative ∇_N at the boundary of the ellipse. Besides a scaling factor, which arises from the differentials $d\mu$ and $d\nu$ and can be denoted as $h(\mu, \nu) = d\sqrt{\sinh^2(\mu) + \sin^2(\nu)}$, for the normal derivative one finds $\nabla_N \propto \partial_\mu$. This results in finding an adequate linearised form of

$$\nabla_N \Psi_{e,n}^{\text{mem-bulk}}|_{\mu=\mu_0} = h(\mu_0, \nu)^{-1} \sum_m^{\infty} \gamma_{e,n,m} \frac{\partial_\mu R_{e,m}(\mu, q_n)}{R_{e,m}(\mu_0, q_n)} \Psi_{e,m}(\nu, q_n), \quad (3.43)$$

for the even bulk-boundary eigenfunctions. The flux operator acting on the odd modes is expressed analogously with o instead of e in the subscript. As explicitly shown by Halatek et al [35, 41] coupling of modes in this expression can be neglected and with the help of a power series expansion and an appropriate cutoff, one finds a approximation (obtained numerically) of the normal derivative at the boundary. In the following, the approximated, linearised boundary conditions is denoted as

$$\nabla_N \Psi_{e,n}^{\text{mem-bulk}}|_{\mu=\mu_0} = \Gamma_{e,n} \Psi_{e,n}^{\text{mem}}. \quad (3.44)$$

Note that the linearised approximation of the boundary flux operator is a polynomial of $q(\sigma_n, \lambda)$. It has to be calculated explicitly for a given ellipse with semi-axis a and b . With the coupled membrane-bulk eigenfunctions to linearise the membrane equations and the linearly approximated reactive boundary conditions at hand, linear stability analysis can be performed, i.e. the growth rates for each eigenmode can be calculated.

Despite the mathematical complexity, computationally this is still an efficient procedure to gain a first insight on a preference for long- or short- axis alignment. In the following two simple reaction-diffusion models are presented in elliptical geometry.

3.3.4 Recruitment in elliptical geometry

Consider a single protein species which cycles between membrane-bound (component with concentration m) and cytosolic state (component with concentration c) in a two-dimensional elliptical geometry with long axis a and short axis b (as introduced above). Additional to some constant on- and off-kinetics with rates, k^{on} and k^{off} , the membrane-bound component recruits itself to the membrane, i.e. the reactions on the membrane include a mathematical term $k^{\text{d}} \cdot m^2 c$. Altogether, membrane reactions are described by the function $f(m, c) = k^{\text{on}} c - k^{\text{off}} m + k^{\text{d}} \cdot m^2 c$. One obtains a set of reaction-diffusion equations, where on the membrane the equation reads

$$\partial_t m = D_{\text{mem}} \nabla^2 m + f(m, c), \quad (3.45)$$

where D_{mem} is the membrane-bound diffusion constant, ∇_{\parallel}^2 the Laplace operator on the membrane as described in equation 3.33. The cytosolic dynamics is described by a pure diffusion equation:

$$\partial_t c = D_{\text{cyt}} \nabla^2 c, \quad (3.46)$$

with diffusion constant D_{cyt} . The reactive boundary conditions are

$$D_{\text{cyt}} \nabla_N c|_{\mu=\mu_0} = -h(m, c). \quad (3.47)$$

Here $h(m, c) = f(m, c)$ since there is no cytosolic reactivation.

The stationary state is obtained by

$$0 = f(\bar{m}, \bar{c}). \quad (3.48)$$

A perturbation to the stationary solution \bar{c}, \bar{m} can be expressed in elliptical coordinates. In vector form the perturbation is described with

$$\begin{pmatrix} \delta m \\ \delta c \end{pmatrix} := e^{\sigma_{e/o,n} t} \Psi_{e/o,n}(\mu, \nu) \cdot \vec{x}. \quad (3.49)$$

Following the scheme above the linearised system of this set of equations reads:

$$0 = \begin{pmatrix} \partial_t(\cdot) - \partial_m f - D_{\text{mem}} \nabla_{\parallel}^2 & -\partial_c f \\ \partial_m f & \partial_c f + D_{\text{cyt}} \nabla_N(\cdot) \end{pmatrix} \cdot \begin{pmatrix} \delta m \\ \delta c \end{pmatrix}, \quad (3.50)$$

where L is the circumference of the ellipse. The derivatives can be evaluated with

$$\nabla_{\parallel}^2 \Psi_{e/o,n} = - \left(\frac{2\pi n}{L} \right)^2 \Psi_{e/o,n}, \quad (3.51)$$

$$\partial_t e^{\sigma_{e/o,n} t} = \sigma_{e/o,n} e^{\sigma_{e/o,n} t}, \quad (3.52)$$

and

$$\nabla_N \Psi_{e/o,n} \Big|_{\mu=\mu_0} = \Gamma_{e/o,n} \Psi_{e/o,n}, \quad (3.53)$$

where in the last equation $\Gamma_{e/o,n}$ is the linearly approximated flux operator.

Plugging these equations in one finds

$$0 = \begin{pmatrix} \sigma_{e/o,n} - \partial_m f - D_{\text{mem}} \left(\frac{2\pi n}{L} \right)^2 & -\partial_c f \\ \partial_m f & \partial_c f + D_{\text{cyt}} \Gamma_{e/o,n} \end{pmatrix} \cdot \begin{pmatrix} \delta m \\ \delta c \end{pmatrix}. \quad (3.54)$$

Since $\Gamma_{e/o,n}$ is expressed as a higher order polynomial function of $q_{e/o,n} = -\sigma_{e/o,n} \frac{d^2}{4D_{\text{cyt}}}$, solving the full linearised system is left to numerical calculations. However, close to the onset of pattern formation the growth rate $\sigma_{e/o,n}$ is small. It is therefore reasonable to express the expansion of $\Gamma_{e/o,n}$ in $\sigma_{e/o,n}$ explicitly and introduce the cutoff for this expansion:

$$\Gamma_{e/o,n} := \sum_{i=0}^{\infty} \left(-\frac{d}{4D_{\text{cyt}}} \right)^i \frac{\partial_q^i \Gamma_{e/o,n} \Big|_{q=0}}{i!} \cdot \sigma_{e/o,n}^i. \quad (3.55)$$

Approximating in linear order one finds

$$\Gamma_{e/o,n} \approx \Gamma_{e/o,n} \Big|_{q=0} - \frac{d}{4D_{\text{cyt}}} \partial_q \Gamma_{e/o,n} \Big|_{q=0} \cdot \sigma_{e/o,n}. \quad (3.56)$$

This expression can be used for a first analytic estimation of the dispersion relation. Plugging the linear order of $\Gamma_{e/o,n}$ into the linearised set of equations 3.54 one finds:

$$0 = \begin{pmatrix} \sigma_{e/o,n} - \partial_m f - D_{\text{mem}} \left(\frac{2\pi n}{L} \right)^2 & -\partial_c f \\ \partial_m f & \partial_c f + D_{\text{cyt}} \Gamma_{e/o,n} \Big|_{q=0} - \frac{d}{4D_{\text{cyt}}} \partial_q \Gamma_{e/o,n} \Big|_{q=0} \cdot \sigma_{e/o,n} \end{pmatrix} \cdot \begin{pmatrix} \delta m \\ \delta c \end{pmatrix}. \quad (3.57)$$

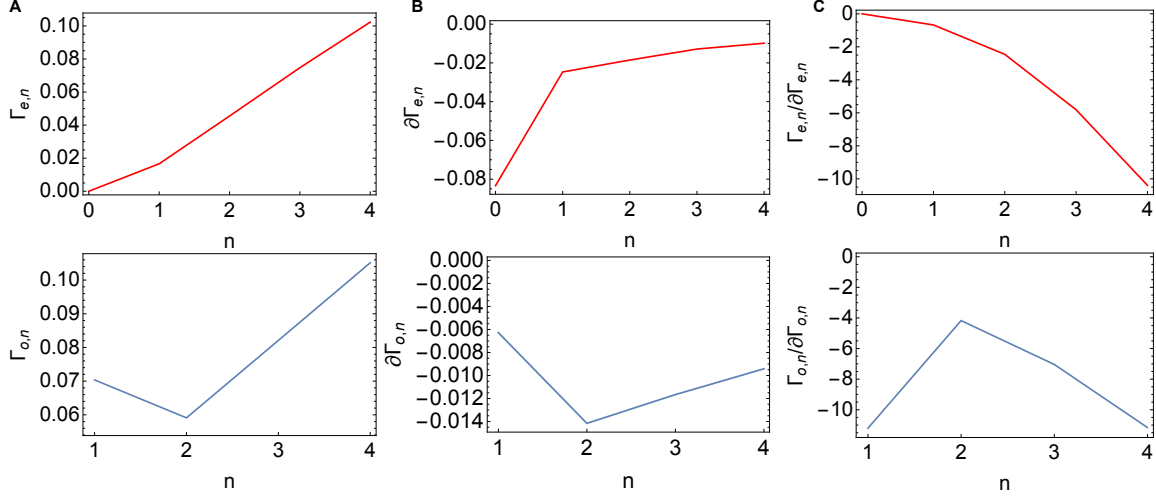


Figure 3.5 Expansion coefficients of $\Gamma_{e/o,n}(\sigma_{e/o,n} \frac{d^2}{4D_{\text{cyl}}})$ in $\sigma_{e/o,n}$ around zero.

$\Gamma_{e/o,n}$ is expanded in orders of $q_{e/o,n} = -\sigma_{e/o,n} \frac{d^2}{4D_{\text{cyl}}}$ around $\sigma_{e/o,n} = 0$. Given an elliptical geometry with semi-major axis $a = 27\mu\text{m}$ and semi-minor axis $b = 15\mu\text{m}$ the expansion coefficients of each order and mode can be calculated. The even coefficients are plotted on top and the odd ones at the bottom.

(A) The zeroth coefficient, which here is written in short $\Gamma_{e/o,n} := \Gamma_{e/o,n}|_{q=0}$, is plotted against the corresponding mode.

(B) The first coefficient, for readability $\partial\Gamma_{e/o,n} := \partial_q \Gamma_{e/o,n}|_{q=0}$, is plotted against the corresponding mode.

(C) The ratio $\Gamma_{e/o,n}/\partial\Gamma_{e/o,n} = \frac{\Gamma_{e/o,n}|_{q=0}}{\partial_q \Gamma_{e/o,n}|_{q=0}}$ is plotted. It can be used to approximate the dispersion relation. Note that it is always below zero.

Solving the determinant for $\sigma_{e/o,n}$ one finds the lengthy but analytical expression

$$\begin{aligned} \sigma_{e/o,n} = & \frac{2\partial_c f}{d \cdot \partial\Gamma_{e/o,n}} + \frac{D_c \Gamma_{e/o,n}}{\partial\Gamma_{e/o,n}} + \frac{\partial_m f}{2} + \frac{2D_m n^2 \pi^2}{L^2} \\ & \pm \sqrt{\left(\frac{2\partial_c f}{d \cdot \partial\Gamma_{e/o,n}} + \frac{D_c \Gamma_{e/o,n}}{\partial\Gamma_{e/o,n}} + \frac{\partial_m f}{2} + \frac{2D_m n^2 \pi^2}{L^2} \right)^2} \\ & - \frac{16D_m \partial_c f n^2 \pi^2}{d \cdot \partial\Gamma_{e/o,n} L^2} - \frac{4D_c \Gamma_{e/o,n} (\partial_m f L^2 + 4D_m n^2 \pi^2)}{d \cdot \partial\Gamma_{e/o,n} L^2}, \end{aligned} \quad (3.58)$$

where the subscript $q = 0$ was dropped for readability. From $f(m, c) = k^{\text{on}} c - k^{\text{off}} m + k^{\text{d}} \cdot m^2 c$ it follows:

$$\partial_c f = k^{\text{on}} + k^{\text{d}} \cdot m^2 \quad (3.59)$$

$$\partial_m f = -k^{\text{off}} + 2k^{\text{d}} \cdot m. \quad (3.60)$$

One can see that $\partial_c f$ is always positive and $\partial_m f$ is positive for sufficiently large recruitment rates and membrane fixed point concentrations. Plugging in the flux operator coefficients (see numerical values in **Fig. 3.5**) one already finds a tendency of which modes become unstable before others, when $\partial_c f$ and $\partial_m f$ are both positive. Note that $\Gamma_{e/o,n}$ is always positive while $\partial\Gamma_{e/o,n}$ is always negative. Furthermore, by looking at the numerical values one sees directly $\frac{\Gamma_{o,1}}{\partial\Gamma_{o,1}}$ and $\frac{1}{\partial\Gamma_{o,1}}$ are large negative numbers, larger than these contributions for other modes. As the inequalities hold: $\frac{\Gamma_{o,n}}{\partial\Gamma_{o,n}} < \frac{\Gamma_{e,n}}{\partial\Gamma_{e,n}}$, $\frac{1}{\partial\Gamma_{o,n}} < \frac{1}{\partial\Gamma_{e,n}}$, and $\frac{\Gamma_{o,1}}{\partial\Gamma_{o,1}} < \frac{1}{\partial\Gamma_{o,1}}$, even modes have larger growth rates. Therefore, one can already conclude that in a recruitment model with sufficiently strong recruitment the even modes become unstable before the odd modes.

This agrees with the heuristic picture presented in chapter 1. There, it was argued that in a recruitment driven model the membrane reencountering in highly curved membrane regions would establish high concentrations there. In elliptical geometry the highly curved regions are the poles of the ellipse. The zeroth to second even modes all correspond to domains of high concentrations at the cell poles (see **Fig. 3.4**) whereas odd modes have high concentration peaks in the flatter regions at midcell or diagonally.

With a rough approximation of the flux operator one can therefore already support the heuristic picture for recruitment.

3.3.5 Mutual antagonism in elliptical geometry

Consider the model first introduced by Goehring et al [31, 82], but without cortical flows and in elliptical geometry. Two species, A and P , exist in membrane-bound form, m_A and m_P , and in cytosolic form, c_A and c_P . Without a rapid-mixing assumption, which was used in [31, 82], this system is comprised of four components. The membrane reaction-diffusion equations are

$$\partial_t m_A = D_{m_A} \nabla_{\parallel}^2 m_A + f(m_A, m_P; c_A, c_P), \quad (3.61)$$

$$\partial_t m_P = D_{m_P} \nabla_{\parallel}^2 m_P + h(m_A, m_P; c_A, c_P) \quad (3.62)$$

with

$$f(m_A, m_P; c_A, c_P) = k_{\text{on},A} c_A - k_{\text{off},A} m_A - k_{Ap} m_P^\beta m_A, \quad (3.63)$$

$$h(m_A, m_P; c_A, c_P) = k_{\text{on},PCP} - k_{\text{off},P} m_P - k_{Pa} m_A^\alpha m_P. \quad (3.64)$$

In the bulk there is only diffusion:

$$\partial_t c_A = D_{c_A} \nabla^2 c_A, \quad (3.65)$$

$$\partial_t c_P = D_{c_P} \nabla^2 c_P \quad (3.66)$$

The reactive boundary condition reads

$$D_{c_A} \nabla_{\parallel} c_A \Big|_{\mu=\mu_0} = -f(m_A, m_P; c_A, c_P), \quad (3.67)$$

$$D_{c_P} \nabla_{\parallel} c_P \Big|_{\mu=\mu_0} = -h(m_A, m_P; c_A, c_P) \quad (3.68)$$

The linearised form of this system becomes

$$0 = \underbrace{\begin{pmatrix} \partial_t(\cdot) - \partial_{m_A} f - D_{m_A} \nabla_{\parallel}^2 & -\partial_{m_P} f & -\partial_{c_A} f & -\partial_{c_P} f \\ -\partial_{m_P} h & \partial_t(\cdot) - \partial_{m_P} h - D_{m_P} \nabla_{\parallel}^2 & -\partial_{c_A} h & -\partial_{c_P} h \\ \partial_{m_A} f & \partial_{m_P} f & \partial_{c_A} f & \partial_{c_P} f \\ \partial_{m_P} h & \partial_{m_P} h & \partial_{c_A} h & \partial_{c_P} h \end{pmatrix}}_{=:\hat{F}} \cdot \begin{pmatrix} \delta m \\ \delta c \end{pmatrix} \quad (3.69)$$

$$+ \underbrace{\begin{pmatrix} 0 & 0 & 0 & 0 \\ 0 & 0 & 0 & 0 \\ 0 & 0 & D_{c_A} & 0 \\ 0 & 0 & 0 & D_{c_A} \end{pmatrix}}_{=:\hat{D}} \cdot \begin{pmatrix} \delta m \\ \delta c \end{pmatrix} \quad (3.70)$$

As before, the derivatives can be evaluated with

$$\nabla_{\parallel}^2 \rightarrow -\left(\frac{2\pi n}{L}\right)^2, \quad (3.71)$$

$$\partial_t \rightarrow \sigma_{e/o,n}, \quad (3.72)$$

and

$$\nabla_N \Big|_{\mu=\mu_0} \rightarrow \Gamma_{e/o,n}(\sigma_{e/o,n} d^2 / 4D_{c_A}), \text{ or } \nabla_N \Big|_{\mu=\mu_0} \rightarrow \Gamma_{e/o,n}(\sigma_{e/o,n} d^2 / 4D_{c_P}), \quad (3.73)$$

where the last replacement depends on the species on which the flux operator acts, A or P .

The linearised system of equations is then described in matrix form with

$$0 = \det \left(\hat{F}_{e/o,n} + \hat{D}_c \cdot \hat{\Gamma}_{e/o,n} \right), \quad (3.74)$$

where the subscript $e/o, n$ denotes the dependency on $\sigma_{e/o,n}$ by replacing the derivatives above, and

$$\hat{D}_c \cdot \hat{\Gamma} = \begin{pmatrix} D_{c_A} & 0 \\ 0 & D_{c_P} \end{pmatrix} \cdot \begin{pmatrix} \Gamma_{e/o,n}(\sigma_{e/o,n} d^2 / 4D_{c_A}) & 0 \\ 0 & \Gamma_{e/o,n}(\sigma_{e/o,n} d^2 / 4D_{c_P}) \end{pmatrix}. \quad (3.75)$$

Following the idea of a former Master student in our group [41] this can be written in block matrix structure:

$$0 = \begin{pmatrix} \sigma_{e/o,n} + \left(\frac{2\pi n}{L}\right)^2 \cdot \hat{D}_m - \hat{a} & -\hat{A} \\ \hat{a} & \hat{D}_c \hat{\Gamma} + \hat{A} \end{pmatrix} \cdot \begin{pmatrix} \delta m \\ \delta c \end{pmatrix}, \quad (3.76)$$

where

$$\hat{D}_m = \begin{pmatrix} D_{m_A} & 0 \\ 0 & D_{m_P} \end{pmatrix}, \quad (3.77)$$

$$\hat{D}_c \hat{\Gamma} = \begin{pmatrix} D_{c_A} & 0 \\ 0 & D_{c_P} \end{pmatrix} \cdot \begin{pmatrix} \Gamma_{e/o,n} \left(\sigma_{e/o,n} d^2 / 4D_{c_A} \right) & 0 \\ 0 & \Gamma_{e/o,n} \left(\sigma_{e/o,n} d^2 / 4D_{c_P} \right) \end{pmatrix}, \quad (3.78)$$

$$\hat{a} := \begin{pmatrix} \partial_{m_A} f & \partial_{m_P} f \\ \partial_{m_A} h & \partial_{m_P} h \end{pmatrix}, \quad (3.79)$$

and

$$\hat{A} := \begin{pmatrix} \partial_{c_A} f & \partial_{c_P} f \\ \partial_{c_A} h & \partial_{c_P} h \end{pmatrix}. \quad (3.80)$$

For the model here, where the reaction function of one species does not depend on the cytosolic component of the other species, i.e. $\partial_{c_P} f = 0$ and $\partial_{c_A} h$, one can get rid of some terms at this point. This simplifies \hat{A} to a diagonal matrix:

$$\hat{A} := \begin{pmatrix} \partial_{c_A} f & 0 \\ 0 & \partial_{c_P} h \end{pmatrix}. \quad (3.81)$$

Writing out the determinant in block matrix structure one finds the next simplification:

$$\begin{aligned} 0 &= \det \begin{pmatrix} \sigma_{e/o,n} + \left(\frac{2\pi n}{L}\right)^2 \cdot \hat{D}_m - \hat{a} & -\hat{A} \\ \hat{a} & \hat{D}_c \hat{\Gamma} + \hat{A} \end{pmatrix} \\ &= \det \begin{pmatrix} \sigma_{e/o,n} + \left(\frac{2\pi n}{L}\right)^2 \cdot \hat{D}_m & \hat{D}_c \hat{\Gamma} \\ \hat{a} & \hat{D}_c \hat{\Gamma} + \hat{A} \end{pmatrix}, \end{aligned} \quad (3.82)$$

As before, plugging in the power series expansion

$$\Gamma_{e/o,n} := \sum_{i=0}^{\infty} \left(-\frac{d}{4D_{\text{cyt}}} \right)^i \frac{\partial_q^i \Gamma_{e/o,n} \Big|_{q=0}}{i!} \cdot \sigma_{e/o,n}^i. \quad (3.83)$$

at some cutoff for the i , altogether the dispersion relation can be calculated. However, higher order approximations of $\Gamma_{e/o,n}$ in the determinant of the four-by-four matrix leads to higher order polynomials in $\sigma_{e/o,n}$, which makes calculation by hand difficult. To obtain a very intuitive first result, one can further simplify. Very close to onset of pattern formation, where $\sigma_{e/o,n} \approx 0$ a cutoff after the zeroth order might already give a valuable approximation of the dispersion relation and is analytically feasible.

Keeping only the zeroth expansion coefficients $\Gamma_{e/o,n}|_{q=0}$ one finds an expression for the dispersion relation

$$\sigma_{e/o,n} = \frac{1}{2} \text{Tr} \Lambda_{e/o,n} \left(-1 \pm 4 \frac{\det \Lambda_{e/o,n}}{\text{Tr}^2 \Lambda_{e/o,n}} \right), \quad (3.84)$$

where

$$\Lambda_{e/o,n} = \begin{pmatrix} \left(\frac{2\pi n}{L}\right)^2 \cdot D_{m_A} - \frac{\partial_{m_A} f}{1 + \frac{\partial_{c_A} f}{\Gamma_{e/o,n}|_{q=0}^{Dc_A}}} & -\frac{\partial_{m_P} f}{1 + \frac{\partial_{c_A} f}{\Gamma_{e/o,n}|_{q=0}^{Dc_A}}} \\ -\frac{\partial_{m_A} h}{1 + \frac{\partial_{c_P} h}{\Gamma_{e/o,n}|_{q=0}^{Dc_P}}} & \left(\frac{2\pi n}{L}\right)^2 \cdot D_{m_P} - \frac{\partial_{m_P} h}{1 + \frac{\partial_{c_P} h}{\Gamma_{e/o,n}|_{q=0}^{Dc_P}}} \end{pmatrix}, \quad (3.85)$$

From this estimation for the dispersion relation it is possible to draw some conclusions for the model based on mutual antagonism.

Our former Master student, *Thomas Fehm*, could show that if $\partial_{m_A} f < 0$ and $\partial_{m_P} h < 0$, then the n^{th} odd mode must become unstable before the n^{th} even mode [41].

For this specific system, it is in general true that $\partial_{m_A} f < 0$ and $\partial_{m_P} h < 0$. Therefore, this estimate of the dispersion relation implies an onset of pattern formation with odd modes, such as short-axis polarisation.

This finding gave rise to set up a new model for the PAR system, in which even modes can grow before odd modes. The model, based on mutual antagonism, recruitment and a cytosolic inactive phase is presented in chapter 4.

3.4 Conclusion of linear stability analysis in geometry

In conclusion of the above calculations, linear stability in specific geometries has proven useful for the following

- It is analytically more feasible than dealing with the full nonlinear reaction-diffusion systems in geometry.
- Therefore, it is much more efficient for large parameter sweeps than computer simulations of the full dynamics with a Finite Element Method.
- Besides, an efficient search for regimes of pattern formation from uniform solutions provides an efficient way to find regimes of pattern formation at all!

- It also follows that heuristic intuitions can be checked at least partially with analytic calculations. This helps to understand the onset of pattern formation more intuitively.

However, as also shown in chapter 4, linear stability analysis is not an appropriate method for understanding the final pattern of a system. Furthermore, linear stability in specific geometries can not provide insight into the full, time-dependent dynamics. Results from linear stability analysis just predict the behaviour right at onset of pattern formation, i.e. in a linear regime around a uniform solution.

Chapter 4

Geometric cues stabilise long-axis polarisation by the PAR system

This chapter presents my main theoretical project on the PAR reaction-diffusion system and its capability to polarise along the long cellular axis in the *C. elegans* zygote. In this project I worked together with *Jacob Halatek*, *Laeschkir Würthner* and was supervised by *Erwin Frey*. The chapter is taken from the manuscript "Geometric cues stabilise long-axis polarisation of PAR protein patterns in *C. elegans*", which we published in Nature Communications [32].

4.1 Abstract

In the *Caenorhabditis elegans* zygote, PAR protein patterns, driven by mutual antagonism, determine the anterior-posterior axis and facilitate the redistribution of proteins for the first cell division. Yet, the factors that determine the selection of the polarity axis remain unclear. We present a reaction-diffusion model in realistic cell geometry, based on biomolecular reactions and accounting for the coupling between membrane and cytosolic dynamics. We find that the kinetics of the phosphorylation-dephosphorylation cycle of PARs and the diffusive protein fluxes from the cytosol towards the membrane are crucial for the robust selection of the anterior-posterior axis for polarisation. The local ratio of membrane surface to cytosolic volume is the main geometric cue that initiates pattern formation, while the choice of the long-axis for polarisation is largely determined by the length of the aPAR-pPAR interface, and mediated by processes that minimise the diffusive fluxes of PAR proteins between cytosol and membrane.

4.2 Introduction

Cell polarisation is a crucial process in development [90]. Well studied examples include localisation of bud sites in *Saccharomyces cerevisiae* [91], apico-basal asymmetry in mammalian epithelial cells [92], and the asymmetric placement of the first cell division in the *Caenorhabditis elegans* zygote [93]. A key question in such systems is how the correct polarity axis is established and robustly maintained.

In *C. elegans*, the anterior-posterior axis of the embryo is determined in the fertilised egg by a polarised distribution of PAR (partitioning defective) proteins [46, 48, 93]. Immediately before the establishment of polarisation begins, the future anterior PARs (aPARs) cover the cell cortex uniformly, while posterior PARs (pPARs) are cytoplasmic [67]. After fertilisation, the sperm-donated centrosome induces contraction of the actomyosin network, which leads to cortical flows that displace cortical aPARs anteriorly, allowing cytoplasmic pPARs to bind in the posterior zone [31, 54, 57, 94]; see **Fig. 4.1(A)**. Once these two PAR domains have formed (during the ‘establishment phase’) and have thereby established the anterior-posterior axis, they persist for several minutes through the ‘maintenance’ phase until cell division [46, 67].

Several independent in vivo experiments on *C. elegans* have demonstrated that maintenance of PAR protein polarity is independent of an intact actomyosin network [67, 83, 94–97]. Rather, it appears that the entry of the sperm and the following contractions of the cortical actomyosin serve as a temporal trigger for the rapid establishment of the PAR protein pattern [26, 31, 96]. However, experimental observations also suggest that while the rapid establishment and perfect position of anterior-posterior PAR domains are the result of an interplay between mechanical, hydrodynamical and biochemical mechanisms, polarisation is nevertheless robustly established (albeit with some delay) when various mechanical and hydrodynamical mechanisms are eliminated. [53, 57, 94, 98, 99]. To disentangle and understand these distinct mechanisms one needs to investigate the mechanism of self-organised polarisation by the biochemical PAR protein network. Based on the fact that aPAR and pPAR proteins mutually drive each other off the membrane by phosphorylation [58], and that this antagonism promotes formation of distinct domains on the membrane [5, 57, 62], previous studies have outlined how self-organisation of PAR proteins maintain polarisation until cell division [26, 83, 100]. These studies showed that basic features of PAR protein polarisation can be explained by minimal reaction-diffusion models. However, as these models used a simplified one-dimensional geometry and assumed that cytosolic proteins are homogeneously distributed, the effect of cell geometry was disregarded and the distinction between long and short axis was lost. Thus, how the long axis is selected for polarisation and subsequently maintained, and in a broader context, which features of a reaction-diffusion system are responsible for axis selection remain open questions.

To answer these questions we draw on previous studies of other intracellular pattern-forming protein systems which revealed that even the typically rather fast cytosolic diffusion does not eliminate protein gradients in the cytosol [13, 27, 35, 36]. As a consequence, protein patterns are generically sensitive to cell geometry through coupling between processes in the cytosol and on the membrane. In particular, it

was predicted [35, 36] that delayed reattachment to the cell membrane (e.g., due to cytosolic nucleotide exchange) is key to geometry sensing. Indeed, recent experimental studies support the idea that axis selection depends on the interplay between reaction kinetics and cellular geometry [27].

These results suggest that the protein dynamics in the cytoplasm of the *C. elegans* embryo may also influence the selection of the long over the short axis during polarity maintenance. In order to investigate axis alignment, we developed a reaction-diffusion model of the PAR protein dynamics. As in previous studies [31, 42, 83], a central element in our model is mutual displacement of membrane-bound aPARs and pPARs by phosphorylation. However, in contrast to earlier models [31, 82], we do not use effective nonlinearities but strictly biomolecular reactions based on mass-action law kinetics, e.g. by explicitly modelling the formation of PAR protein complexes. Importantly, we also account for the delay caused by the need for reactivation of detached PAR proteins by cytosolic dephosphorylation, thus introducing the generic feature of a biochemical activation-deactivation cycle.

Our extended reaction-diffusion model in realistic cell geometry reveals that the dynamics of the phosphorylation-dephosphorylation cycle of PAR proteins is crucial for long-axis polarisation. Without this additional feature, the biochemical network of PAR proteins would not lead to robust polarisation along the long axis but instead exhibit a strong tendency to first polarise along the short axis, and polarisation would not re-align within a time that corresponds to a typical time before cell division. Furthermore, the extended model enables us to characterise the roles of mutual antagonism (phosphorylation) and overall protein numbers in robust long-axis polarisation: while the phosphorylation rates determine how distinctively one polarisation axis is selected over the other, relative protein numbers primarily affect the robustness of pattern formation as a whole.

Most importantly, our analysis indicates that these findings can be generalised beyond the specific model for the PAR system: axis selection is based on the generic dependence of intracellular pattern-forming processes on the local ratio of membrane surface to cytosolic volume and on the cell geometry via the length of the interface between the two different protein domains. Broadly speaking, the membrane-to-bulk ratio determines the likelihood that a given protein will reattach to the membrane quickly after detachment into the cytosol and the interface length affects both the establishment and maintenance of long-axis polarisation.

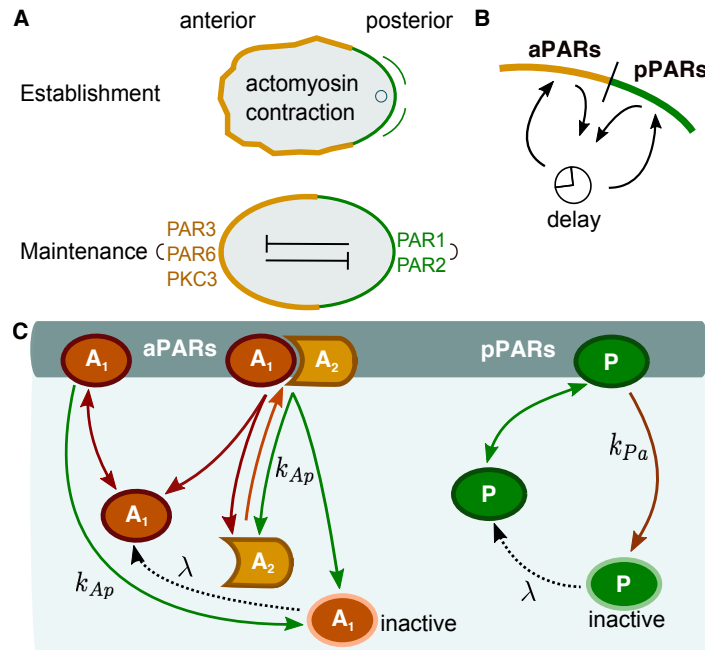


Figure 4.1 Biological background and model network (A) Cell polarisation in the *C. elegans* embryo during the establishment (top) and maintenance (bottom) phases; sketch adapted from Ref. [46]. **(B)** Illustration of protein flux between cytosol and membrane. As proteins detach from the membrane when phosphorylated, they cannot immediately rebind to the membrane. There is therefore an intrinsic delay before dephosphorylation permits rebinding. **(C)** The biochemical reaction network is comprised of two mutually antagonistic sets of proteins, aPARs and pPARs. Dephosphorylated (active) A_1 and P attach to the membrane with rates k_a^{on} and k_p^{on} , respectively. Both active proteins may also detach spontaneously from the membrane with rates k_a^{off} and k_p^{off} , respectively. A_1 acts as a scaffold protein: Once bound to the membrane it recruits A_2 with rate k_d and forms a membrane-bound hetero-dimeric aPAR complex A_{12} . The hetero-dimer A_{12} may itself spontaneously detach from the membrane with rate k_a^{off} and dissociate into A_2 and active A_1 . Membrane-bound A_1 and A_{12} can also be phosphorylated by P with rate $k_{Ap}[P]$, thereby initiating dissociation of the aPAR complex and release of aPAR proteins into the cytosol. While reattachment of the scaffold protein A_1 is delayed by the requirement for dephosphorylation (reactivation), detached A_2 can be recruited to the membrane by membrane-bound A_1 immediately. Similarly, P is phosphorylated by the hetero-dimer A_{12} at rate $k_{Pa}[A_{12}]$, and is consequently released as inactive P into the cytosol. In the same way as A_1 , also P must be dephosphorylated before it can bind again to the membrane. For simplicity, we take identical dephosphorylation (reactivation) rates λ for inactive A_1 and P . The ensuing reaction-diffusion equations are provided in the Method section 4.5.1 and a table listing the values of the rate constants can be found in 4.1. **(D)** Sketch of the cell's geometry: Prolate spheroid with long axis a and short axis b , and with short- (left) and long-axis (right) polarisation.

4.3 Results

4.3.1 Model

The aPAR set of proteins comprises PAR-3, PAR-6, and the atypical protein kinase PKC-3. Only complexes containing PKC-3 can phosphorylate pPARs, thereby disabling their membrane-binding capacity [61, 62]. How trimeric complexes consisting of PAR-3, PAR-6 and PKC-3 actually form is not fully understood. The evidence so far suggests that PAR-6 acts as a linker between PKC-3 and PAR-3, which can itself bind directly to the membrane [55, 63–65]. In the absence of PAR-6, PKC-3 freely diffuses in the cytosol [59, 60]. In the reaction network upon which our mathematical model is based, we simplify the formation of trimeric complexes to the formation of a complex consisting of two effective species of aPARs: A_1 and A_2 (**Fig. 4.1 (C)**). The first species, A_1 , models the membrane binding function of PAR-3, thus we also refer to it as a scaffold protein. The second species, A_2 , corresponds to a complex of PAR-6 and PKC-3. It is assumed to be recruited by scaffold proteins A_1 that are already bound to the membrane, thereby forming hetero-dimers A_{12} on the membrane. These complexes can then phosphorylate membrane-bound pPARs, which initiates their release into the cytosol in a phosphorylated (inactive) state.

As with aPARs, there are different pPAR species, PAR-1 and PAR-2. While it is known that PAR-2 binds directly to the membrane, and PAR-1 phosphorylates PAR-3, it remains unclear whether PAR-2 also helps to maintain anterior-posterior polarity by excluding aPAR complexes from the membrane [58, 67]. However, PAR-2 is required for posterior binding of PAR-1 [66] and PAR-2 exclusion from the membrane by PKC-3 is essential for proper restriction of pPARs to the posterior [62]. In view of the remaining uncertainties we refrain from distinguishing between different species and effectively treat the pPARs as a single species P (**Fig. 4.1 (C)**). P phosphorylates membrane-bound A_1 and A_{12} , which triggers their subsequent detachment as a phosphorylated (inactive) species into the cytosol.

Our model also accounts for protein dephosphorylation reactions in the cytosol. This creates deactivation-reactivation cycles, as proteins that were phosphorylated (deactivated) on the membrane are thereby reactivated for membrane binding (**Fig. 4.1 (B), (C)**). For simplicity, the reactivation (dephosphorylation) rate λ is assumed to be identical for cytosolic pPARs (P) and aPARs (only A_1). The ensuing reaction-diffusion equations are given in the Method section Equations (4.7-4.18).

We approximate the natural shape of a *C. elegans* embryo by a prolate spheroid with semi-axis lengths $a = 27\mu\text{m}$ and $b = 15\mu\text{m}$ (see **Fig. 4.1 (D)**) [31]. Here, a is the distance from centre to pole through a focus along the symmetry axis, also called the semi-major axis, while b is the equatorial radius of the spheroid, which is called the semi-minor axis. The boundary and interior of the ellipse represent the cell membrane and cytosolic volume, respectively.

4.3.2 Dephosphorylation plays a key role for axis determination

For mutually antagonistic protein interactions, protein domains are separated by an interface at which mutually induced membrane detachment dominates [26, 31, 83]. For its maintenance proteins that have detached from the membrane must be replaced, otherwise the antagonistic interaction between the proteins would deplete either aPARs or pPARs from the membrane. As the protein interactions are mass-conserving, maintenance requires that detached proteins quickly rebind, unless the cytosolic reservoir of proteins is large enough for them to be replenished directly. This suggests that an interface can best be maintained locally in those membrane regions where rebinding to the membrane after detachment is most likely.

The likelihood of rebinding depends on the availability of cytosolic proteins for binding, which depends on the interplay between the local cell geometry and the time required for reactivation of detached proteins by dephosphorylation (**Fig. 4.2**). The ratio of available membrane surface to cytosolic volume is highest at cell poles and lowest at mid-cell. How this local cell geometry affects protein rebinding depends on the dephosphorylation time: a longer reactivation time implies that a protein that detached in a phosphorylated state from the membrane will on average diffuse farther away from the membrane before it can be reactivated and reattaches. The corresponding reactivation length is estimated as

$$\ell := \sqrt{D_{\text{cyt}}/\lambda}. \quad (4.1)$$

To see how this diffusion length affects protein dynamics, consider a protein with a short inactive (phosphorylated) phase, such that ℓ is significantly smaller than the cell length $L = 2a$ (**Fig. 4.2 (A)**). Then, proteins are likely to be dephosphorylated fast and can therefore rebind very soon after phosphorylation-induced detachment. Since the local ratio of membrane surface to cytosolic volume at the cell poles is larger than at mid-cell, these proteins are more likely to reencounter the membrane in the polar zone which translates into higher polar reattachment (after reactivation), i.e. proteins remain caged at the cell poles (**Fig. 4.2 (A)**). Conversely, proteins that detached from the membrane at mid-cell have more cytosolic volume available than those that detached at the poles and, thus, are less likely to re-encounter the membrane and rebind there (**Fig. 4.2 (A)**). This heuristic picture suggests that for $\ell \ll L$ domain interfaces preferentially form at the cell poles and hence cell polarity will be established along the short-axis. If dephosphorylation requires more time, ℓ increases and the effect of local membrane curvature is attenuated (**Fig. 4.2 (B)**). Ultimately, when $\ell > L$, proteins can be considered as uniformly distributed throughout the cytosol for the next attachment event (**Fig. 4.2 (D)**). Therefore, reactivated proteins are more likely to attach at mid-cell, where the accumulated density along the long-axis (or, equivalently, the ratio of cytosolic volume to membrane area) is highest (**Fig. 4.2 (C)**). This implies that an interface between different protein domains will establish itself at mid-cell and cells will become polarised along the long-axis for large enough reactivation length ℓ .

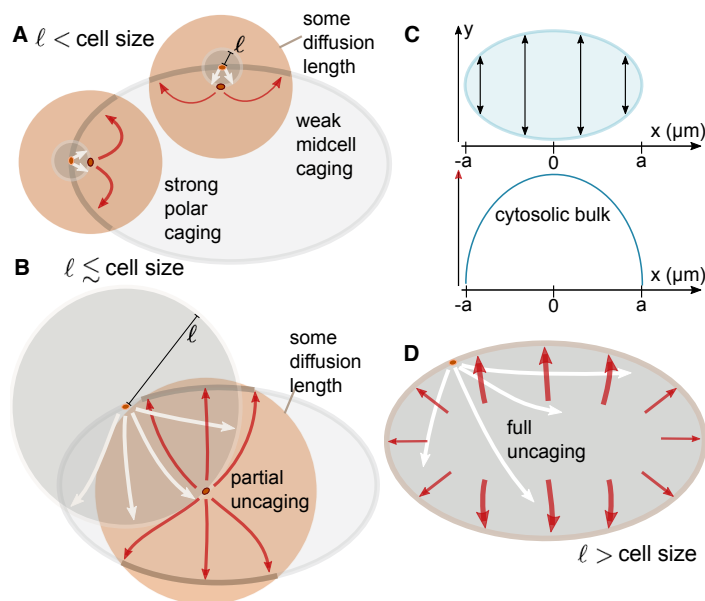


Figure 4.2 Role of dephosphorylation in axis determination. (A, B, and D): A protein is shown in the elliptical cell firstly at its phosphorylation and detachment site on the membrane and then at the point of its reactivation. The reactivation length gives an average radius (gray circles) how far from the detachment point a protein travels before reactivation. The orange circles around the reactivated protein and the associated arrows sketch some diffusion distance corresponding to a time interval Δt following reactivation, i.e. during this time interval the protein can reattach to the membrane. (A) If the reactivation length ℓ (radius of gray circle) is small compared to the cell size, the local membrane surface to cytosolic volume ratio strongly affects the position at which detached proteins reattach. Due to the reactivation occurring close to the membrane, within some time interval Δt following reactivation a protein that detaches from a cell pole is more likely to reattach near that same cell pole than a protein detaching from mid-cell is to reattach at mid-cell. Hence, dynamics that are based on membrane-cytosol cycling (such as antagonistic reactions that maintain an interface) are enhanced at the cell poles. (B) As the reactivation length ℓ approaches the length of the cell, this effect of geometry becomes weaker, and detaching proteins become increasingly unconstrained by the position of detachment (uncaged). (C) Illustration of the distribution of cytosolic bulk proteins along the long-axis. The elliptical cell and the cytosol height is depicted as a function of x , where the x -axis aligns with the long axis (top). The amount of cytosolic bulk proteins for each x varies from the poles to mid-cell as illustrated (bottom). (D) This effect of cell geometry is completely lost if the reactivation length ℓ exceeds the length of the cell. Hence, detached proteins become uniformly distributed throughout the cell before reactivation occurs. In that case, most will re-encounter the membrane near mid-cell after reactivation, since a delocalised protein will most likely be found in the mid-cell area.

In summary, if cell polarisation is induced by antagonistic protein interaction, we expect long-axis polarisation to be favoured only if the delay resulting from the inactive phase is sufficiently long. Moreover, our analysis suggests that relative protein numbers

affect axis selection, as the global availability of an abundant protein species attenuates the effect of cell geometry associated with the activation-deactivation cycle.

In the heuristic arguments outlined above, we tacitly considered a single position along the interface between the PAR domains. In general, however, the length of the interface may also play an important role in determining the orientation of the axis ultimately selected, as one expects energetic costs for interface establishment and maintenance to scale with its length. In the following we will analyse the system's dynamics in a two-dimensional as well as in a three-dimensional cell geometry; an analysis of a simplified rectangular geometry would actually be misleading (see also Supplementary Section 4.7.3). Furthermore, the analysis in two and three dimensions enables us to disentangle the effects due to the membrane-to-bulk ratio and interface length in polarisation establishment and maintenance. Note that in a two-dimensional ellipse the interface between the domains reduces to a point, such that all geometric effects can be solely attributed to the membrane-to-bulk ratio.

4.3.3 Growth rates of long versus short-axis polarisation

To put the above heuristic reasoning concerning the role of membrane-to-bulk ratio on a firm basis, we first performed a mathematical analysis in two-dimensional elliptical geometry, building on previous investigations of intracellular pattern formation [35, 36].

Importantly, in the bounded geometry of a cell, broken detailed balance due to the dephosphorylation-phosphorylation cycle implies that a uniform well-mixed state can no longer be a steady state of the system [36]. Instead, all steady states show cytosolic gradients with a density profile that is spatially non-uniform but unpolarised [36]. As the reactive dynamics in the PAR system is bistable, there are two such unpolarised states, one with aPAR and the other with pPAR being the more abundant membrane species. In the zygote, aPARs predominate on the membrane, and we refer to this aPAR-dominant state as the unpolarised state.

To perform a linear stability analysis with respect to this unpolarised state, we use Fourier modes specific for elliptical geometry [35]. These modes are classified as even and odd by their symmetry with respect to reflections through a plane along the long axis, and correspond to patterns aligned along the long and short axes, respectively (**Fig. 4.3 (A)**). If the real parts of the growth rates σ of all modes are negative, small spatial perturbations of the unpolarised state will decay and it will remain stable. In contrast, a positive real part of any growth rate ($\sigma > 0$) indicates that the unpolarised state is unstable, and initially a pattern will emerge corresponding to the mode with the highest growth rate (**Fig. 4.3 (B)**). Hence, linear stability analysis can identify the parameter regime where patterns of a certain symmetry (short- vs. long-axis) form spontaneously. On very general grounds [13, 33], we expect that bifurcations in mass-conserving reaction-diffusion systems are subcritical and hence these pattern attractors persist over some range outside the linear unstable parameter regime (see also details on FEM simulations in the Method section), where patterns do not form

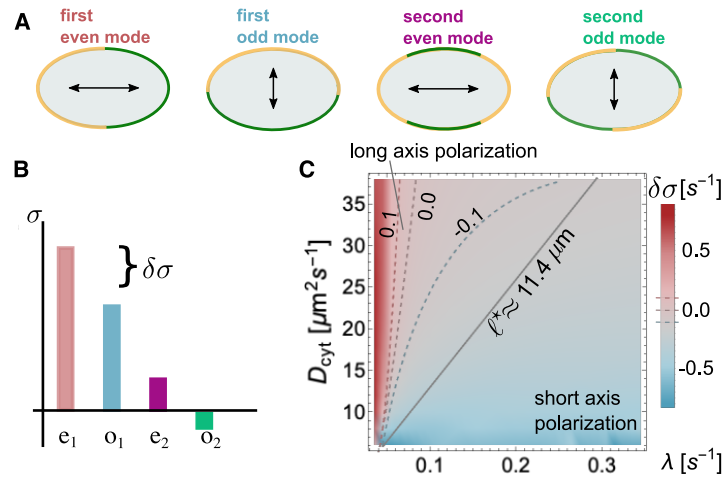


Figure 4.3 Mode selection and polarity. (A) Illustration of the protein distribution on the membrane and the ensuing polarity axis for the lowest-order even and odd modes. (B) Illustration of the mode spectrum for these lowest-order modes and the gap $\delta\sigma$ in the growth rates between the first even and odd modes. (C) Relative difference in the growth rates of the first even and odd modes (linear stability analysis in colour code with dashed threshold lines $\delta\sigma = 0\text{ s}^{-1}$, $\delta\sigma = \pm 0.1\text{ s}^{-1}$), $\delta\sigma$, as a function of D_{cyt} and λ . For small λ and large D_{cyt} , $\delta\sigma$ is clearly greater than zero (red, long-axis polarisation), whereas for large λ and small D_{cyt} , $\delta\sigma$ lies below zero (blue, short-axis polarisation). These findings are validated using FEM simulations. FEM sweeps in D_{cyt} and λ were run until the steady state was reached. These simulations yielded a straight-line interface (black-solid line in (C)) in the λ - D_{cyt} parameter space which divides long- (above) from short-axis (below) polarisation in steady state. The line corresponds to a constant threshold reactivation length ℓ^* . All other parameters can be found in Table 4.1.

spontaneously but can be triggered by a finite perturbation – such as the fertilisation event.

For a typical cell size and cytosolic diffusion constants in the range of $D_{\text{cyt}} = 5 - 50 \mu\text{m}^2\text{s}^{-1}$, linear stability analysis shows that second- and higher-order modes are negligible compared to the first even and odd modes, σ_e and σ_o . In the parameter regime under consideration, those two growth rates exhibit similar magnitude and at least one of them is positive. To quantify the competition between the first even and odd modes (long- vs. short-axis), we define the relative difference in their growth rates,

$$\delta\sigma := (\sigma_e - \sigma_o) / \sqrt{\sigma_e^2 + \sigma_o^2}; \quad (4.2)$$

for an illustration see **Fig. 4.3 (B)**.

4.3.4 Cytosolic reactivation length is crucial for axis selection

We computed $\delta\sigma$ as a function of λ and D_{cyt} . As shown in **Fig. 4.3 (C)**, the even mode dominates ($\delta\sigma > 0$) for large cytosolic diffusion constant and low reactivation rates (favouring long-axis polarisation), otherwise the odd mode dominates. This is

consistent with the above heuristic reasoning suggesting that reactivation must be slow or cytosolic diffusion must be fast for the establishment of long-axis polarity. While linear stability analysis can elucidate the selection of the polarisation axis during the onset of pattern formation, it can not predict the final pattern as it neglects nonlinear effects in the diffusion-reaction equation. To determine the final stable polarisation axis we performed finite-element (FEM) simulations; see also details on FEM simulations in the Method Section. These simulations show that there is a threshold value for the reactivation length $\ell^* = 11.4 \mu m$ above/below which cells stably polarise along the long/short-axis (**Fig. 4.3 (C)**). We conclude that in a two-dimensional cell geometry the reactivation length ℓ , which determines the spatial distribution of active proteins, is the decisive parameter that determines both initial axis selection and its long-term maintenance. How in full three-dimensional cell geometry this effect of the membrane-to-bulk ratio interacts with the role of the interface length will be discussed below.

4.3.5 Role of phosphorylation rates

Whether there is a spatial separation between aPAR and pPAR domains, is known to depend on the relative magnitude of the phosphorylation rates k_{Ap} and k_{Pa} [26, 31]: an interface between different domains exists and can be maintained only if these antagonistic phosphorylation processes are balanced. To determine the necessary conditions for this balance, we analysed the stability of the unpolarised state using linear stability analysis varying both phosphorylation rates over one order of magnitude. We fixed $D_{\text{cyt}} = 30 \mu m^2 s^{-1}$ and chose two representative reactivation rates, $\lambda = 0.3 s^{-1}$ and $\lambda = 0.05 s^{-1}$, corresponding to reactivation lengths, $\ell = 10 \mu m$ and $\ell = 24.5 \mu m$, respectively.

Our analysis in elliptical cell geometry shows that spontaneous polarisation starting from the unpolarised state arises only within a limited range of k_{Pa}/k_{Ap} values (cones in **Fig. 4.4**), in accordance with previous studies using a one-dimensional model [31, 82]. Strikingly, however, we find that the selection of the polarisation axis does not depend on the mutual antagonism but primarily on the activation-deactivation cycle. The ratio of the phosphorylation rates mainly determines the initial preference for a polarisation axis starting from an unpolarised state (**Fig. 4.4 (A) and (B)**). Specifically, we find that for $\lambda = 0.3 s^{-1}$, the first even mode grows more slowly than the first odd mode ($\delta\sigma < 0$), favouring short-axis polarisation. In contrast, for slower reactivation $\lambda = 0.05 s^{-1}$, the first even mode grows faster than the first odd mode ($\delta\sigma > 0$). These respective preferences are most pronounced for large k_{Pa}/k_{Ap} . For the mid to low range of k_{Pa}/k_{Ap} , one finds $\delta\sigma \approx 0$, i.e. linear stability analysis does not predict a clear preference for either long- or short-axis polarisation. FEM simulations (for details on the FEM simulations see Method Section) show, however, that – irrespective of the ratio k_{Pa}/k_{Ap} – long- and short-axis polarisation in the final steady state is obtained for $\ell = 10 \mu m$ and $\ell = 24.5 \mu m$, respectively; see the Supplementary Movies **M2d_1** – **M2d_3**, which are available on the Nature Communications website as Supplementary Information of our publication [32], and see the Tables 4.2, 4.3. The there shown and

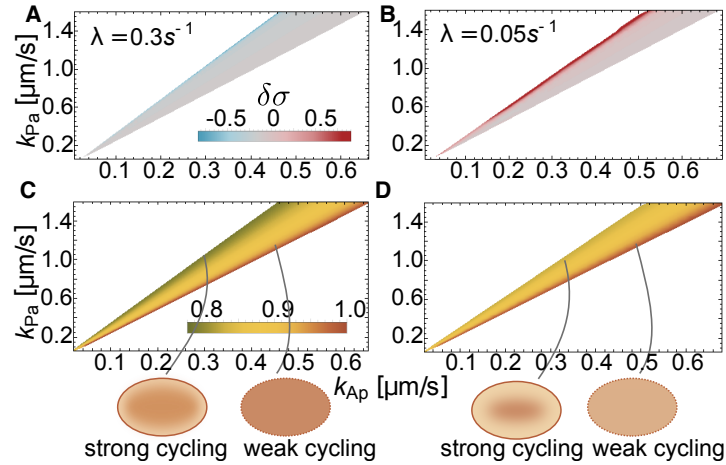


Figure 4.4 Role of phosphorylation rates in polarisation and axis selection. Linear stability analysis shows that spontaneous polarisation is possible only within a range of ratios of the phosphorylation rates, k_{Pa}/k_{Ap} (cone-shaped regions): The relative difference in the growth rates of even and odd modes ($\delta\sigma$) is shown in (A) for $\lambda=0.3\text{ s}^{-1}$, and (B) for $\lambda=0.05\text{ s}^{-1}$ in colour code (indicated in the graph). Panels (C) and (D) show the corresponding cytosolic concentration of A_1 in the aPAR dominant unpolarised state (A_2 has a quantitatively similar concentration gradient to A_1 within the cone, not shown), normalised with respect to the maximal concentration of A_1 obtained within the respective cone. Cartoons at the bottom of the figure schematically depict the cytosolic distribution of aPARs throughout the cell.

documentated simulations confirm that the reactivation length ℓ is the deciding factor for axis selection in elliptical geometry.

The FEM simulations further show that outside of the parameter regime of linear instability there exist stable polarised states, showing that the system is excitable, i.e. that patterns can be triggered by a large enough finite perturbation ; see Supplementary Section 4.7.1. This parameter regime is actually quite broad (see also **Fig. 4.7**). As a generic example for an external stimulus, we have investigated how the PAR system reacts to initial concentration gradients on the membrane that were aligned along the final stable polarisation axes. We find that large enough gradients can indeed stimulate the formation of cell polarisation. It would be interesting to specify external cues more in detail experimentally and study how they affect pattern formation. In another work we recently showed that Turing instabilities and excitability (i.e. the ability to establish a pattern by applying a larger perturbation to the stable uniform steady state) are mechanistically linked in mass-conserving systems such as the PAR system [33]. Hence, even in systems where polarity is established by an external cue, identifying a Turing instability also locates regions where external stimulation leads to stable pattern formation.

The dependence of initial growth rates on the ratio of phosphorylation rates can be attributed to the fact that, in the unpolarised (aPAR-dominant state), the cytosolic concentration of aPARs increases with the rate at which aPARs are phosphorylated by

pPARs, i.e. with a reduction in k_{Pa}/k_{Ap} (**Fig. 4.4 (C), (D)**). If a protein species is abundant in the cytosol, recycling of recently detached proteins can be compensated for by a protein of the same type in the cytosolic reservoir attaching to the membrane. Hence, effects due to different membrane-to-bulk ratios in the initial polarisation phase are dominant if the cytosolic pool of proteins undergoing an activation-deactivation cycle is low, explaining why $\delta\sigma$ depends on geometry for large values of k_{Pa}/k_{Ap} (**Fig. 4.4 (C), (D)**).

4.3.6 Axis selection depends on relative protein densities

After learning that the abundance of cytosolic proteins determines initial axis selection, we asked how changing the relative total protein densities affects cell polarisation. For all investigations up to this point the average densities were fixed to the order of magnitude determined experimentally by Gross et al. [100] (see Table 4.1 and see Supplementary Section 4.7.2). A linear stability analysis revealed that density variations alter several features: the range of ratios k_{Pa}/k_{Ap} for which an interface between different PAR domains can be stably maintained, and the threshold value of reactivation length ℓ^* that distinguishes between short- and long-axis polarisation. The effects were most prominent when the ratio of pPAR and aPAR proteins that phosphorylate each other ($[P]/[A_2]$), and the ratio of aPAR proteins ($[A_1]/[A_2]$) was varied.

As shown in **Fig. 4.5**, increasing the ratio of the antagonistic proteins ($[P]/[A_2]$) mainly shifts the regime of spontaneous cell polarisation up on the k_{Pa}/k_{Ap} axis. This upward shift is easily explained, as the effective mutual phosphorylation rates are given by $k_{Ap}[P]$ and $k_{Pa}[A_{12}]$, respectively – where $[A_{12}]$ is mainly limited by the availability of $[A_2]$. Therefore, when the concentration of pPAR proteins ($[P]$) is increased relative to $[A_2]$, the per capita rate k_{Pa} has to be increased relative to k_{Ap} as well, in order to retain the balance between the mutual phosphorylation processes.

Changing the ratio between the different types of aPAR proteins has two effects. First, spontaneous polarisation is possible for a broader range of k_{Pa}/k_{Ap} . Increasing the concentration of the scaffold protein $[A_1]$ relative to $[A_2]$, which phosphorylates pPARs, decreases the lower bound of k_{Pa}/k_{Ap} that allows for polarisation. This is a consequence of the increased reservoir size of A_1 which implies a higher rate of attachment of cytosolic A_1 to the membrane and hence a fast local redimerisation of A_2 (which lacks an inactive phase) right after the detachment of a hetero-dimer A_{12} . This newly formed hetero-dimer A_{12} is then competent to phosphorylate pPARs. Thus it is plausible that even for low k_{Pa}/k_{Ap} one can achieve a balance of mutual antagonism, extending the lower bound of the polarisation regime. Second, changing the ratio $[A_1]/[A_2]$ also has a major effect on the threshold value of the reactivation length ℓ^* . We find that ℓ^* increases with increasing concentration of the scaffold protein $[A_1]$ (**Fig. 4.5**). Again, this can be understood as a reservoir effect: globally abundant A_1 promotes immediate re-dimerisation of A_2 with any available A_1 . Axis selection is then affected by the polar recycling of A_2 .

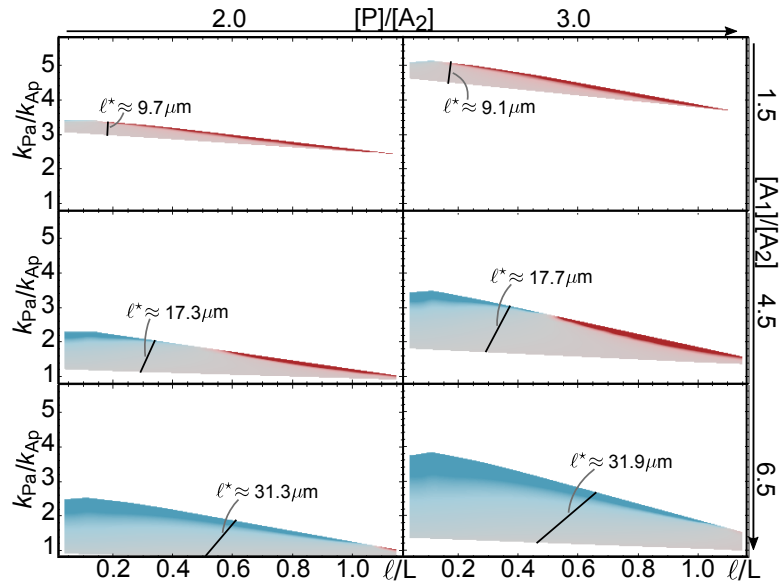


Figure 4.5 Relative protein numbers determine robustness of cell polarity. Linear stability analysis for a range of density ratios $[P]/[A_2]$ and $[A_1]/[A_2]$; $[A_2]$ was kept constant. Each graph shows the range of phosphorylation ratios (k_{Pa}/k_{Ap}) and relative reactivation lengths (ℓ/L) where the base state is linearly unstable, with $\delta\sigma$ given by the same colour code as in **Fig. 4.4 (A)**; fixed parameters are $k_{Ap} = 0.4 \mu\text{m s}^{-1}$ and $D_{\text{cyt}} = 30 \mu\text{m}^2 \text{s}^{-1}$, and further parameters not varied can be found in Table 4.1. FEM parameter sweeps of k_{Pa} and λ , with fixed parameters $k_{Ap} = 0.4 \mu\text{m s}^{-1}$ and $D_{\text{cyt}} = 30 \mu\text{m}^2 \text{s}^{-1}$, for each density set show that the steady state polarisation axis also depends strongly on the ratio $[A_1]/[A_2]$. The steady state switches from short- to long-axis polarisation at the black line in each graph, indicating ℓ^* .

Taken together, both of these findings emphasise the importance of the activation-deactivation cycle. A cell polarises more robustly when amounts of scaffold proteins are higher. However, at the same time, the cytosolic reactivation length has to increase significantly in order to also robustly maintain long-axis polarisation.

4.3.7 Role of interface length in three-dimensional cell geometry

With the previous analysis in two-dimensional cell geometry we have built up a basic understanding of the role of the membrane-to-bulk ratio for the selection of the polarisation axis. In a nutshell, we concluded that sufficiently fast diffusion and a sufficiently long inactive phase of the antagonistic proteins ensure that long-axis polarisation is established in a self-organised manner from homogeneous initial membrane concentrations. As the main parameter serving as a proxy for this effect we identified the reactivation length ℓ . Is this result directly transferable to a full three-dimensional cell geometry?

Since sensing of the local membrane-to-bulk ratio does not depend significantly on spatial dimension (see also Supplementary Section 4.7.4), one would at first sight expect

the same conclusions to hold. However, there is a fundamental difference between a three- and a two-dimensional cell geometry. While for an ellipse the interface is always point-like, for a prolate spheroid the interface is longer for short-axis polarisation than for long-axis polarisation; in our case, we have $135\ \mu\text{m}$ and $94\ \mu\text{m}$, respectively (**Fig. 4.1 (D)**). This inherent difference between a two- and a three-dimensional cell geometry could significantly affect the protein dynamics on the membrane and in the cytosol. In the absence of an interface the only geometric effect is the membrane-to-bulk ratio. Therefore, as in the two-dimensional case, we expect this ratio to be the main factor that determines the initial formation of the protein domains and the interface between them. However, as soon as an interface has formed, its length is likely to affect the stability of the polarisation axis. The maintenance of the interface between protein domains is presumably energetically costly (protein fluxes sustaining antagonistic reactions, reactivation and rebinding have to be maintained). Therefore, since the interface is longer for short-axis than for long-axis polarisation, it is possible that even an initially favoured alignment of polarisation with the short-axis can become unstable.

To assess the protein dynamics of the system in full cell geometry we performed extensive FEM simulations, restricting ourselves to parameter regimes that we identified as most relevant from the two-dimensional geometry (see Table 4.4 and compare with Table 4.1). Starting from a weakly perturbed unpolarised state we observe the following time evolution (**Fig. 4.6 (A,B)**); see the Method section on FEM simulations for 3d system and see our Supplementary Movies 4 and 5 (**M3d_1.mp4** and **M3d_2.mp4**), which are available on the website of Nature Communications as Supplementary Information of our publication [32]. During an initial time period T_{initial} a protein pattern forms that is either aligned along the short or long cell axis or somewhere in between. While long-axis polarisation is stable, any other polarisation is only metastable and after some persistence time T_{pers} transitions into stable long-axis polarisation during T_{trans} ; as discussed in Supplementary Section 4.7.5 and Supplementary Figures 4.10-4.11, there are (unphysiological) cell geometries where short-axis polarisation is stable.

We observe that, as for the two-dimensional case, initial long-axis polarisation is favoured for large cytosolic diffusion constants D_{cyt} and low reactivation rates λ , while initial short-axis polarisation is favoured for the diametrically opposed case; compare **Fig. 4.6 (D)** with **Fig. 4.3 (D)**. This shows that the local membrane-to-bulk ratio is indeed the main factor that determines initial axis selection. Moreover, the persistence time T_{pers} (**Fig. 4.6 (C)**) and the transition time T_{trans} (**Fig. 4.6 (C,D)**) both depend strongly on D_{cyt} but only weakly on λ . In the regime with a clear preference for short-axis polarisation (below the dashed line in **Fig. 4.6 (D)**), T_{trans} becomes as large as several hours; for reference see **Fig. 4.6 (D)** with $\ell^* \approx 7\ \mu\text{m}$; for further discussion and results on time scales see also Supplementary Section 4.7.8 and Supplementary **Fig. 4.14**.

Finally, we wanted to investigate the main factors that determine the stability of long- versus short-axis polarisation. As the essential novel feature of a three-dimensional cell geometry is the length of the interface between the PAR domains, we speculated

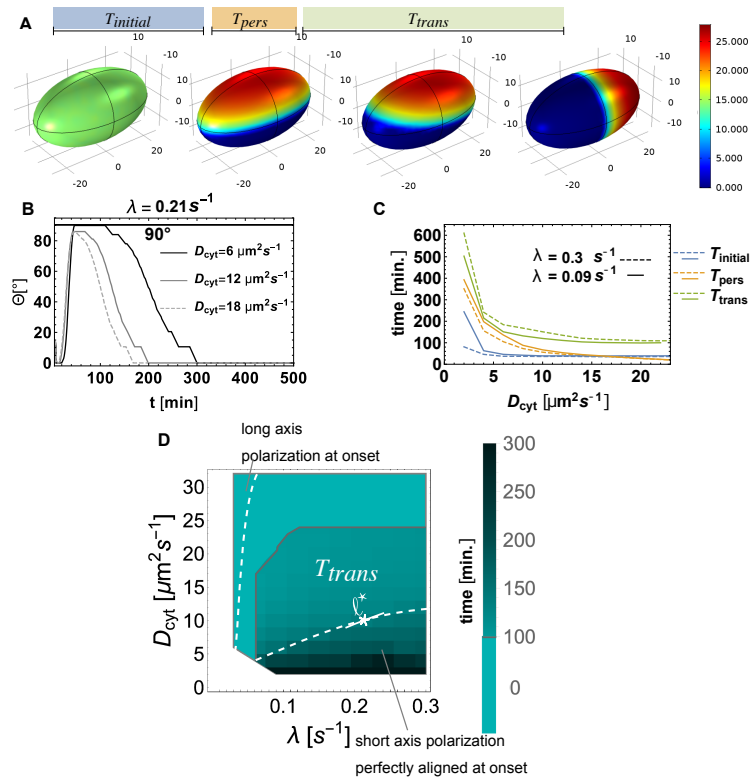


Figure 4.6 Cell polarisation in three dimensions. (A) Image series from FEM (Comsol) simulation for $D_{cyt} = 6 \mu\text{m}^2\text{s}^{-1}$, and reactivation rate $\lambda = 0.21 \text{ s}^{-1}$. The series illustrates the different times which are further analysed: The time from the initial aPAR-dominated unpolarised state to the initial short-axis polarisation, $T_{initial}$; the time duration of persistent short-axis polarisation, T_{pers} ; and the time the pattern takes to turn from short- to long-axis polarisation, T_{trans} . (B) The angle Θ of the concentration maximum of membrane-bound A_1 is plotted against simulation time for different D_{cyt} indicated in the graph. (C) $T_{initial}$, T_{pers} , T_{trans} plotted as a function of D_{cyt} for $\lambda = 0.09 \text{ s}^{-1}$ and $\lambda = 0.3 \text{ s}^{-1}$. (D) The magnitude of the transition time from short- to long-axis polarisation, T_{trans} , in D_{cyt} - λ parameter space; a cell was considered to be polarised along the short axis if $90^\circ - 10^\circ \leq \Theta \leq 90^\circ + 10^\circ$. The monochrome cyan-coloured region above the gray line corresponds to a parameter region where there is no short-axis polarisation, but the polarisation axis is aligned along the diagonal or long axis from the beginning. The dashed lines demarcate parameter regimes where the initial polarisation is aligned perfectly with the short axis ($\Theta = 90^\circ$) or with the long-axis, as indicated in the graph.

that an additional mechanism relevant for axis polarisation is the minimisation of the interface length. To test this hypothesis, we performed FEM simulations in different prolate and oblate geometries ; see Supplementary Section 4.7.5 and Supplementary **Figures 4.10 to 4.14** for details, and Supplementary Movies 6 to 8 (**M3d_3 to M3d_5**) for an illustration of the different stable polarisation alignments in oblate geometry. The movies are uploaded on the website of Nature Communications as Supplementary Information of our publication [32]. We find that (for a given set of

model parameters) the local diffusive protein fluxes from the cytosol to the membrane at the aPAR-pPAR interface are the same for short- and long-axis polarisation. Hence, the corresponding total fluxes scale with the length of the interface (see also Supplementary Section 4.7.6). This suggests that the mechanism responsible for long-axis stability is minimisation of protein fluxes. As a consequence, the transition times T_{trans} from short- to long-axis polarisation should also decrease with larger cytosolic protein fluxes as the maintenance of a larger interfaces becomes more costly. Indeed, FEM simulations show that changing the cytosolic diffusion constant leads to an increase in the associated cytosolic fluxes (see Supplementary Section 4.7.8 and Supplementary Figs. 7 and 8), and concomitantly to a significant decrease in the transition times T_{trans} (**Fig. 4.6 (C,D)**). Taken together, this shows that it is the interplay between membrane-to-bulk ratio and interface length minimisation due to flux (energy) minimisation that drives the selection of the polarisation axis and determines stability and robustness of this selection process.

4.4 Discussion

Here, we have addressed two linked questions concerning cell polarity in *C. elegans*: Under what conditions do cells polarise, and what determines the polarisation axis?

Polarisation in *C. elegans* is controlled by several mechanisms and their interplay: an initial polarisation cue of the centrosome, contraction of the actomyosin network and the PAR reaction-diffusion system which leads to polarisation in a self-organised manner but also interacts with the centrosome as well as with the actomyosin network. Recent research has further revealed some redundant pathways for the reaction-diffusion system depending on other proteins such as CHIN-1, LGL-1 and Cdc42 [53, 68, 69, 94]. In view of this complexity, it is constructive to disentangle all individual building blocks, mechanical as well as kinetic, and investigate each separately in order to properly identify the underlying mechanisms which (i) leads to polarisation and (ii) aligns it with the long axis. With our work we could now shed light on polarisation and its alignment by the PAR reaction-diffusion system in 2d and in 3d. We expect the insights gained to be essential elements for a future three-dimensional model which combines the reaction-diffusion system with mechanical effects to quantitatively understand pattern formation in the *C. elegans* embryo.

Previous experiments supported by mathematical models in simplified cell geometry have indicated that balance between mutual phosphorylation of aPAR and pPAR proteins is a key mechanism responsible for cell polarisation [26, 31, 83, 84]. Our theoretical results in realistic cell geometry support this finding. In addition, we have shown that robustness of cell polarity to variations in the phosphorylation rates increases if the scaffold protein PAR-3 is more abundant than PKC-3, which phosphorylates pPARs. Hence, low scaffold abundance is incompatible with robust biological function. This agrees with experimental findings that the scaffold function of PAR-3 is at least partially supported by other proteins (e.g. Cdc-42 [55]). Our results suggest that it would be worthwhile to experimentally search for other scaffold proteins and test their functional roles in axis selection.

Most importantly, our theoretical analysis in realistic cell geometry reveals that the key processes for axis selection are cytosolic, specifically the cytosolic diffusion and an inactive (phosphorylated) phase of PAR-3 and PAR-2 after detachment from the membrane. The reactivation time (λ^{-1}) implies a cytosolic reactivation length $\ell = \sqrt{D_{\text{cyt}}/\lambda}$ which defines a cytosolic zone of inactive proteins close to the membrane. Proteins with a short reactivation length remain partially caged at the cell poles after membrane detachment, while those with a large reactivation length are uncaged and thereby become uniformly distributed in the cytosol before rebinding. Similarly, proteins lacking a delay, like the PAR-6 PKC-3 complex, are available for rebinding immediately after detachment from the membrane and are thus strongly caged to the cell poles.

Our theoretical analysis in a two-dimensional elliptical geometry shows that only for a sufficiently large cytosolic reactivation length ℓ does the long axis become the preferred polarisation axis, at onset as well as for the steady state. For the onset of polarisation, starting from a spatially homogeneous protein distribution, this result is fully transferable to a three-dimensional prolate spheroid. However, in such a realistic cell geometry, the length of the aPAR-pPAR interface also becomes important for the stability of the polarisation axis. Our simulation results suggest an (approximate) extremal principle: The dynamics tries to minimise the interface length such that for physiologically relevant geometries the long axis is always stable. Initial metastable short-axis polarisation is observed if the reactivation length ℓ is small (fast reactivation) such that proteins exhibit caging at the polar zones. In that regime, the transition times from short-axis to long-axis polarisation can be of the order of several hours. In contrast, if $\ell/L \gtrsim 0.3$ this time can be as short as 10min. This implies that without guiding cues the reaction-diffusion system requires a sufficiently slow phosphorylation-dephosphorylation cycle and a sufficiently large diffusion constant for fast and robust long-axis polarisation.

Furthermore, how slow reactivation and how fast cytosolic diffusion need to be in order to efficiently and robustly establish and maintain long-axis polarisation depends on the ratio of PAR-3 proteins to the PAR-6 PKC-3 complex: a larger cytosolic pool of PAR-3 attenuates the effect of selecting the interface at midplane and at the same time strengthens the tendency of PKC-3 to put the interface at the poles. Hence we predict that increasing the number of PAR-3 should destabilise long-axis polarisation in favour of short-axis polarisation.

On a broader perspective, these results show that selection of a characteristic wavelength for a pattern and selection of a polarity axis are distinct phenomena and are, in general, mediated by different underlying mechanisms. We expect the following findings to be generic for mass-conserved intracellular protein systems: local membrane-to-bulk ratio and the length of interfaces between different protein domains act as geometric cues for protein pattern formation, and an activation-deactivation as well as cytosolic protein reservoirs alter the sensitivity to cell geometry. Identifying the biochemical steps that are most relevant for axis selection in other intracellular pattern forming systems is an important theme for future research.

4.5 Methods

4.5.1 Model

First we introduce and discuss the mathematical formulation and analysis of the reaction-diffusion model for PAR protein dynamics. To account for a realistic cell geometry we use, similar as in previous studies of the Min system [35], a two-dimensional elliptical geometry where the boundary of the ellipse ($\partial\Omega$) represents the membrane and the interior (Ω) represents the cytosol. Attachment-detachment processes are encoded by nonlinear reactive boundary conditions as introduced in Ref. [35]. Protein interactions are assumed to be bimolecular reactions that follow mass-action law kinetics. In the following a species identifies a mass- conserved protein type, whereas a component indicates the subgroup of proteins in a specific state, such as e.g. ‘phosphorylated’ (‘inactive’) or ‘membrane bound’.

4.5.2 Cytosolic dynamics

Proteins in the cytosol are all assumed to diffuse with the same diffusion constant, $D_{\text{cyt}} = 30 \mu\text{m}^2\text{s}^{-1}$ (see also Table 4.1). In addition, we consider dephosphorylation (reactivation) of phosphorylated proteins with an activation (dephosphorylation) rate $\lambda = 0.05/\text{s}$ (see also Table 4.1). The cytosolic concentration of each protein type X is denoted by c_X in its active form and by c_{X^*} in its inactive form (if applicable). The dynamics of the bulk components are thus given by the following set of reaction-diffusion equations:

$$\partial_t c_{A_1} = D_{\text{cyt}} \nabla^2 c_{A_1} + \lambda c_{A_1^*}, \quad (4.3)$$

$$\partial_t c_{A_1^*} = D_{\text{cyt}} \nabla^2 c_{A_1^*} - \lambda c_{A_1^*}, \quad (4.4)$$

$$\partial_t c_{A_2} = D_{\text{cyt}} \nabla^2 c_{A_2}, \quad (4.5)$$

$$\partial_t c_P = D_{\text{cyt}} \nabla^2 c_P + \lambda c_{P^*}, \quad (4.6)$$

$$\partial_t c_{P^*} = D_{\text{cyt}} \nabla^2 c_{P^*} - \lambda c_{P^*}, \quad (4.7)$$

where ∇^2 is the Laplacian in the two-dimensional bulk.

4.5.3 Membrane dynamics

On the membrane all species are assumed to diffuse with the respective diffusion constant, $D_{\text{mem}}^{\text{a}} = 0.28 \mu\text{m}^2\text{s}^{-1}$ and $D_{\text{mem}}^{\text{p}} = 0.15 \mu\text{m}^2\text{s}^{-1}$ for aPARs and pPARs (see also Table 4.1). With m_X we denote the membrane-bound concentration of protein X . Then, the bimolecular reactions discussed above (see **Fig. 4.1**) translate into the following set of reaction-diffusion equations:

$$\partial_t m_{A_1} = D_{\text{mem}}^a \nabla_{\parallel}^2 m_{A_1} + k_a^{\text{on}} c_{A_1} - k_a^{\text{off}} m_{A_1} - k_{\text{Ap}} m_P m_{A_1} - k_d m_{A_1} c_{A_2}, \quad (4.8)$$

$$\partial_t m_{A_{12}} = D_{\text{mem}}^a \nabla_{\parallel}^2 m_{A_{12}} - k_a^{\text{off}} m_{A_{12}} + k_d m_{A_1} c_{A_2} - k_{\text{Ap}} m_P m_{A_{12}}, \quad (4.9)$$

$$\partial_t m_P = D_{\text{mem}}^p \nabla_{\parallel}^2 m_P + k_p^{\text{on}} c_P - k_p^{\text{off}} m_P - k_{\text{Pa}} m_{A_{12}} m_P, \quad (4.10)$$

where ∇_{\parallel}^2 is the Laplacian operator on the boundary $\partial\Omega$, i.e. on the membrane.

4.5.4 Reactive boundary conditions

The membrane dynamics and cytosolic dynamics are coupled through reactive boundary conditions. These describe the balance between diffusive fluxes ($D_{\text{cyt}} \nabla_{\perp}$ acting on cytosolic concentration) and attachment and detachment processes between membrane and cytosol:

$$D_{\text{cyt}} \nabla_{\perp} c_{A_1} = k_a^{\text{off}} (m_{A_1} + m_{A_{12}}) - k_a^{\text{on}} c_{A_1} \quad (4.11)$$

$$D_{\text{cyt}} \nabla_{\perp} c_{A_2} = (k_{\text{Ap}} m_P + k_a^{\text{off}}) m_{A_{12}} - k_d c_{A_2} m_{A_1} \quad (4.12)$$

$$D_{\text{cyt}} \nabla_{\perp} c_P = k_p^{\text{off}} m_P - k_p^{\text{on}} c_P \quad (4.13)$$

$$D_{\text{cyt}} \nabla_{\perp} c_{A_1^*} = k_{\text{Ap}} m_P (m_{A_1} + m_{A_{12}}) \quad (4.14)$$

$$D_{\text{cyt}} \nabla_{\perp} c_{P^*} = k_{\text{Pa}} m_P m_{A_{12}} \quad (4.15)$$

where ∇_{\perp} is the Nabla operator perpendicular to the boundary, such that $D_{\text{cyt}} \nabla_{\perp}$ is the flux operator between cytosol and membrane.

4.5.5 Mass conservation

On the time scale of establishment and maintenance of polarisation in *C. elegans*, PAR protein production and degradation are negligible. Hence, the total number N_X of each protein species $X \in \{A_1, A_2, P\}$ is conserved. It can be obtained by integrating the average densities over the whole space or by integrating the space-dependent cytoplasmic concentrations and membrane concentrations over Ω and $\partial\Omega$, respectively:

$$N_{A_1} = \int_{\Omega} \rho_{A_1} = \int_{\Omega} (c_{A_1} + c_{A_1^*}) + \int_{\partial\Omega} (m_{A_1} + m_{A_{12}}), \quad (4.16)$$

$$N_{A_2} = \int_{\Omega} \rho_{A_2} = \int_{\Omega} c_{A_2} + \int_{\partial\Omega} m_{A_{12}}, \quad (4.17)$$

$$N_P = \int_{\Omega} \rho_P = \int_{\Omega} (c_P + c_{P^*}) + \int_{\partial\Omega} m_P, \quad (4.18)$$

where \int_{Ω} and $\int_{\partial\Omega}$ denote integrals over the interior and the boundary of the ellipsoid, respectively.

4.5.6 Linear Stability Analysis

In the following we outline the main steps required to perform a linear stability analysis (LSA) in elliptical geometry, emphasising the major differences relative to the well known stability analysis in planar system geometries with no bulk-boundary coupling (see e.g. a didactic derivation of linear stability analysis written by Cross and Greenside [12]). A detailed derivation of LSA in elliptical geometry can be found in the Supplementary Information of Halatek et al. [35].

4.5.7 Reaction-diffusion equations in elliptical geometry

A LSA yields the initial dynamics of a system perturbed from any of its steady states. In the context of pattern formation in reaction-diffusion systems this is typically a uniform steady state. The eigenfunctions of the linearised system (around the steady state) serve as an orthogonal basis in which any perturbation can be expressed. In planar systems these are simply Fourier modes, e.g. $\sim \cos(qx)$ with spatial variable x and wavenumber q , where q is chosen such that boundary conditions are satisfied. The LSA then yields the temporal eigenvalues σ_q (growth rates) for each wavenumber that express exponential growth or decay, and possible oscillation (if the imaginary part $\Im[\sigma_q] \neq 0$) of the respective eigenfunction $\exp(\sigma_q t) \cos(qx)$. Hence, the main objective is (i) to derive the eigenfunctions for the linearised system in the corresponding geometry, and (ii) to calculate the associated growth rates (real parts $\Re[\sigma_q]$), where positive growth rates signify formation of patterns with wavelength $\sim 1/q$.

For reaction-diffusion systems with bulk-boundary coupling in elliptical geometry there are three major complications with this approach.

Due to bulk-boundary coupling, we are faced with two separate sets of reaction–diffusion equations. One set is defined in the bulk and accounts for the dynamics in the cytosol. Here reactions are assumed to be linear (first order kinetics) and typically account for nucleotide exchange or (de-)phosphorylation, Eq. (4.3) – Eq. (4.7). The second set is defined on the boundary and accounts for the dynamics on the membrane (or cell cortex) including diffusion and reaction, Eq. (4.8) – Eq. (4.10).

The first complication arises as follows: Given orthogonal elliptical coordinates

$$x = d \cosh \mu \cos \nu, \quad (4.19)$$

$$y = d \sinh \mu \sin \nu, \quad (4.20)$$

with ‘radial’ variable $\mu > 0$, ‘angular’ variable $0 \leq \nu < 2\pi$, and elliptical eccentricity $d = \sqrt{a^2 - b^2}$ (with long half-axis a and short half-axis b), the diffusion operator in the bulk $D_{\text{cyt}} \nabla^2$ reads:

$$D_{\text{cyt}} \frac{1}{d^2(\sinh^2 \mu + \sin^2 \nu)} (\partial_\mu^2 + \partial_\nu^2). \quad (4.21)$$

On the boundary the diffusion operator $D_{\text{mem}} \nabla_{\parallel}^2$ acts along constant $\mu = \mu_0 = \arctan(b/a)$ and reads:

$$D_{\text{mem}} \left(- \frac{\cos \nu \sin \nu}{d (\sinh^2 \mu_0 + \sin^2 \nu)^{3/2}} \partial_{\nu} + \frac{1}{d^2 (\sinh^2 \mu_0 + \sin^2 \nu)} \partial_{\nu}^2 \right). \quad (4.22)$$

Due to these different diffusion operators the sets of reaction–diffusion equations in the bulk and on the boundary do not share the same set of canonical eigenfunctions (i.e. eigenfunction obtained from separation of variables). To overcome this problem the diffusion on the membrane can be more conveniently expressed in arclength parametrisation $s(\nu)$:

$$s(\nu) = \int_0^{\nu} d\tilde{\nu} \sqrt{b^2 + (a^2 - b^2) \sin^2 \tilde{\nu}}. \quad (4.23)$$

Then, the diffusion operator $D_{\text{mem}} \nabla_{\parallel}^2$ simplifies to $D_{\text{mem}} \partial_s^2$, and the eigenfunctions are obtained as

$$\Psi_{e,n}^{\text{mem}}(\mu_0, s(\nu)) = \cos \left(\frac{2\pi n}{S} s(\nu) \right), \quad (4.24)$$

$$\Psi_{o,n}^{\text{mem}}(\mu_0, s(\nu)) = \sin \left(\frac{2\pi n}{S} s(\nu) \right), \quad (4.25)$$

with the circumference of the ellipse $S = s(2\pi)$. The goal is then to express these functions in terms of the orthogonal eigenfunctions of the bulk problem — the Mathieu functions, here denoted by $\Psi(\nu)$ and $R(\mu)$ — which are obtained as solutions of the Mathieu equations:

$$0 = \partial_{\nu}^2 \Psi(\nu) + [\alpha - 2q \cdot \cos(2\nu)] \Psi(\nu) \quad (4.26)$$

$$0 = \partial_{\mu}^2 R(\mu) - [\alpha - 2q \cdot \cosh(2\mu)] R(\mu). \quad (4.27)$$

Here α is a constant of separation, and

$$q = -(\sigma + \lambda) \frac{d^2}{4D_{\text{cyt}}} \quad (4.28)$$

denotes a dimensionless parameter (not to be confused with a wavenumber!). For small q , analytical approximations of the Mathieu functions can be obtained [35, 101] and matched with the eigenfunctions $\Psi_{e,n}^{\text{mem}}$ and $\Psi_{o,n}^{\text{mem}}$ at the boundary $\mu = \mu_0$.

The second complication is a consequence of the coupling between bulk and boundary processes through the reactive boundary condition, see e.g. the model equations Eq. (4.11) – Eq. (4.15). This coupling introduces an explicit dependence of the linearised system on the (derivative of the) radial eigenfunctions $R(\mu)$ (see Ref. [35]),

which, in turn, depends on the temporal eigenvalues σ in a non-algebraic fashion. Usually, the final step in any LSA is the solution of a characteristic equation $0 = f(\sigma)$, which is typically polynomial in σ . Due to the bulk-boundary coupling this is no longer the case (irrespective of the geometry, see e.g. Ref. [13]; the characteristic equation is transcendental and can only be solved numerically for each parameter combination [35]. Therefore, it is not possible to derive a general stability criterion analogous to that known for planar systems without bulk-boundary coupling [12]. We further note that the boundary condition introduces a coupling between the angular eigenfunctions $\Psi(\nu)$, which, however, is small and can be neglected [35].

The final complication arises as consequence of the cytosolic reactivation cycle. This cycle generically precludes the existence of a uniform steady state (including states uniform along the boundary). The origin of this symmetry adaption process has been discussed in Ref. [36]. Following Ref. [35] we approximate the near-uniform steady state with the eigenfunction that is constant along the boundary, i.e. $\Psi_{e,0}^{\text{mem}}(\mu_0, s(\nu))$. In this case nonlinearities (which are restricted to the boundary) do not induce mode coupling, which would otherwise complicate the LSA.

4.5.8 Finite Element Simulations (FEM)

Linear stability analysis can only predict the onset of pattern formation. In order to understand the full nonlinear protein dynamics and to determine the steady states corresponding to given parameter sets we further performed finite element (FEM) simulations on a triangular mesh using Comsol Multiphysics 5.1 - 5.4 (updating versions).

4.5.9 Setup for FEM simulations

As time-dependent solver in Comsol Multiphysics we chose PARDISO with a multithreaded nested dissection. The time stepping was performed with a relative tolerance of 10^{-6} between time steps and solved with a multistep method (BDF). In all simulations we used triangular meshing (setting ‘finer’) with additional refinement at the boundary, i.e. along the membrane. As for the linear stability analysis, if not specified otherwise, the parameters for the FEM simulations can be found in Table 4.1. For the standard parameter sets given in Table 4.1, we ran the simulation up to $5 \cdot 10^6 s$. Since the system reached the steady state for most parameter sets at the latest after $5 \cdot 10^5 s$, we limited simulation times for large parameter sweeps at $10^6 s$.

4.5.10 The critical reactivation rate

The 2d FEM sweep of λ versus D_{cyt} was initialised with a random initial perturbation of the stationary state with high aPAR concentration on the membrane. The initial perturbation was implemented by drawing a random number $\text{rand}(x, y)$ from a normal

distribution with zero mean and unit variance and multiplying the membrane concentration of aPARs by $(1 + 0.01 \cdot \text{rand}(x, y))$ and that of pPARs by $(1 - 0.01 \cdot \text{rand}(x, y))$, i.e. we perturbed the initial condition randomly by 1%. The parameter sweep was performed varying λ from $5 \cdot 10^{-3} \text{ s}^{-1}$ to 0.3 s^{-1} in steps of $5 \cdot 10^{-3} \text{ s}^{-1}$ and varying D_{cyt} from $6 \mu\text{m}^2 \text{ s}^{-1}$ to $40 \mu\text{m}^2 \text{ s}^{-1}$ with a uniform spacing of $2 \mu\text{m}^2 \text{ s}^{-1}$.

We further performed two test simulations (sweeping λ and D_{cyt}) which were initialised with linear gradients. These implementations were intended to uncover dependencies of the final pattern on the initial perturbation. In the first sweep, the gradient was oriented along the long-axis, i.e. the aPAR concentrations were multiplied by $(1 + 0.1 \cdot x/a)$ and the pPAR concentrations by $(1 - 0.1 \cdot x/a)$. In the second sweep the gradient was oriented along the short-axis, i.e. the aPAR concentrations were multiplied by $(1 + 0.1 \cdot y/b)$ and the pPAR concentrations by $(1 - 0.1 \cdot y/b)$. We found that the steady state polarisation was the same as with small random perturbations. Initial linear gradients with the ‘wrong?’ alignment only lead to a transient polarisation along the same axis as the initially imposed gradient but then turned to the same polarisation axis as with the random initial perturbation.

Furthermore, we checked the linear stability analysis sweeps on k_{Ap} and k_{Pa} in **Fig. 4.4** using FEM simulations. The explicit parameter sets k_{Ap} and k_{Pa} used for probing FEM simulations are shown in Tables 4.2 and 4.3. 2d FEM simulations confirm that there λ is the decisive parameter that determines the polarisation axis and not k_{Ap} and k_{Pa} .

In order to find ℓ^*/L in steady state for different combinations of density ratios shown in **Fig. 4.5**, we performed FEM sweeps of k_{Pa} (for fixed $k_{\text{Ap}} = 0.4 \mu\text{m} \text{ s}^{-1}$) and λ (for fixed $D_{\text{cyt}} = 30 \mu\text{m}^2 \text{ s}^{-1}$) at first in broad steps (the steps for λ were initiated with $5 \cdot 10^{-3} \text{ s}^{-1}$ and those for k_{Pa} with $0.2 \mu\text{m} \text{ s}^{-1}$). As soon as we identified a regime of parameters for ℓ^*/L where long-axis polarisation turned to short-axis polarisation, we used finer steps, with the step size being chosen in accordance with the cone size of each of the $k_{\text{Pa}}/k_{\text{Ap}}$ versus ℓ^*/L cones in **Fig. 4.5**.

4.5.11 FEM simulations for 3d system

In 3d FEM simulations for all sweeps were initiated with an initial *aPAR*-dominant concentration on the membrane and 1% random perturbation thereof. All parameters are shown in Table 4.4. For the sweep of λ versus D_{cyt} resulting in the data discussed in the main text and **Fig. 4.6** the parameter range was set to $D_{\text{cyt}} = 2 - 32 \mu\text{m}^2 \text{ s}^{-1}$ in steps of $2 \mu\text{m}^2 \text{ s}^{-1}$, and reactivation rate $\lambda = 0.03 - 0.3 \text{ s}^{-1}$ in steps of 0.03 s^{-1} . The full region of the formation of any pattern can be found by using the feature that the absolute value of membrane gradients is zero for a homogeneous distribution on the membrane and a positive number for inhomogeneous (patterned) protein distributions on the membrane. To distinguish between long and short axis patterns the FEM simulations were analysed by investigating (i) the angle of the concentration maxima on the membrane in ellipsoidal coordinates (which is 90° for perfect short axis polarisation and $0/180^\circ$ for perfect long axis polarisation) and additionally (ii) the distance between the concentration maximum of P and A_1 on the membrane (which is $2 \cdot a = 54 \mu\text{m}$ for

long axis polarisation and $2 \cdot b = 30 \mu m$ for short axis polarisation). For a final check, the pattern dynamics was sampled by eye to ensure that these criteria work. In order to numerically investigate the onset of long axis polarisation - which is very sensitive to λ - a finer sweep was additionally performed with $D_{\text{cyt}} = 2 - 32 \mu m^2 s^{-1}$ in steps of $2 \mu m^2 s^{-1}$, and reactivation rate $\lambda = 0.015 - 0.01 s^{-1}$ in steps of $0.005 s^{-1}$. To find the boundary for a polarity onset with long axis alignment we filtered for a short axis and a diagonal onset.

4.6 Tables for the main sections

| | | | | | | |
|--------------------------------|---|---|--|---------------------------------------|-------------------------------|-------------------------------|
| $a[\mu m]$ | $b[\mu m]$ | $D_{\text{cyt}}[\mu m^2 s^{-1}]$ | $k_{\text{a/p}}^{\text{on}}[\mu m s^{-1}]$ | $k_{\text{a/p}}^{\text{off}}[s^{-1}]$ | $k_{\text{Ap}}[\mu m s^{-1}]$ | $k_{\text{Pa}}[\mu m s^{-1}]$ |
| 27 | 15 | 30 | 0.1 | 0.005 | 0.4 | 1.2 |
| $k_{\text{d}}[\mu m^2 s^{-1}]$ | $D_{\text{mem}}^{\text{a}}[\mu m^2 s^{-1}]$ | $D_{\text{mem}}^{\text{p}}[\mu m^2 s^{-1}]$ | $\lambda[s^{-1}]$ | $\rho_{A_1}[\mu m^{-2}]$ | $\rho_{A_2}[\mu m^{-2}]$ | $\rho_P[\mu m^{-2}]$ |
| 0.034 | 0.28 | 0.15 | 0.3 | 8.0 | 2.5 | 8.0 |

Table 4.1 Parameters used to create **Fig. 4.3 - 4.5**.

Fig. 4.3: For the sweep using linear stability analysis in **Fig. 4.3 (C)** all parameters but λ and D_{cyt} were chosen as shown in this Table. λ was varied between $5 \cdot 10^{-3} s^{-1}$ and $0.35 s^{-1}$ with a uniform spacing of $5 \cdot 10^{-3} s^{-1}$. D_{cyt} was varied from $6 \mu m^2 s^{-1}$ to $38 \mu m^2 s^{-1}$ with a uniform spacing of $2 \mu m^2 s^{-1}$. **Fig. 4.4:** For the linear stability analysis sweep in **Fig. 4.4 (A,B)** all parameters but λ and k_{Ap} and k_{Pa} were chosen as above. k_{Ap} was varied between $0.02 \mu m s^{-1}$ and $0.8 \mu m s^{-1}$ and k_{Pa} was varied between $0.06 \mu m s^{-1}$ and $1.6 \mu m s^{-1}$; for both parameters values were uniformly spaced with distance $0.02 \mu m s^{-1}$. **Fig. 4.5:** For the linear stability analysis sweeps in **Fig. 4.5** all parameters but the densities ρ_{A_1} , ρ_{A_2} and ρ_P , λ and k_{Ap} were set as shown above. For all triples of densities $\rho_{A_2} = [\mu m^{-2}]$ while ρ_{A_1} and ρ_P were varied accordingly. The simultaneous sweep of ℓ and $k_{\text{Pa}}/k_{\text{Ap}}$ was obtained by varying λ and k_{Pa} for fixed $D_{\text{cyt}} = 30 \mu m^2 s^{-1}$ and $k_{\text{Ap}} = 0.4 \mu m s^{-1}$. The values of ℓ were uniformly spaced from $2 \mu m$ to $62 \mu m$ with distance $2 \mu m$. The ratio $k_{\text{Pa}}/k_{\text{Ap}}$ was varied from 0.7 to 8.0 with uniform steps of 0.05.

| k_{Ap} | k_{Pa} | steady state | onset |
|----------|----------|-------------------------|------------|
| 0.44 | 1.68 | no pattern | no pattern |
| 0.46 | 1.62 | no pattern | no pattern |
| 0.48 | 1.56 | no pattern | no pattern |
| 0.5 | 1.5 | short-axis polarisation | short-axis |
| 0.52 | 1.44 | short-axis polarisation | short-axis |
| 0.54 | 1.38 | short-axis polarisation | short-axis |
| 0.56 | 1.32 | short-axis polarisation | long-axis |
| 0.58 | 1.26 | short-axis polarisation | long-axis |
| 0.6 | 1.2 | no pattern | no pattern |

Table 4.2 FEM sample sweeps of k_{Ap} , k_{Pa} with small initial perturbation (1%) for $\lambda = 0.3s^{-1}$.

| k_{Ap} | k_{Pa} | steady state | onset |
|----------|----------|------------------------|------------|
| 0.44 | 1.68 | no pattern | no pattern |
| 0.46 | 1.62 | no pattern | no pattern |
| 0.48 | 1.56 | no pattern | no pattern |
| 0.5 | 1.5 | long-axis polarisation | long-axis |
| 0.52 | 1.44 | long-axis polarisation | long-axis |
| 0.54 | 1.38 | long-axis polarisation | short-axis |
| 0.56 | 1.32 | long-axis polarisation | short-axis |
| 0.58 | 1.26 | long-axis polarisation | short-axis |
| 0.6 | 1.2 | no pattern | no pattern |

Table 4.3 FEM sample sweeps of k_{Ap} , k_{Pa} with small initial perturbation (1%) for $\lambda = 0.05s^{-1}$

| | | | | | | | |
|-----------------------|------------------------------------|------------------------------------|-------------------------------------|--------------------------------|--------------------------|--------------------------|-----|
| $a[\mu m]$ | $b[\mu m]$ | $D_{\text{cyt}}[\mu m^2 s^{-1}]$ | $k_{a/p}^{\text{on}}[\mu m s^{-1}]$ | $k_{a/p}^{\text{off}}[s^{-1}]$ | $k_{Ap}[\mu m^2 s^{-1}]$ | $k_{Pa}[\mu m^2 s^{-1}]$ | 1.2 |
| | 27 | 15 | 30 | 0.1 | 0.005 | 0.4 | |
| $k_d[\mu m^3 s^{-1}]$ | $D_{\text{mem}}^a[\mu m^2 s^{-1}]$ | $D_{\text{mem}}^p[\mu m^2 s^{-1}]$ | $\lambda[s^{-1}]$ | $\rho_{A_1}[\mu m^{-3}]$ | $\rho_{A_2}[\mu m^{-3}]$ | $\rho_P[\mu m^{-3}]$ | 8.0 |
| | 0.034 | 0.28 | 0.15 | 0.3 | 8.0 | 2.5 | |

Table 4.4 Parameters for three-dimensional FEM simulations. For the sweeps shown in **Fig. 4.6** all parameters but λ and D_{cyt} were chosen as shown in this Table. λ was varied between $3 \cdot 10^{-2} s^{-1}$ and $0.3 s^{-1}$ with a uniform spacing of $3 \cdot 10^{-2} s^{-1}$. D_{cyt} was varied from $2 \mu m^2 s^{-1}$ to $32 \mu m^2 s^{-1}$ with a uniform spacing of $2 \mu m^2 s^{-1}$.

4.7 Supplementary Information

Following the structure of the main sections above, section 4.7.1 discusses further aspects of cell polarisation in two-dimensional elliptical geometry using finite element simulations: excitable region in parameter space, and time evolution of the polarisation axis. Section 4.7.2 summarises experimental information on protein numbers. In Section 4.7.3 we show why it is not sufficient to use a planar geometry in order to learn about the selection of the polarisation axis. The membrane-to-bulk ratio in two-dimensional elliptical and three-dimensional ellipsoidal geometry is summarised in section 4.7.4. In order to challenge the hypothesis of interface minimisation, in section 4.7.5 the results on axis selection in oblate and prolate geometries are discussed. To understand the relative role of the activation-deactivation cycle and interface minimisation an extensive set of finite element simulations was performed and the results are discussed. Sections 4.7.6 and 4.7.7 show that interface minimisation arises from flux minimisation. Finally, in section 4.7.8 patterning time scales are provided and discussed.

4.7.1 Stimulus-induced polarisation and transient polarisation alignment

In the wild type *C. elegans* embryo polarisation is established by an interplay between mechanical cues (forces of the centrosome after male sperm entry and actomyosin contraction towards the anterior) and the PAR reaction diffusion system. In the main text we focused on spontaneous pattern formation facilitated by a Turing instability. Here, we investigate whether the Turing instability is subcritical, i.e. whether patterns can be induced (stimulated) by large perturbations outside the Turing unstable region, such as the fertilisation event. To this end, we performed FEM simulations that were initiated with linear concentration gradients along the membrane as initial conditions. The gradient was chosen to favour selection of a pattern aligned with the same polarisation axis as predicted by linear stability analysis.

Specifically, for $\lambda = 1s^{-1}$ (fast reactivation) shown in **Fig. 4.7(A)** top row, the gradient was chosen along the short axis, i.e. the aPAR concentrations were multiplied by $(1 + y/b)$ and the pPAR concentrations by $(1 - y/b)$, where $2b$ is the length of the short axis. For $\lambda = 0.05s^{-1}$ (slow reactivation) shown in **Fig. 4.7(B)** top row, the gradient was aligned along the long axis, i.e. the aPAR concentrations was multiplied with $(1 + x/a)$ and the pPAR concentrations with $(1 - x/a)$, where $2a$ is the length of the long axis. Indeed, in both cases we found a large parameter domain outside the regime of spontaneous polarisation where pattern formation can be triggered by finite perturbations. The specific sets (k_{AP}, k_{Pa}) for which the system was tested for stimulus-induced pattern formation are provided in the Tables 4.5, 4.6 and 4.7. In Supplementary **Figure 4.7** we extrapolated from this data to find an outer cone of the excitable region (dashed lines in the k_{AP} - k_{Pa} diagrams).

Furthermore, in the Turing unstable regime we tested alignment of polarisation when the initial condition in the FEM simulation was chosen to select for the pattern orthogonal to the polarisation axis predicted by linear stability analysis. For all sets

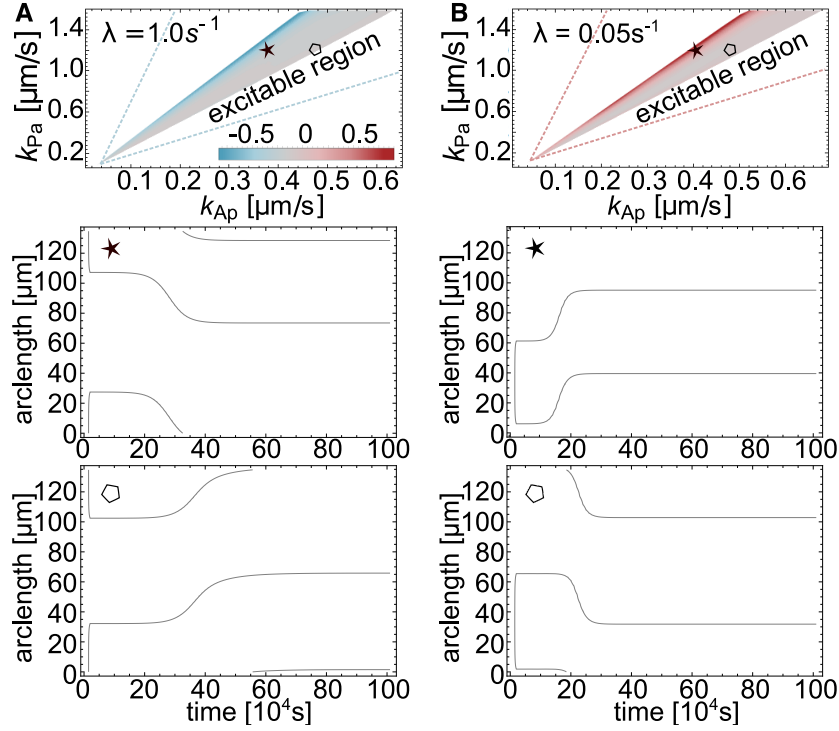


Figure 4.7 Testing the steady state polarity axis with initial gradients. **(A,B)** top row: Investigation of excitable region. The cones show the results of a linear stability analysis in the 2d ellipse as a function of k_{Ap} and k_{Pa} with the color code indicating the normalised difference of the first even and odd growth rate, $\delta\sigma$ (same color code as in **Fig. 4.4** of the main text, i.e. even mode grows faster: red, odd mode grows faster: blue, $\delta\sigma \approx 0s^{-1}$: gray). These Turing-unstable regions are flanked by parameter regimes (bounded by dashed lines), where patterns can only be induced by a large enough stimulus acting on the uniform state; we call this the excitable region. Parameters as in Table 1 of the main text. **(A,B)** Middle and bottom row: Investigation of polarisation re-alignment. The black lines indicate the interface position between aPAR and pPAR domain. Shown are sample interface trajectories from FEM simulations for parameters at the upper (star) and lower (hexagon) bound of the Turing-unstable regime. In contrast to the top row of the Figure, here the FEM simulations were initialised with gradients aligned perpendicularly to the predicted pattern orientation (gradients as above, but orthogonal to predicted polarisation alignment, for mathematical definition see text). We find that the initial polarisation axis is aligned with the initial gradient while the final pattern is dictated by the reactivation cycle. k_{Ap} and k_{Pa} do not impact this qualitatively but only the transition time from one to the other polarisation axis.

of parameters (k_{Ap} , k_{Pa}) which we tested we found that the final steady state was the same as the one predicted by linear stability analysis (at the upper bound of (k_{Pa} , k_{Ap}) where $\delta\sigma$ is decisively above or below zero). However, a transiently lasting polarisation along the axis of the initial gradient was observed (see Supplementary **Fig. 4.7** middle and bottom row). In detail, for fast $\lambda = s^{-1}$ the initial gradient is aligned with the

long axis, i.e. the original aPAR concentrations were multiplied with $(1 + x/a)$ and the pPAR concentrations with $(1 - x/a)$. Polarisation establishes along the long axis first (for both pairs of (k_{Ap}, k_{Pa}) in Supplementary **Fig. 4.7**, "star" and "hexagon"), and then transitions to align with the short axis where it then finds its steady state. This turning of the polarisation axis starts later for lower k_{Pa}/k_{Ap} ratios (compare Supplementary **Fig. 4.7**, bottom row). For slow $\lambda = 0.05s^{-1}$ we find just the opposite behaviour: Initial short axis polarisation establishes aligned with the gradient but then turns towards steady state long axis polarisation. The time of turning again depends on the ratio k_{Pa}/k_{Ap} .

4.7.2 Total and relative protein numbers

For the PAR protein system in *C. elegans*, many parameters have been measured including relative and total protein numbers, binding and unbinding rates, and diffusion constants of proteins on the membrane [26, 31, 100, 102]. However, measurements of the PAR protein density were reported with a relatively large uncertainty; according to the Supplementary Information in Ref. [31] with a relative error larger than 20%. Most recent experiments report total PAR protein densities between 2 and 6 proteins per μm^3 if all proteins were evenly distributed in the cytosol (depending on the specific PAR protein) [100]. We used the corresponding order of magnitude of total protein numbers (see Table 4.1 of the main sections) for our studies and further investigated relative abundances of proteins (see the relative density variations $[P]/[A_2]$ and $[A_1]/[A_2]$ discussed in Section "Axis selection depends on relative protein densities") and **Fig. 4.5** in the main sections).

4.7.3 Planar geometry: the characteristic length scale does not select the axis

Is it possible to simplify the geometry of a cell in order to answer the question of axis selection for cell polarisation? A heuristic argument in favour of a positive answer would be: Let's simplify to a planar geometry as illustrated in **Fig. 4.8 (A)**, and perform a linear stability analysis. This will yield a fastest growing mode at some characteristic wavelength. Intuitively, one may now expect that in elliptical geometry those axis is selected which length fits this characteristic wavelength best. Is this intuition correct?

To answer this question, we investigated the PAR model in planar geometry and compared it with the results that we obtained in elliptical and ellipsoidal geometry (main text). The linear stability analysis was performed in a rectangular two-dimensional geometry (x, z) with variable width and fixed height h that matches the short half-axis b of the ellipsoidal cell; see **Fig. 4.8 (A)**. The membrane is at the bottom, $z = 0$, where we assume reactive boundary conditions. For symmetry reasons we assume no-flux boundary conditions at $z = b$. The details of the linear stability analysis can be found in

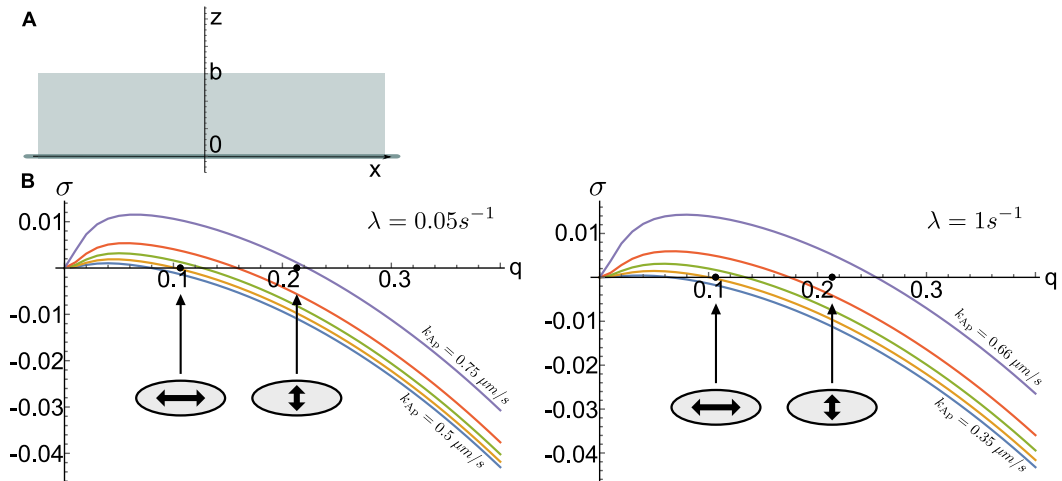


Figure 4.8 Linear stability analysis in planar geometry. (A) Illustration of a planar geometry with membrane at the bottom, $z = 0$, and cytosol of height $h = b$. (B) Dispersion relations in rectangular geometry for $\lambda = 0.05 \text{ s}^{-1}$ (left, long-axis selection in the ellipse) and $\lambda = 1 \text{ s}^{-1}$ (right, short-axis selection in the ellipse), showing that the fastest growing mode depends sensitively on k_{AP} . The filled black circles highlight the length scales corresponding to long axis polarity $q = \pi/(2a)$ and short axis polarity $q = \pi/(2b)$. Naively, the stability analysis in rectangular geometry suggests that modes with large length scale (long axis polarity) are always preferred, contradicting the correct results from the simulations and linear stability analysis in elliptical geometry.

Ref. [13]. The numerical values of all parameters are unchanged (i.e. as in Table 1 in the main text), except the attachment rates $k_{\text{a/p}}^{\text{on}}$ which we rescaled to $0.3 \mu\text{m}\cdot\text{s}^{-1}$] to recover the lateral (Turing) instability of the unpolarised aPAR state. A parameter sweep of the phosphorylation rate constant k_{AP} for $\lambda = 0.05 \text{ s}^{-1}$ (long axis selection in the ellipse) and $\lambda = 1 \text{ s}^{-1}$ (short axis selection in the ellipse) shows that the band of unstable modes and the *fastest growing mode* (the mode which determines the *characteristic length scale* at onset) sensitively depend on k_{AP} but not on λ . Furthermore, we find that the *fastest growing mode* corresponds to a *characteristic length scale* which is always longer than the short axis of the cell, $2b$, and can be tuned to fit the long axis, $2a$ (see also marks in the dispersion relation in **Fig. 4.8 (B)**). Following the heuristic argument one would conclude that the long axis is chosen for polarisation because it fits better into the cell. However, our results in the main text demonstrate that axis selection in cellular geometry is determined by cytosolic parameters such as λ and D_{cyt} , but effects by k_{AP} are negligible. Hence, we conclude that the *characteristic length scale* determined by linear stability in planar geometry does neither inform about axis selection in elliptical nor ellipsoidal geometry.

We find that pattern alignment is a process which strongly depends on the distribution of binding active proteins in the cytosol. For our model pattern alignment is not dictated by the wavelength of a pattern but rather by the reactivation length ℓ^* and

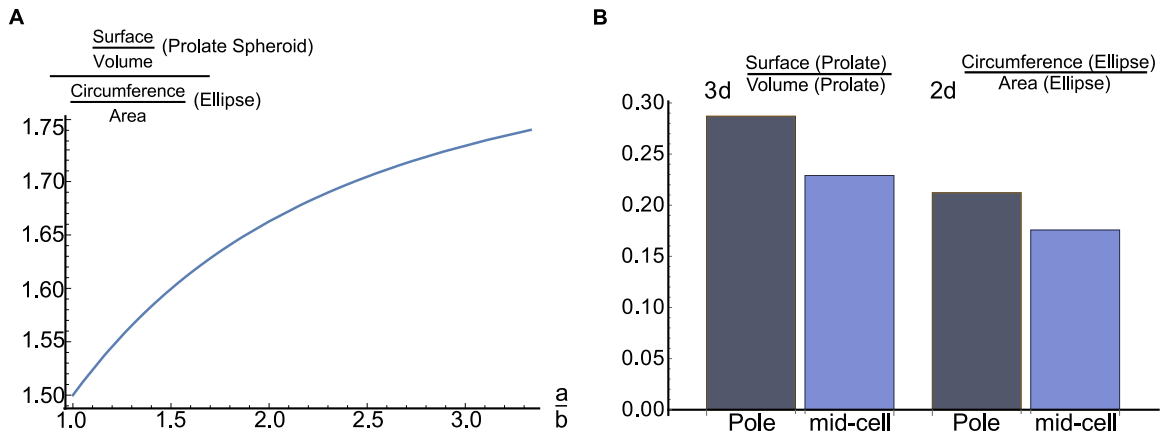


Figure 4.9 Membrane-to-bulk ratio for a two-dimensional (2d) ellipse and a three-dimensional (3d) prolate spheroid. (A) The *overall* membrane-to-bulk ratio (integrated over the whole cell boundary) of a prolate spheroid is compared to that of an ellipse with the same minor and major axes as a function of the aspect ratio a/b . (B) The *local* membrane-to-bulk ratio (as defined in the main text of the supplement) of a prolate spheroid and an ellipse, both at the cell poles and at midcell. The membrane-to-bulk ratio was calculated for some sample diffusion length $\ell_D = 7.5 \mu m$.

the topology of the domain interfaces.

4.7.4 Membrane-to-bulk ratio for ellipses and prolate spheroids

In the main text we showed that the membrane-to-bulk ratio is a key factor for axis selection, especially during the initial phase of pattern formation. How does this ratio depend on the dimensionality of the system? **Fig. 4.9 (A)** compares the *overall* membrane-to-bulk ratio — the ratio of area/circumference of the membrane to volume/area of the cytosol (‘bulk’) — for a two-dimensional ellipse and a three-dimensional prolate spheroid (ellipsoid). One observes that this ratio is in general larger for a prolate spheroid, and the surplus is increasing with the aspect ratio a/b .

The *local* membrane-to-bulk ratio varies qualitatively in a similar fashion for the two- and three-dimensional case: it is maximal at the poles and decreases monotonously towards midcell where it reaches its minimum. In order to see this quantitatively we have calculated the membrane-to-bulk ratio for a sample diffusion length ($\ell_D = 7.5 \mu m$) at the poles and at midcell for an ellipse and a prolate spheroid; see **Fig. 4.9 (B)**. To determine the membrane-to-bulk ratio at the poles, we defined a sphere with the sample diffusion length $\ell_D = 7.5 \mu m$ as radius and center at the cell pole. Then we calculated the membrane region of the ellipse (2d) or ellipsoid (3d) which lies within this sphere. This gives the membrane part of the membrane-to-bulk ratio. The bulk part was calculated by the intersecting region of the ellipse (2d) or ellipsoid (3d) with the sphere. Similarly, we defined the membrane to bulk ratio at midcell with the help of a sphere with radius ℓ_D and center at the midcell membrane. We find that

quantitatively, the change in the local membrane-to-bulk ratio from midcell to pole is more pronounced in a three-dimensional prolate spheroid than in a two-dimensional ellipse.

4.7.5 The role of interface length for the selection of the polarity axis

We argued in the main text, that axis selection during cell polarisation is determined by an interplay between two effects: The higher membrane-to-bulk ratio at the cell poles favors short-axis selection for small enough reactivation lengths ℓ . Otherwise, long-axis polarisation is favored. This is confirmed by our studies for two-dimensional ellipses; see also Method Section *The critical reactivation rate to switch steady state polarity*. On the other hand, we have argued in the main text that there is a tendency of the dynamics to minimize the length of the interface between aPAR and pPAR domains, which would always favor long-axis polarisation.

In this section we give a detailed account of FEM simulations Comsol Multiphysics 5.4 for various three-dimensional ellipsoidal geometries including both prolate and oblate spheroids; see Tables 4.8, 4.9. The goal is to clarify the relative role of the membrane-to-bulk ratio and the interface length in the axis selection process.

Perimeter ratio for long- and short-axis polarisation in prolate and oblate spheroid geometries. The interface length for short-axis polarisation, L_{short} , and long-axis polarisation, L_{long} are different for an ellipsoidal geometry.

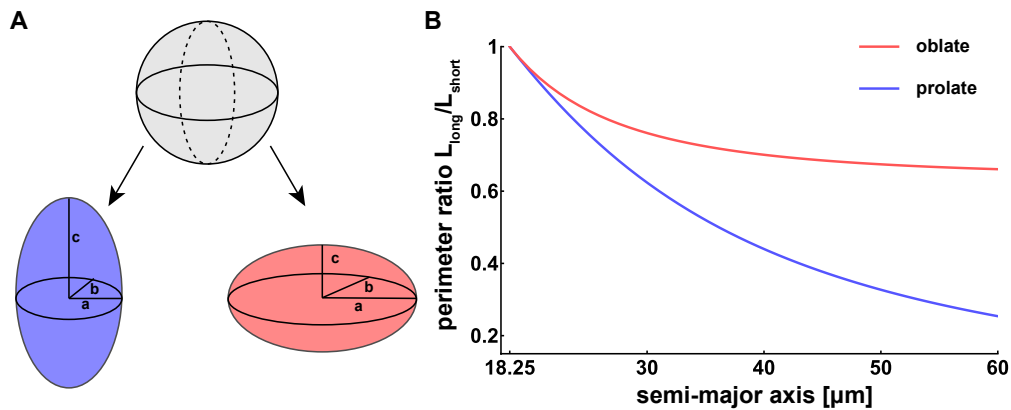


Figure 4.10 Perimeter ratio for an oblate and a prolate spheroid. (A) Smooth deformation of a sphere (top) to a prolate spheroid (bottom, left) or to an oblate spheroid (bottom, right) with the same volume as the sphere. Note that for a prolate $a = b < c$ while for an oblate $a = b > c$. (B) The perimeter ratio, $L_{\text{long}}/L_{\text{short}}$, as a function of the length of the semi-major axis for an oblate (red curve) and a prolate spheroid (blue curve) with the same volume as a sphere of radius $R = 18.25 \mu\text{m}$.

There is a difference between prolate and oblate geometries insofar as the ratio of the interface length for long- and short-axis polarisation, $L_{\text{long}}/L_{\text{short}}$ (short: perimeter ratio), differs; for an illustration see **Fig. 4.10**.

We compare the perimeter ratio $L_{\text{long}}/L_{\text{short}}$ for three-dimensional ellipsoids of the same volume. As our reference system we use a prolate spheroid with axes $15\ \mu\text{m} - 15\ \mu\text{m} - 27\ \mu\text{m}$, i.e. $a = b = 15\ \mu\text{m}$ (semi-minor axis) and $c = 27\ \mu\text{m}$ (semi-major axis). This is the same geometry that has been used to generate the results shown in the main text. The volume of an ellipsoid is $V_{\text{ellipsoid}} = \frac{4\pi}{3}a^2c$, corresponding to a sphere of same volume with radius $R = (a^2c)^{1/3} = 18.25\ \mu\text{m}$. Note that in contrast to a prolate spheroid, for an oblate spheroid a and c correspond to the semi-major and semi-minor axis, respectively; for an illustration see **Fig. 4.10 (A)**.

Fig. 4.10 (B) shows the perimeter ratio for prolate (blue) and oblate (red) spheroids as a function of the semi-major axis (c for prolate and a for oblate). Due to spherical symmetry, the perimeter ratio between long- and short-axis polarisation is equal to 1 for a sphere. For small deviations from spherical geometry (semi-major axis comparable with the radius of the sphere $R = 18.25\ \mu\text{m}$), the perimeter ratios in the prolate and oblate geometries are nearly the same. For larger deviations, however, the perimeter ratio for a prolate geometry becomes significantly smaller than for an oblate geometry. This difference suggests that long-axis polarisation is more favourable for a prolate spheroid than for an oblate spheroid.

Axis selection for an oblate spheroid As a representative example we analyzed pattern formation in an oblate spheroid with axes $35\ \mu\text{m} - 35\ \mu\text{m} - 13.2\ \mu\text{m}$ and the same volume as a sphere with radius $R = 18.25\ \mu\text{m}$ corresponding to a perimeter ratio of 0.72; note the smaller perimeter ratio 0.52 for a prolate spheroid with the same volume and semi-major axis $35\ \mu\text{m}$. We performed an extensive set of FEM simulations sweeping both λ and D_{cyt} in a range between $0.01\ \text{s}^{-1} - 0.3\ \text{s}^{-1}$ (with step size $0.01\ \text{s}^{-1}$) and $1.0\ \mu\text{m}^2\text{s}^{-1} - 20\ \mu\text{m}^2\text{s}^{-1}$ (with step size $1\ \mu\text{m}^2\text{s}^{-1}$), respectively, and determined the steady state solution of the reaction-diffusion model. **Fig. 4.11 (A)** shows a “phase diagram” indicating the parameter regimes where the polarisation axis is oriented along the long or short axis or along some intermediate axis (diagonal). We find that there is indeed a parameter regime where short-axis polarisation is stable, namely for D_{cyt} smaller than approximately $5\ \mu\text{m}^2\text{s}^{-1}$ and independent of the value of λ . This suggests that weak cytosolic flows are required for stable short-axis polarisation. Interestingly, there is no direct transition between stable short-axis and stable long-axis polarisation but an intermediary regime where the stable polarisation axis is aligned at an intermediate orientation. This indicates a subtle interplay between interface length minimisation and effects due to bulk-to-boundary ratios in this region of the $\lambda - D_{\text{cyt}}$ parameter space.

Axis selection for a prolate spheroid We have just learned that for a large perimeter ratio in an oblate spheroid one can find parameter regimes where short-axis polarisation is stable. However, for the prolate spheroid with the same volume (axes $15\ \mu\text{m} - 15\ \mu\text{m} -$

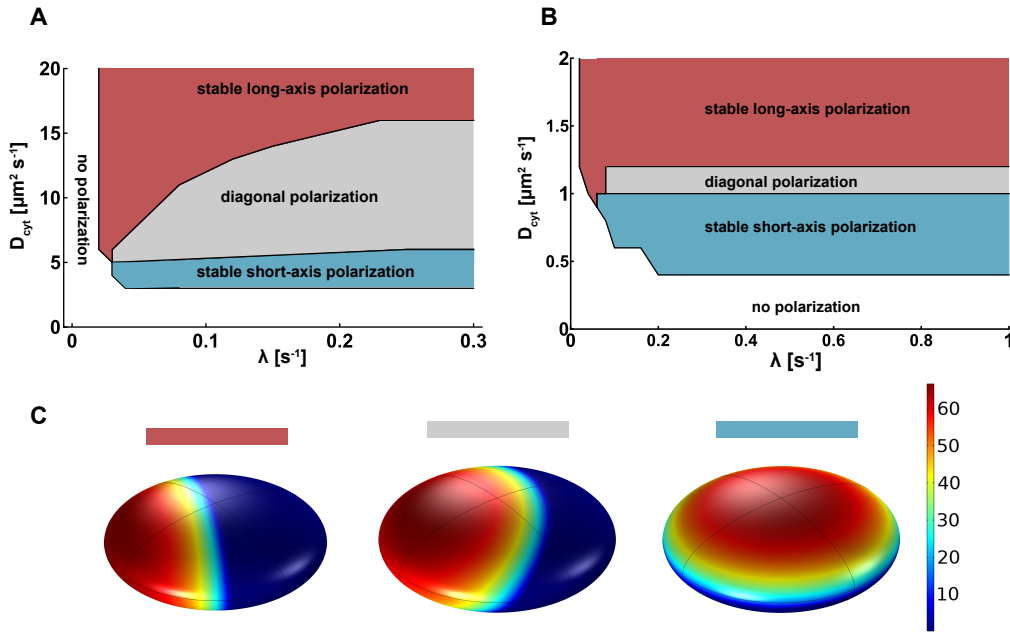


Figure 4.11 Axis selection for oblate and prolate spheroids. Stable polarisation axis in steady state as obtained from FEM simulations for an oblate (A) and a prolate spheroid (B) in the $\lambda - D_{\text{cyt}}$ parameter space. For an oblate spheroid (A), we find that short-axis polarisation is stable for small values of D_{cyt} (shaded cyan region) quite independent of the value for λ , while long-axis polarisation is stable for sufficiently large D_{cyt} and small λ (shaded red region), similar to our findings for two-dimensional ellipses (Fig. 4.3 in the main text). The transition from stable short-axis polarisation to long-axis polarisation is not abrupt but there is an intermediary region where the pattern aligns along the diagonal (shaded grey region). For a prolate spheroid (B), we find similar results but for different parameter regimes. Long-axis polarisation is stable for sufficiently large D_{cyt} (shaded red region), and the regime with diagonal polarisation is less pronounced. (C) Typical steady state patterns as obtained from the corresponding parameter combinations in (A) and (B) (red, grey, and cyan shaded area) shown for an oblate spheroid.

$27\mu\text{m}$) we only find metastable short-axis polarisation (see section *three-dimensional cell geometry and the role of interface length* and Fig. 4.6 in the main text). We hypothesize that this is due to the smaller perimeter ratio if compared to an oblate with the same volume (see Supplementary Fig. 4.10).

It is, however, not clear whether short-axis polarisation is always metastable in any prolate spheroids. If the perimeter ratio is indeed an important factor, it should be possible to find stable short-axis polarisation for a prolate spheroid that has a perimeter ratio comparable with an oblate spheroid (as is the case for prolate spheroids that are almost spherical, cf. Supplementary Fig. 4.10 (B)). To test this, we performed an extensive set of FEM simulations for a prolate spheroid with axes $16.6\mu\text{m} - 16.6\mu\text{m} - 22\mu\text{m}$, corresponding to a perimeter ratio of 0.86; note that an oblate with the same volume and semi-major axis $22\mu\text{m}$ gives a perimeter ratio of 0.88.

We used parameter for λ and D_{cyt} ranging between $0.01s^{-1} - 1.0s^{-1}$ (with step size $0.01s^{-1}$) and $0.4\mu m^2s^{-1} - 3\mu m^2s^{-1}$ (with step size $0.2\mu m^2s^{-1}$). Similar to the oblate case we indeed find that short-axis polarisation can be stabilized for a small parameter region in the $\lambda - D_{\text{cyt}}$ space and that the two regions (stable long- and short-axis polarisation) are connected by a regime where the pattern aligns along the diagonal (Supplementary **Fig. 4.11 (B)**). The parameter range for such an intermediate polarisation is, however, significantly smaller as for the oblate case.

4.7.6 Minimisation of the average net cytosolic protein flux onto the membrane explains interface minimisation

To shed more light on the observed interface minimisation in three-dimensional ellipsoidal geometries we analysed the net cytosolic protein fluxes onto the membrane for the different pPAR and aPAR protein species:

$$J_{\text{net}}^{(P)} = D_{\text{cyt}} \nabla_{\perp} c_P + D_{\text{cyt}} \nabla_{\perp} c_{P^*} = k_p^{\text{off}} m_P - k_p^{\text{on}} c_P + k_{Pa} m_P m_{A_{12}}, \quad (4.29)$$

$$\begin{aligned} J_{\text{net}}^{(A_1)} &= D_{\text{cyt}} \nabla_{\perp} c_{A_1} + D_{\text{cyt}} \nabla_{\perp} c_{A_1^*} \\ &= k_a^{\text{off}} (m_{A_1} + m_{A_{12}}) - k_a^{\text{on}} c_{A_1} + k_{Ap} m_P (m_{A_1} + m_{A_{12}}), \end{aligned} \quad (4.30)$$

$$J_{\text{net}}^{(A_2)} = D_{\text{cyt}} \nabla_{\perp} c_{A_2} = (k_{Ap} m_P + k_a^{\text{off}}) m_{A_{12}} - k_d c_{A_2} m_{A_1}, \quad (4.31)$$

see also in the Methods Section the paragraph on reactive boundary conditions.

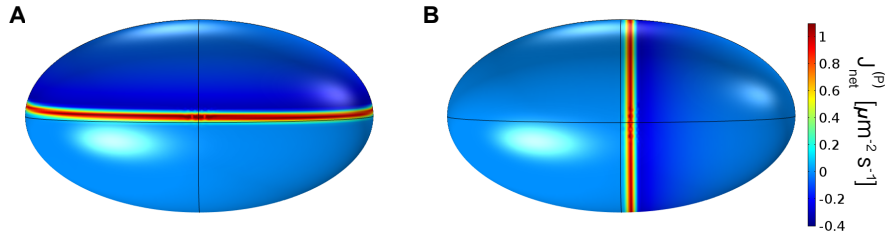


Figure 4.12 Illustration of protein fluxes onto the membrane. **(A)** A snapshot of the net flux $J_{\text{net}}^{(P)}$ of pPAR proteins where the system is polarised in a metastable state (short-axis polarisation) is shown. **(B)** A snapshot of the net flux $J_{\text{net}}^{(P)}$ of pPAR proteins where the system is polarised in a long-axis polarised is shown. The net flux of pPAR proteins along the interface has the same local magnitude for the steady state with long-axis polarisation as for the metastable short-axis polarisation. All parameters are set as in Table 4.10.

Strikingly, we find that all of the local net protein fluxes $J_{\text{net}}^{(P/A_{1,2})}$ remain constant as the pattern rotates from short- to long-axis polarisation; as an example the pPAR flux is shown in Supplementary **Fig. 4.12**. Hence, one expects that the averages of the absolute values of the net membrane fluxes integrated over the whole membrane area $\partial\Omega$

$$\bar{J}^{(P/A_{1,2})} = \int_{\partial\Omega} |J_{\text{net}}^{(P/A_{1,2})}| dS / \int_{\partial\Omega} dS \quad (4.32)$$

are expected to be larger for short-axis polarisation than for long-axis polarisation, simply due to the larger interface perimeter. This is indeed the case: for the pPAR flux shown in Supplementary **Fig. 4.12**, we find that the average absolute net flux ratio between long- and short-axis polarisation is $\bar{J}_{\text{long}}^{(P)}/\bar{J}_{\text{short}}^{(P)} = 0.66$. This indicates that long-axis polarisation is maintained by a smaller total protein flux and is therefore more favourable.

4.7.7 Cytosolic fluxes depend on the cytosolic diffusion and dictate the transition time from short to long axis polarisation

As discussed in the main text and shown there in **Fig. 4.14**, the transition time from short- to long-axis polarisation (for a 3d prolate spheroid) depends on both the reactivation rate λ and the cytosolic diffusion D_{cyt} . However, this dependence is not simply explained by the reactivation length ℓ alone, since our results show that actually the dependence on the cytosolic diffusion constant D_{cyt} is decisively stronger than that on λ . Because the transition from short- to long-axis polarisation (interface minimisation) is driven by protein fluxes, we investigated the cytosolic protein flux for different cytosolic diffusion constants D_{cyt} .

Fig. 4.13 (A) shows the magnitude of the cytosolic flux of species A_1 after the steady state (long-axis polarisation) has been reached. We defined the magnitude of the cytosolic flux as its Euclidean norm:

$$\|\vec{J}_{A_1}\| = D_{\text{cyt}} \|(\partial_x c_{A_1}, \partial_y c_{A_1}, \partial_z c_{A_1})\|. \quad (4.33)$$

This flux decreases with increasing distance from the membrane. Moreover, the lower the cytosolic diffusion the steeper are the flux gradients, i.e. the shorter is the penetration depth of the flux from the membrane into the cytosol; the width of the red domains (at midcell) in Supplementary **Fig. 4.13 (A)** decreases with lowering the diffusion constant from $D_{\text{cyt}} = 25 \mu\text{m}^2\text{s}^{-1}$ to $5 \mu\text{m}^2\text{s}^{-1}$. We also notice that the polar cytosolic region shows high cytosolic fluxes on the pPAR-side of the cell, i.e. where the P domain is on the membrane. In contrast, the cytosolic flux of A_1 is very low (blue in Supplementary **Fig. 4.13 (A)**) in the polar region where A_1 builds the domain on the membrane. **Fig. 4.13 (B)** shows the magnitude of the cytosolic flux of species A_1 integrated over the whole cytosol (total flux)

$$\|\vec{J}_{A_1}\|_{\text{tot}} = D_{\text{cyt}} \int_{\Omega} \|(\partial_x c_{A_1}, \partial_y c_{A_1}, \partial_z c_{A_1})\| \quad (4.34)$$

as a function of the cytosolic diffusion constant. Clearly, with increasing cytosolic diffusion constant, the overall cytosolic flux is increasing. Together with the observation that the transition times become shorter with increasing cytosolic diffusion constant (see **Fig. 4.6 (D)** in the main text) this shows that there is a correlation between

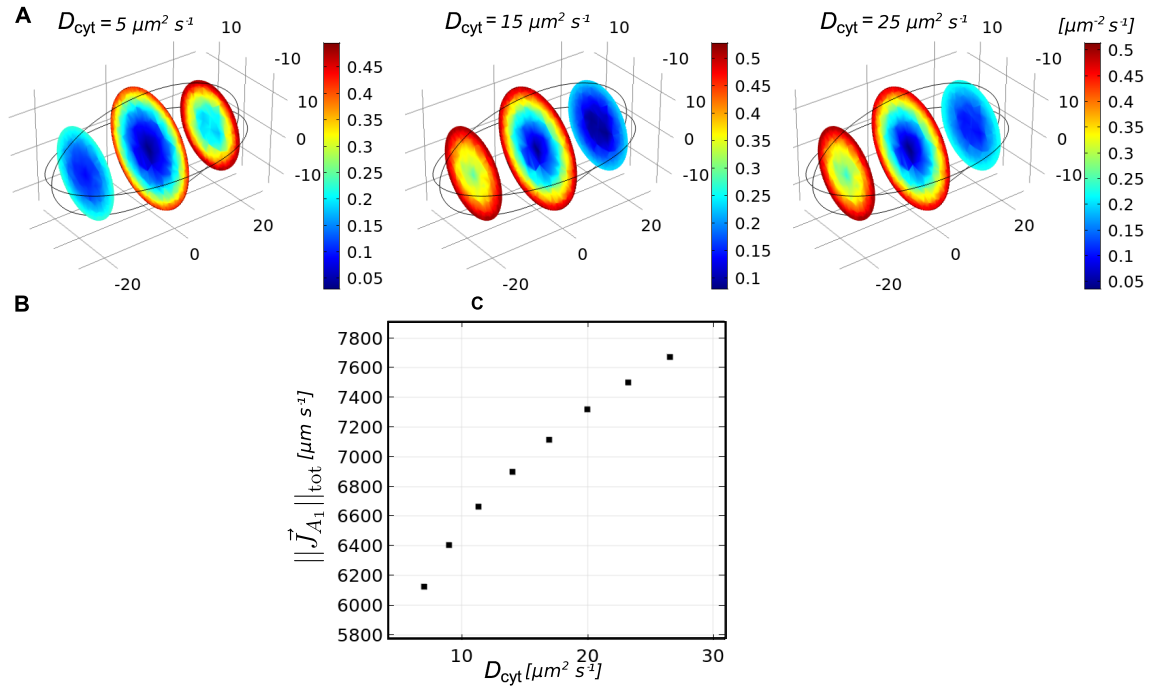


Figure 4.13 Illustration of cytosolic fluxes. (A) The magnitudes of cytosolic fluxes of species A_1 for three different cytosolic diffusion constants (indicated in the graph) are shown for three slices through the cytosol at $x = 0 \mu\text{m}$ and $x = \pm 18 \mu\text{m}$. The reactivation rate was set to $\lambda = 0.15 \text{s}^{-1}$ and all other parameters were set as given in the main text table 4. (B) The overall cytosolic flux (absolute value of flux integrated over the full cytosolic volume) is shown as a function of the cytosolic diffusion constant.

faster transition times and higher cytosolic fluxes.

4.7.8 Time scales for the formation of cell polarisation

In order to determine the time required for the formation of long-axis polarisation, we consider an idealised situation where this is achieved by the PAR reaction-diffusion system alone. For the cell polarisation process in *C. elegans* there is experimental evidence that the localisation of the centrosome as well as the successive actomyosin contraction play an important role in polarity establishment and support its alignment with the long axis ([94, 100, 103]). However, how the PAR reaction-diffusion system acts in concert with actomyosin contraction is not understood in realistic three-dimensional cell geometry. Previous work uses a simplified one-dimensional cell geometry ([31, 83, 100]). Here, we focus (as a first and important step) on the reaction-diffusion pathway alone disregarding any effects due to the PAR interaction with the centrosome or actomyosin contraction and ensuing cytoplasmic flows. This way one can learn how robust and fast reaction-diffusion dynamics on its own can establish long-axis polarisation and what the relative role of other effects like cytoplasmic flow may be.

In the actual *C. elegans* embryo polarisation has to be stable along the long axis for ≈ 15 min until the first cell division. Therefore, the time of a possibly existing short-axis polarisation and the transition to the long axis is an important observable for the real system. Hence we ask: How fast is the long axis selected as the stable polarisation axis driven solely by a reaction-diffusion dynamics?

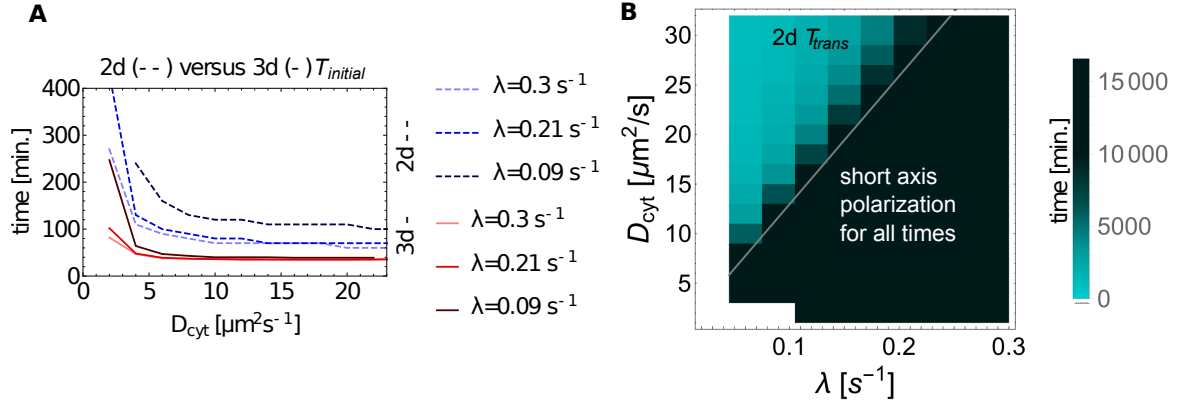


Figure 4.14 Times in 2d versus 3d. (A) The initial time of polarisation T_{initial} is plotted against the cytosolic diffusion for various reactivation rates in 2d as well as in 3d. (B) T_{trans} is shown in cyan color code in the $D_{\text{cyt}}-\lambda$ parameter space. The gray line shows the line of constant reactivation length, which divides steady state long- and short-axis polarisation ℓ^* . It was interpolated as a linear function with zero offset.

We find that the time scales for the selection and maintenance of different polarisation axes depend on the reactivation rate λ and the cytosolic diffusion D_{cyt} both in a two-dimensional elliptical geometry and in an three-dimensional ellipsoidal geometry (see **Fig. 4.6** and **Fig. 4.14**). Strikingly, the transition time from short to long axis polarisation is extremely slow in 2d compared to 3d (≈ 1000 min in 2d compared to ≈ 100 min for 3d data: compare Supplementary **Fig. 4.14** with **Fig. 4.6** in the main text). The transition time from any transient polarisation pattern to a steady state long-axis polarisation pattern may be taken as a proxy for the expected typical time scales of polarisation re-alignment in case of an initially non-aligned cue (e.g. this happens if the centrosome does not localise at the poles initially). Hence, we conclude that for physiological parameters in 2d these times are far too long: a wrong alignment induced by cues or flows can not be corrected by a mechanism based on reaction and diffusion alone. In contrast, our simulations in 3d show that these transition times are short in a broad region of parameter space; compare **Fig. 4.14** with **Fig. 4.6** in the main sections. Therefore, we conclude, that all geometry-sensitive mechanisms of the reaction-diffusion system, as well as the activation-deactivation cycle and interface minimisation, play an important role for cell polarisation in *C. elegans*. Antagonism (of aPARs and pPARs) and recruitment (among aPARs) enables polarisation, fast cytosolic diffusion and the activation-deactivation cycle enable the cell to polarise along the long axis from the beginning on, and interface minimisation always leads to long axis polarisation in the long term. Furthermore, cytosolic diffusion, as it determines

the magnitude of fluxes, decisively influences perfect polarity establishment along the long axis on a biologically reasonable time scale. E.g. if the centrosome was originally localised close to mid-cell and would induce an initial polarity alignment with the long axis, fast cytosolic diffusion would rescue such an embryo and polarisation would align with the long axis before cell division.

In contrast to the transition time from any initial polarisation to well aligned long-axis polarisation, the establishment time of the initial polarisation from a homogenous aPAR dominated state on the membrane is strongly dependent on the type of initial perturbations. Take **Fig. 4.7** middle and bottom row as an example in 2d, where polarisation is quickly established with initial gradients (despite of misalignment). The establishment time of any polarisation from a homogenous aPAR dominated state with only a small random initial perturbation is of the order of 30 minutes in 3d and is approximately three times slower in 2d. Therefore, with only a small random initial perturbation the reaction-diffusion system alone does still lead to stable polarisation, but on a time scale that is too slow for the real embryo (see **Fig. 4.14 (A)** for 2d and 3d times).

4.8 Supplementary Tables

| k_{Ap} | k_{Pa} | steady state | onset |
|----------|----------|------------------------|--------------------------|
| 0.24 | 2.28 | no pattern | transient long axis pol. |
| 0.28 | 2.16 | long axis polarisation | long axis |
| 0.32 | 2.04 | long axis polarisation | long axis |
| 0.36 | 1.92 | long axis polarisation | long axis |
| 0.4 | 1.8 | long axis polarisation | long axis |
| 0.44 | 1.1.68 | long axis polarisation | long axis |
| 0.48 | 1.56 | long axis polarisation | long axis |
| 0.5 | 1.5 | long axis polarisation | long axis |
| 0.52 | 1.44 | long axis polarisation | long axis |
| 0.54 | 1.38 | long axis polarisation | long axis |
| 0.56 | 1.32 | long axis polarisation | long axis |
| 0.58 | 1.26 | long axis polarisation | long axis |
| 0.6 | 1.2 | long axis polarisation | long axis |
| 0.64 | 1.08 | long axis polarisation | long axis |
| 0.68 | 0.96 | long axis polarisation | long axis |
| 0.72 | 0.84 | no pattern | transient long axis pol. |
| 0.76 | 0.72 | no pattern | transient long axis pol. |

Table 4.5 Sweep of antagonistic rates to investigate the excitable region with initial gradients for slow reactivation. FEM sample sweeps of k_{Ap} , k_{Pa} with initial linear gradient for $\lambda = 0.05s^{-1}$ (for more details see Supplementary Section 4.7.1). The sweep shows that also outside of the spontaneously polarising region the system can be excited into stable long axis polarisation. All other parameters were set as in the standard parameter set shown in Table 4.1 of the main text.

| k_{Ap} | k_{Pa} | steady state | onset |
|----------|----------|-------------------------|-------------------------|
| 0.2 | 2.4 | no pattern | transient short axis p. |
| 0.24 | 2.28 | short axis polarisation | short axis |
| 0.28 | 2.16 | short axis polarisation | short axis |
| 0.32 | 2.04 | short axis polarisation | short axis |
| 0.36 | 1.92 | short axis polarisation | short axis |
| 0.4 | 1.8 | short axis polarisation | short axis |
| 0.44 | 1.1.68 | short axis polarisation | short axis |
| 0.48 | 1.56 | short axis polarisation | short axis |
| 0.5 | 1.5 | short axis polarisation | short axis |
| 0.52 | 1.44 | short axis polarisation | short axis |
| 0.54 | 1.38 | short axis polarisation | short axis |
| 0.56 | 1.32 | short axis polarisation | short axis |
| 0.58 | 1.26 | short axis polarisation | short axis |
| 0.6 | 1.2 | short axis polarisation | short axis |
| 0.64 | 1.08 | short axis polarisation | short axis |
| 0.68 | 0.96 | short axis polarisation | short axis |
| 0.72 | 0.84 | no pattern | transient short axis p. |
| 0.76 | 0.72 | no pattern | transient short axis p. |

Table 4.6 Sweep of antagonistic rates to investigate the excitable region with initial gradients for fast reactivation. FEM sample sweeps of k_{Ap} , k_{Pa} with initial linear gradient for $\lambda = 0.3s^{-1}$ (for more details see Supplementary Section 4.7.1). The sweep shows that also outside of the spontaneously polarising region the system can be excited into stable short axis polarisation. All other parameters were set as in the standard parameter set shown in Table 4.1 of the main text.

| k_{Ap} | k_{Pa} | steady state | onset |
|----------|----------|-------------------------|-------------------------|
| 0.2 | 2.4 | no pattern | transient short axis p. |
| 0.24 | 2.28 | short axis polarisation | short axis |
| 0.28 | 2.16 | short axis polarisation | short axis |
| 0.32 | 2.04 | short axis polarisation | short axis |
| 0.36 | 1.92 | short axis polarisation | short axis |
| 0.4 | 1.8 | short axis polarisation | short axis |
| 0.44 | 1.1.68 | short axis polarisation | short axis |
| 0.48 | 1.56 | short axis polarisation | short axis |
| 0.5 | 1.5 | short axis polarisation | short axis |
| 0.52 | 1.44 | short axis polarisation | short axis |
| 0.54 | 1.38 | short axis polarisation | short axis |
| 0.56 | 1.32 | short axis polarisation | short axis |
| 0.58 | 1.26 | short axis polarisation | short axis |
| 0.6 | 1.2 | short axis polarisation | short axis |
| 0.64 | 1.08 | short axis polarisation | short axis |
| 0.68 | 0.96 | short axis polarisation | short axis |
| 0.72 | 0.84 | no pattern | transient short axis p. |
| 0.76 | 0.72 | no pattern | transient short axis p. |

Table 4.7 Sweep of antagonistic rates to investigate the excitable region with initial gradients for fast reactivation. FEM sample sweeps of k_{Ap} , k_{Pa} with initial linear gradient for $\lambda = 1.s^{-1}$ (for more details see Supplementary Section 4.7.1). The sweep shows that also outside of the spontaneously polarising region the system can be excited into stable short axis polarisation. All other parameters were set as in the standard parameter set shown in Table 4.1 of the main text.

| Parameter | Value |
|-----------------|-----------------------------|
| a | $13.2 \mu m$ |
| b | $13.2 \mu m$ |
| c | $35 \mu m$ |
| $k_{a/p}^{on}$ | $0.1 \mu m \cdot s^{-1}$ |
| $k_{a/p}^{off}$ | $0.005 s^{-1}$ |
| k_{Ap} | $0.4 \mu m^2 \cdot s^{-1}$ |
| k_{Pa} | $1.2 \mu m^2 \cdot s^{-1}$ |
| k_d | $0.15 \mu m^3 \cdot s^{-1}$ |
| D_{mem}^a | $0.28 \mu m^2 \cdot s^{-1}$ |
| D_{mem}^p | $0.15 \mu m^2 \cdot s^{-1}$ |
| ρ_{A1} | $10.5 \mu m^{-3}$ |
| ρ_{A2} | $2.5 \mu m^{-3}$ |
| ρ_P | $12.0 \mu m^{-3}$ |

Table 4.8 Parameter set for the oblate 3d FEM sweep in Fig. 4.11. All parameters were fixed to the values shown above except for D_{cyt} and λ . The cytosolic diffusion constant D_{cyt} was varied between $1.0 \mu m^2 \cdot s^{-1} - 20 \mu m^2 \cdot s^{-1}$ (with step size of $1 \mu m^2 \cdot s^{-1}$) and the reactivation rate λ was varied between $0.01 s^{-1} - 0.3 s^{-1}$ (with step size of $0.01 s^{-1}$) to generate the result shown in **Fig. 4.11**.

| Parameter | Value |
|-----------------|-----------------------------|
| a | $22 \mu m$ |
| b | $22 \mu m$ |
| c | $16.6 \mu m$ |
| $k_{a/p}^{on}$ | $0.1 \mu m \cdot s^{-1}$ |
| $k_{a/p}^{off}$ | $0.005 s^{-1}$ |
| k_{Ap} | $0.4 \mu m^2 \cdot s^{-1}$ |
| k_{Pa} | $1.2 \mu m^2 \cdot s^{-1}$ |
| k_d | $0.15 \mu m^3 \cdot s^{-1}$ |
| D_{mem}^a | $0.28 \mu m^2 \cdot s^{-1}$ |
| D_{mem}^p | $0.15 \mu m^2 \cdot s^{-1}$ |
| ρ_{A1} | $10.5 \mu m^{-3}$ |
| ρ_{A2} | $2.5 \mu m^{-3}$ |
| ρ_P | $18.0 \mu m^{-3}$ |

Table 4.9 Parameter set for the prolate 3d FEM sweep in Fig. 4.11. All parameters were fixed to the values shown above except for D_{cyt} and λ . The cytosolic diffusion constant D_{cyt} was varied between $0.4 \mu m^2 \cdot s^{-1} - 3.0 \mu m^2 \cdot s^{-1}$ (with step size of $0.2 \mu m^2 \cdot s^{-1}$) and the reactivation rate λ was varied between $0.01 s^{-1} - 1.0 s^{-1}$ (with step size of $0.01 s^{-1}$) to generate the result shown in **Fig. 4.11**.

| Parameter | Value |
|------------------------|------------------------------|
| a | $27 \mu m$ |
| b | $15 \mu m$ |
| c | $15 \mu m$ |
| D_{cyt} | $10 \mu m^2 s^{-1}$ |
| λ | $0.2 s^{-1}$ |
| $k_{a/p}^{\text{on}}$ | $0.1 \mu m \cdot s^{-1}$ |
| $k_{a/p}^{\text{off}}$ | $0.005 s^{-1}$ |
| k_{Ap} | $0.4 \mu m^2 \cdot s^{-1}$ |
| k_{Pa} | $1.2 \mu m^2 \cdot s^{-1}$ |
| k_d | $0.034 \mu m^3 \cdot s^{-1}$ |
| D_{mem}^a | $0.28 \mu m^2 \cdot s^{-1}$ |
| D_{mem}^p | $0.15 \mu m^2 \cdot s^{-1}$ |
| ρ_{A1} | $10.5 \mu m^{-3}$ |
| ρ_{A2} | $2.5 \mu m^{-3}$ |
| ρ_P | $8.0 \mu m^{-3}$ |

Table 4.10 Parameter set for the pPAR average net membrane flux shown in Fig. 4.12.

Chapter 5

***In vivo* measurements of PAR membrane diffusion**

Given the right strains, material and advice the work in the lab with *C. elegans* is learnable within a few weeks. During a summer school in 2016 at the KITP in Santa Barbara, California, I got the chance to measure membrane diffusion constants in the *C. elegans* zygote by myself. My advisor and tutor were Natan Goehring and Lars Hubatsch, who brought all material and showed me how to dissect worms, pick single cell embryos and measure the motility of tagged proteins in them. In the following, the background and motivation, the experimental technique that I learned about, and the results from our measurements of the membrane diffusion constant of PAR-3 and PAR-6 are presented. The results are then compared with previous measurements and discussed.

5.1 Motivation and background

5.1.1 Theory and experiment

The aim of a theory and of theoretical models should be to make predictions which are testable. Even though my doctoral studies at the theory group LS Frey are mainly of theoretical nature, I found it very helpful to experience myself which experimental results can be obtained in real model organisms. This also changes perspectives when working on a theoretical model. Investigation of a reaction-diffusion system theoretically results in a set of open parameters, reaction rates and diffusion constants (as described mathematically in chapters 3 and 4). For a quantitative comparison of theory and experiment physical parameters, such as membrane un-/binding and diffusion rates, need to be measured. Furthermore, when the order of magnitude of at least some parameters is known, then computational parameter sweeps, performed to challenge a model, have a starting point.

5.1.2 Methods to measure PAR protein motilities

Kinetic parameters in *C. elegans* were measured in the past mainly with two experimental methods: (i) Fluorescence Recovery After Photobleaching (FRAP) [26] and (ii) single-molecule tracking techniques [102, 104–106].

The method FRAP to measure lateral diffusion can be summarised as follows: The object of interest, here the single cell *C. elegans* zygote, should contain fluorescently labeled proteins. A well defined region of a thin film on the embryo is photo-bleached. Then the time of fluorescence recovery is measured. From the results diffusion constants and, with some mathematical assumptions, also binding and detachment rates can be approximated [26].

Single molecule tracking on the other hand is based, as its name says, on measuring the track in space and time of single tagged proteins. Sampling many of these tracks then allows to statistically evaluate the proteins' motility.

At the KITP we we worked with single-molecule tracking to measure membrane diffusion constants following a Nature methods publication by Robin et al [102].

5.1.3 Motivation for experiments

Two main questions guided our measurements: As FRAP has widely been used to measure membrane diffusivities of PAR proteins, which values for membrane diffusion constants of PAR proteins does one obtain using single-molecule tracking? The second question arises, because PAR-3 is a protein which tends to cluster [107]. Therefore, the question arises, if this clustering is also observable via different diffusion constants, i.e. one of PAR-3 clusters and one of individual PAR-3 proteins?

5.2 Experimental procedure

In order to answer these questions we performed single-molecule tracking of PAR-3 and PAR-6 at the cell cortex. We used the light microscopy technique "highly inclined and laminated optical sheet" (HILO, see **Fig. 5.2**) to acquire image series. Image analysis let us calculate the mean-squared-displacement (MSD) from which, in turn, we obtained diffusion constants.

5.2.1 Preparation of embryos

C. elegans worms were fed with tagged PAR proteins (transgenics, feeding RNA interference called fRNAi) [108]. In their embryos the fed, tagged PAR proteins are accepted as the ones they self-express in the wild type. We prepared embryos in their single cell state. Therefore, we dissected pregnant worms and picked single cell zygotes. These zygotes were then isolated between two coverslips in a liquid filled with small beads such that they would not be pressed from the coverslips. The prepared embryos were then investigated under the microscope. Here, embryos were investigated until the completion of the first round of cytokinesis, in order to check if they were healthy. Dying embryos might deliver different data. A sample image series of GFP-tagged PAR-6 is shown in **Fig. 5.1**.

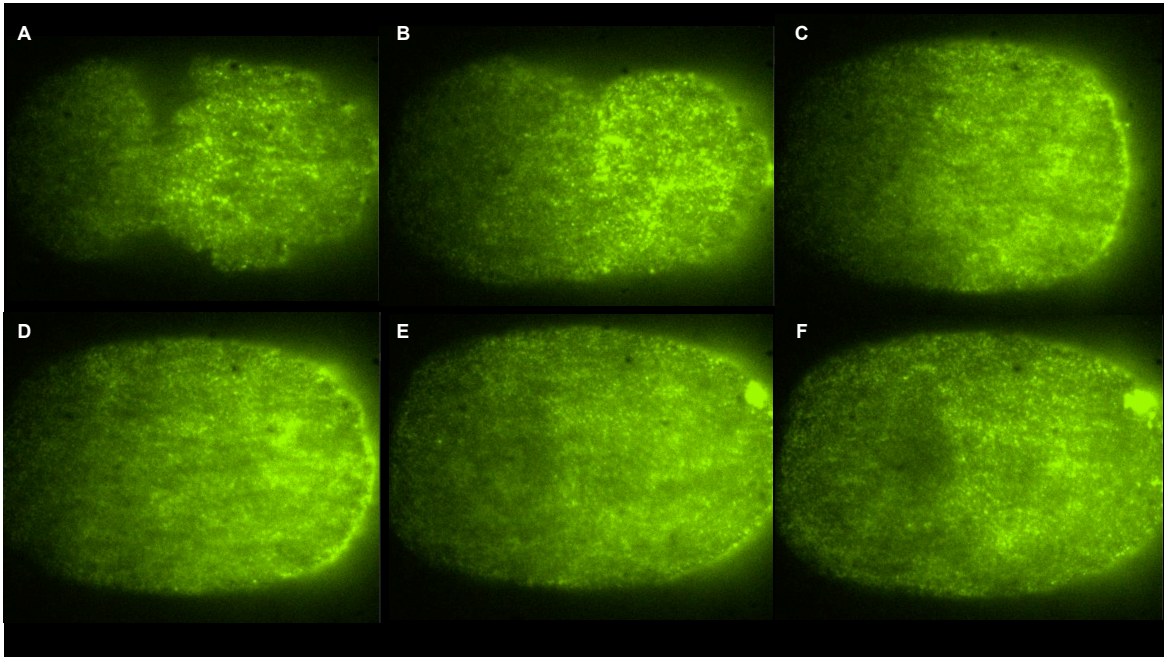


Figure 5.1 Image series of *C. elegans* zygote with GFP-tagged PAR-6. In images (A) to (C) the cortex deforms which is typical for the phase of polarity establishment. In images (D) to (F) polarity is maintained and the zygote does not deform significantly anymore. The centrosome can now be seen on the right.

5.2.2 Imaging using HILO

Image series at the cell cortex were shot using the technique HILO. In **Fig. 5.2 (C)** HILO is illustrated compared to epi-fluorescence, also called widefield, microscopy shown in **Fig. 5.2 (A)**, and "total internal reflection fluorescence" (TIRF) shown in **Fig. 5.2 (B)**. Epi-fluorescence would create images from the whole embryo, not only the cortex, whereas TIRF would create images from a very thin ($\approx 100\text{ nm}$ thick) layer on the embryos surface. HILO, also called "leaky TIRF", makes it possible to create images from a thicker layer of the embryo without imaging it fully. This is useful to image the cell cortex and not the cytosol. Furthermore, it damages the embryo less than imaging in widefield mode.

Before imaging intervals were shot, an embryo was photo-bleached until only few GFP-tagged proteins were still visible under the microscope. A depletion interval was followed by an imaging interval. Most of the measurements were performed using 200 ms depletion intervals with 800 ms imaging intervals. Bleaching was always limited to less than 10 s in order to not risk the zygote's death. Image series were taken around the time of nuclear envelope breakdown for several minutes. We took images of PAR-3

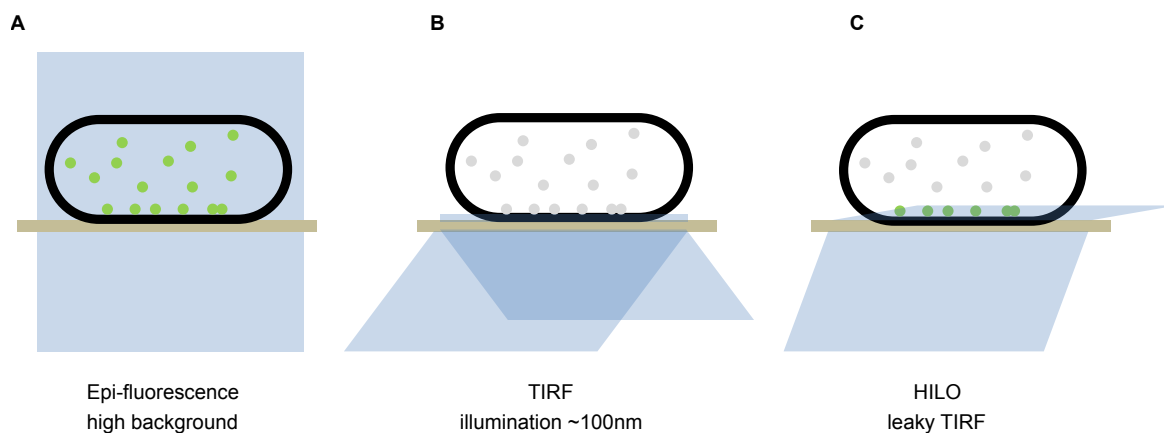


Figure 5.2 Schematics of different light microscopy techniques. (A) In epi-fluorescence also called widefield microscopy the probe is directly illuminated with light of a specific wavelength. (B) In TIRF (total internal reflection fluorescence) light passes onto the probe with an angle that is larger than a critical angle at which light would still be absorbed. An evanescent field is generated which excites fluorophores in an extremely thin layer at the coverslip. (C) With the technique HILO (highly inclined and laminated optical sheet) angles close to but not at total internal reflection are used. Thus light passes through a thicker layer of the probe which is just the right thickness to illuminate the cell cortex in *C. elegans*.

and PAR-6 proteins for several minutes and afterwards waited to check if the first cell cycle would complete. This ensured that we measured on a living zygote.

5.2.3 Single-molecule tracking to obtain mean-squared displacement.

Several image series interrupted by depletion intervals were taken. Afterwards images were analysed. One could distinguish single molecules and their trajectories in space (on each image) and time (one image after the other). This is illustrated in **Fig. 5.3**. From the trajectories the mean-squared displacement (MSD) of a tagged protein versus the lag time τ between two measurements of the protein was obtained. For the MSD the following relation holds:

$$\text{MSD}(\tau) = \langle r^2(\tau) \rangle = 4D\tau^\alpha \quad (5.1)$$

Measurement and calculation of the MSD (for illustration see **Fig. 5.3**) for different trajectories and lag times results in many data points for α and D , see **Fig. 5.5 (A,B)**.

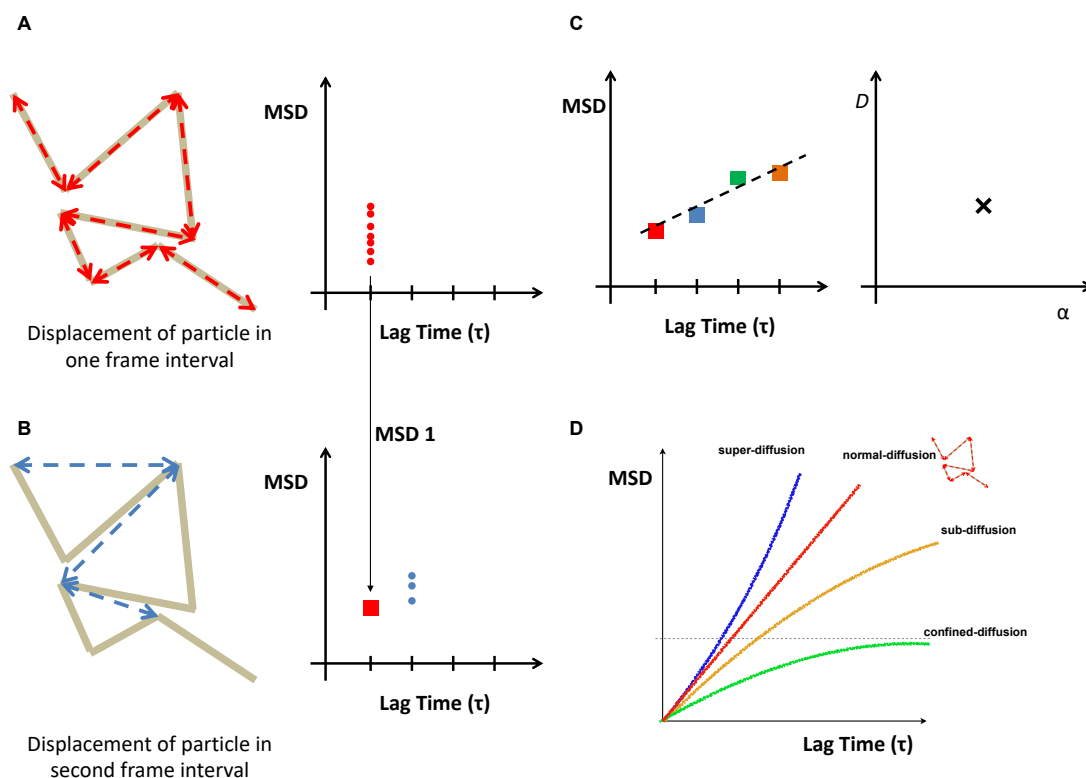


Figure 5.3 Use of single molecule tracking to find diffusive behaviour via the mean square displacement (MSD). The track of a single particle is shown in (A) and (B) on the left. For a fixed time interval the distance between each consecutive points is squared. Its average gives one point to contribute to the mean-square-displacement measurement (see non-averaged points in (A,B) on the right and the averaging illustrated with MSD1). Time intervals were chosen longer in (B) than in (A). (C) From several different lag times τ one obtains several values of the MSD. With the relation $\text{MSD}(\tau) = \langle r^2(\tau) \rangle = 4D\tau^\alpha$ one obtains a measurement in $D - \alpha$ space for each trajectory. As depicted in (D) normal diffusion corresponds to $\alpha = 1$. For larger α -values there is super- and for lower ones there is sub-diffusion and confinement.

5.2.4 Simulations to test against artefacts

For extremely low membrane diffusion constants ($< 0.05 \text{ m}^2 \text{ s}^{-1}$) we observed also low α -values ($\alpha < 1$) which corresponds to sub-diffusive behaviour. Since for such low diffusion constants the resolution (pixel size $0.1049 \mu\text{m}$) could play a role, we additionally performed Gillespie simulations [109–111] of continuous diffusion in a grid. The grid should mimic the grid of pixels of the images from the microscope's camera.

5.3 Results

Our results addressed several details on PAR-3 and PAR-6 diffusion on the cortex of single cell *C. elegans* zygotes. The results can be summarised as follows: We measured the MSD of GFP-tagged PAR-3 and PAR-6 before and after nuclear envelope breakdown (NEBD). Analysis of these measurements allowed conclusions on the values of respective cortex diffusion constants and α -values. Furthermore, with the help of Gillespie simulations for comparison we could estimate if sub-diffusive behaviour was present before NEBD. Last but not least, image analysis with different light sensitivities made PAR-3 cluster detection possible. We could measure PAR-3 cluster diffusion constants.

5.3.1 Diffusion constant measurements of PAR-3 and PAR-6

Evaluation of the MSD of GFP-tagged PAR-3 and PAR-6 showed lower diffusion constants before compared to after NEBD for both protein species (see **Fig. 5.4**). Furthermore, the two protein species have different diffusive behaviour.

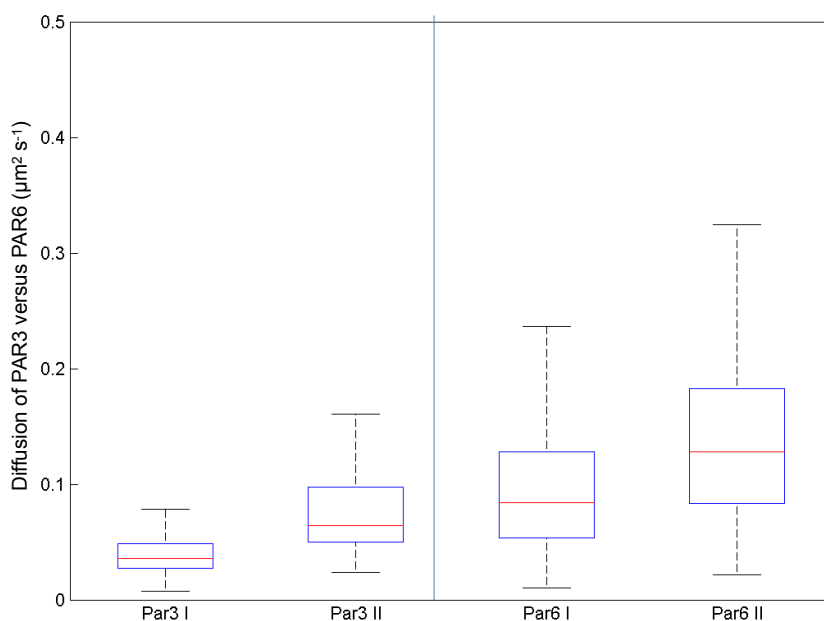


Figure 5.4 PAR-3 and PAR-6 diffusion constants approximately before (I) and after (II) nuclear envelope breakdown (NEBD). On each blue box, the central red mark indicates the median, and the bottom and top edges of the box indicate the 25th and 75th percentiles, respectively. The whiskers extend to the most extreme data points not considered outliers.

5.3.2 Seemingly abnormal diffusion and limitations by image resolution

While PAR-6 exhibited normal diffusive behaviour ($\alpha \approx 1$), we obtained PAR-3 α -values significantly below 1, especially before NEBD (see **Fig. 5.5, (A)**). However, PAR-3 showed the slowest diffusive behaviour of all our measurements before NEBD. We guessed that for very slow diffusion ($\mathcal{O}(10^{-2} \mu\text{m}^2\text{s}^{-1})$ or smaller) the lag times τ were too short to assure that a protein would be able to leave its pixel before the next image was taken. Lag times could not be chosen larger than on the order of seconds for two reasons: Long bleaching intervals damaged the embryos so strongly that they typically did not survive. Long lag times without long depletion made it impossible to assure to follow single particles. In order to check if the pixel size could lead artificially to low α -values I performed Gillespie simulations according to diffusion equations with diffusion constants (i) $D = 0.01 \mu\text{m}^2\text{s}^{-1}$ and (ii) $D = 0.3 \mu\text{m}^2\text{s}^{-1}$. The resulting trajectories were discretised with the same grid size as the pixels of the images from the microscope. We found that this technique leads to values $\alpha < 1$ for $D = 0.01 \mu\text{m}^2\text{s}^{-1}$, despite of the underlying pure diffusion equation for the Gillespie algorithm (see **Fig. 5.5, (B)**).

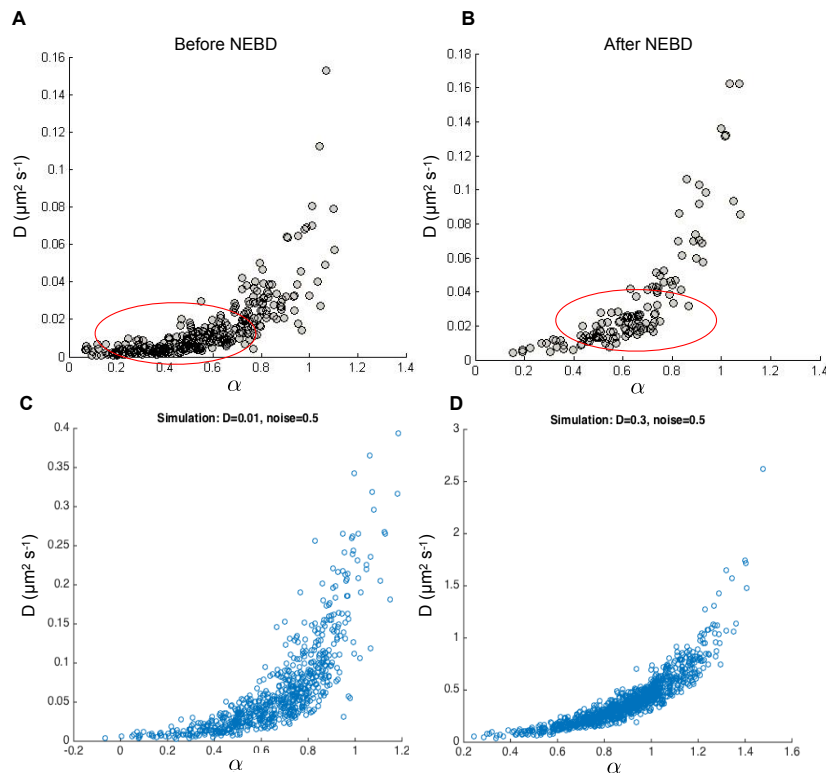


Figure 5.5 PAR-3 diff.

5.3.3 Selection for PAR-3 clusters by decreased light sensitivity

As PAR-3 proteins tend to cluster on the membrane, their clusters might have different diffusion constants than individual proteins and small complexes. Since clusters of GFP-tagged proteins emit more light than individual proteins, one can select for clusters during image processing by reducing the light sensitivity (see **Fig. 5.6 (A)**). This results in two different measured diffusion constants for PAR-3 proteins: an on average faster diffusion constant which include all PAR-3 proteins and a slow diffusion constant for clusters of PAR-3 (see **Fig. 5.6 (B,C)**). Measurements were approximately taken at NEBD. As expected, the variance of the diffusion constant of all objects ranging from single proteins to larger clusters is much higher than that of the clusters solely.

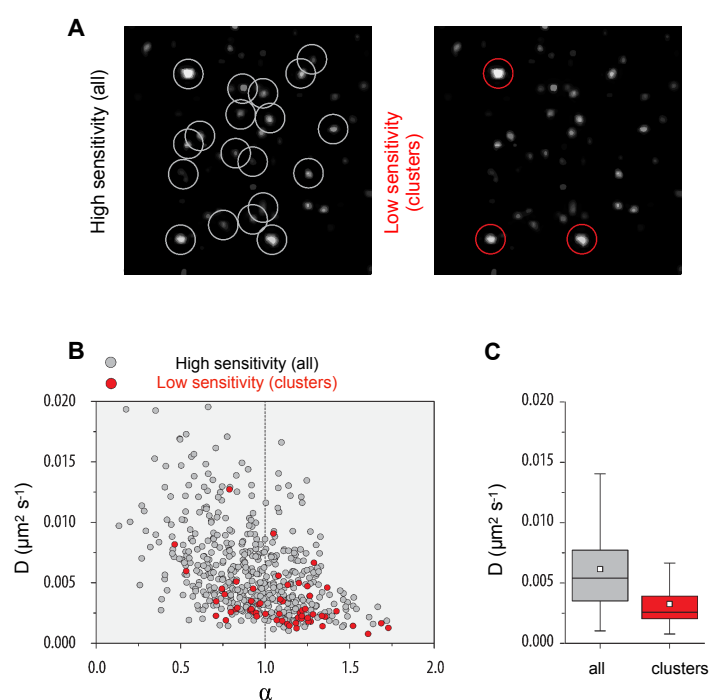


Figure 5.6 PAR-3 protein cluster selection. (A) Images were analysed with different light sensitivities. With a high sensitivity individual as well as clusters of PAR-3 proteins were tracked, while with a low sensitivity only clusters of proteins were tracked. (B,C) Tracking and evaluation of the MSD shows lower diffusion constants for clusters of proteins. (C) On each box, the central red mark indicates the median, where the single and hollow point marks the mean. The bottom and top edges of the box indicate the 25th and 75th percentiles, respectively. The whiskers extend to the most extreme data points not considered outliers.

5.4 Conclusion and discussion

The following main conclusions can be drawn from the results:

1. Anterior PAR Proteins (PAR-3 and PAR-6) exhibit different dynamics. PAR-3 diffusion constants ranged from $D = 0.041 \mu\text{m}^2\text{s}^{-1}$ (before NEBD) to $D = 0.075 \mu\text{m}^2\text{s}^{-1}$ (after NEBD). PAR-6 diffusion constants ranged from $D = 0.095 \mu\text{m}^2\text{s}^{-1}$ (before NEBD) to $D = 0.145 \mu\text{m}^2\text{s}^{-1}$ (after NEBD).
2. Diffusion constants appear to vary throughout the first cell cycle (before compared to after NEBD).
3. Extremely low diffusion constants are typically accompanied by low α -values, i.e. the dynamics seems sub-diffusive. To our understanding this is an artefact arising from image resolution.
4. PAR-3 proteins coexist in single as well as clustered states on the membrane. Clusters diffuse very slowly with $D \approx 0.05 \mu\text{m}^2\text{s}^{-1}$.

The value of PAR-6 diffusion has been measured in the past using FRAP [26] and single-molecule tracking [102] for PAR-2 and PAR-6. While the order of magnitude of the diffusion constant yielded similar results with both methods, the precise results differed. With FRAP PAR-6 diffusion was found at $D = 0.28 \mu\text{m}^2\text{s}^{-1}$ [26], while with single molecule tracking yielded $D = 0.17 \mu\text{m}^2\text{s}^{-1}$. Our estimates were lower, however, since diffusion constants differed before and after NEBD cell cycle dynamics such as flows and other motilities might affect diffusion measurements. Since we also found that very low diffusion can be misinterpreted as sub-diffusion, I concluded that only the order of magnitude of membrane diffusion is fully reliable. Differences between diffusion constants from FRAP and MSD of tracked proteins can also be found comparing previous reported results for PAR-2 diffusion. Goehring and Trong, et al [26] found a PAR-2 diffusion constant of $D = 0.15 \mu\text{m}^2\text{s}^{-1}$ while the PAR-2 diffusion constants obtained by Arata et al [106] using single-molecule tracking and evaluation with MSD were much lower with $D = 0.05 \mu\text{m}^2\text{s}^{-1}$.

Furthermore, as in our experiments PAR-6 diffusion was faster than PAR-3 diffusion one could conclude that GFP-tagged PAR-6 did mainly not bind to clustering PAR-3. Maybe PAR-3 binding sites are occupied when proteins oligomerise. It was reported that PAR-3 oligomerisation is prevented by Polo-like kinase 1 (PLK-1) phosphorylation, which links complex formation to the cell cycle [112]. PLK-1 reduces PAR-3 clustering mainly during maintenance phase.

Another option to explain higher PAR-6 than PAR-3 diffusion constants could state that CDC-42 plays a major role in scaffolding the PAR-6/PKC-3 complex and PAR-3 is less important in scaffolding than previously suggested [49, 61].

Therefore, it would be insightful if a future model included two scaffold proteins among aPARs, where one can oligomerise [113]. Compared to my model presented

in chapter 4, this would be much more detailed and therefore complicated. However, especially the scaffold clustering could have interesting effects.

Chapter 6

Conclusion, discussion and outlook

6.1 Conclusion and discussion

6.1.1 Summary and conclusion of the main results

An in depth study of the PAR protein system in different geometries was performed. For this concrete model system two main questions guided my work: How can the PAR reaction-diffusion system in an ellipsoidal cell form and maintain a polarised pattern in a self-organised manner? How is polarisation aligned with the long axis of the cell? Furthermore, this work should shed light on reaction-diffusion systems in different geometries in general. Hereby, aiming to answer which patterns can form in a self-organised manner and how do patterns align within a specific geometry?

I have developed a model for the PAR system in *C. elegans*. With a step-by-step mathematical and computational procedure, where the model was analysed in rectangular, elliptical and ellipsoidal geometries, I could, supported by my colleagues *Laeschkir Würthner* and *Jacob Halatek*, and my supervisor *Erwin Frey*, disentangle the different mechanisms for polarisation by the PAR system in *C. elegans* and its alignment with a cellular axis.

Concretely, we were able to find the following essentials for polarisation and its alignment in the *C. elegans* zygote: As suggested by previous authors [31, 83, 84], we verified that a general polarisation is mainly promoted by mutual antagonism. Since we only allowed biochemically motivated bimolecular reactions in the model, we could conclude that another feedback loop additional to mutual antagonism (recruitment in our model) is necessary. This could not be investigated with previous models using effective non-linear terms. Solely bimolecular, mutual detachment between two species is not sufficient for stable polarisation. Furthermore, we could show that a balance of antagonistic processes is key to a self-organised and stable polarisation from initially uniform concentrations. This includes a balance of the antagonistic detachment rates and a balance of the antagonistic protein numbers.

For the polarisation orientation in ellipsoidal geometry in *C. elegans*, we identified both geometric and kinetic cues: First of all, the cellular geometry is sensed by diffusing proteins in the cytosol. When proteins are detached from the membrane locally at some point, the likelihood of reencountering the membrane close to the detachment point is dictated by the membrane-to-bulk ratio. As protein patterning on the membrane is mediated by proteins encountering the membrane this ratio is the mediator between pattern formation induced by the membrane-kinetics and geometry.

Due to the specific membrane-to-bulk ratio in two-dimensional elliptical geometry a phosphorylation-dephosphorylation (inactivation-reactivation for membrane binding) cycle is required for stable long-axis polarisation. Without accounting for a cytosolic phosphorylated phase of proteins, the long-axis polarisation cannot be maintained. In the two-dimensional elliptical geometry the diffusive length scale of the cytosolic dephosphorylation (binding-reactivation) process with respect to the cell size selects the stable polarisation axis. Above a certain threshold of this length scale the steady state polarisation aligns with the long axis. However, as the phosphorylated (inactive) phase can be diluted by a reservoir of binding-active proteins, also the total number of proteins also plays a role in axis alignment. Specifically, the ratio of total protein numbers with different functions, i.e. for the PAR system the ratio of antagonistic versus scaffold protein numbers, affects axis alignment significantly.

In three-dimensional ellipsoidal geometry we find, that an additional factor changes the long-term alignment of the polarisation. The initial polarisation axis is still selected by the dephosphorylation process and cytosolic diffusion. However, for the long term, i.e. when steady state is reached, the pattern always aligns with the long axis in an elongated prolate spheroidal cell. We could identify and validate numerically that a flux and interface minimisation is the reason for this phenomenon. The investigation of membrane and overall flux of different polarisation alignment in different three-dimensional geometries showed that the interface between the aPAR and pPAR domains on the membrane are the regions with the highest flux. The total flux, which is obtained by integration, is minimised as soon as these interfaces are minimised at steady state. In prolate spheroidal geometry with a ratio of long and short axis above a certain threshold and with a short-lasting inactive phase, an initial short axis polarisation develops but turns into steady state long-axis polarisation due to the interface minimising mechanism. In conclusion, two mechanisms for polarisation alignment compete in three-dimensional geometry: the local availability of binding proteins dictated by the membrane-to-bulk ratio, protein numbers, and inactive phases of proteins versus the global process of flux and interface minimisation.

6.1.2 Discussion of the PAR system compared to the Min protein system

The Min reaction-diffusion system in *E. coli* has been studied in depth in our group [13, 27, 35, 36, 38, 76, 77]. Pattern formation by the Min system has also been studied by the internship student *Laura Kern* whom I and *Laeschkir Würthner* supervised. By comparing my results for the PAR system with the findings in our group for the Min system, one can identify several similar features:

- Both systems comprise recruiting and antagonistic reactions in the protein network which are key to pattern domain formation on membranes. For the PAR system it is hetero-dimerisation among aPARs and mutual antagonism between aPARs and pPARs, while in the Min system it is self-recruitment of MinD and recruitment of MinE combined with an antagonistic detachment via hydrolysis of the MinDE

dimer induced by MinE. A balance of antagonistic rates is not only key to cell polarisation in the PAR system, but also in the Min system the ratio of MinD versus MinE recruitment rates is decisive for pattern formation [35].

- The balance of antagonistic processes does not only in the PAR system rely on ratios of aPAR and pPAR protein numbers but also in the Min system the ratio of MinE to MinD protein numbers dictates if patterns form.
- An inactive (phosphorylated) phase does not only exist in the PAR system, but also plays an important role in the Min system. Here, MinD undergoes a nucleotide exchange and is inactive for binding in its ADP-bound form [35]. Furthermore, recent findings of *in silico* and *in vitro* investigations [77] have pointed out that also a conformational switch of MinE, i.e. another type of inactive phase, increases the robustness of Min pattern formation against changes in protein numbers.
- While in this work it is shown that PAR proteins sense the geometry by the membrane-to-bulk ratio, also the Min system has been shown to adapt to the geometry via this ratio [36].
- In both protein systems cell polarisation appears as a minimal pattern unit. While in *C. elegans* the PAR system exhibits a stationary pattern during the polarisation maintenance phase, the Min system (*in vivo*) exhibits a dynamic equilibrium of pole to pole oscillations which appear on time average like a polarised pattern in the rod-shaped *E. coli* bacterium.
- The analysis of both systems shows that the coupling between membrane and cytosol counts for membrane patterning. The cytosolic processes are unignorable when considering the full cellular geometry [27, 32, 35, 36].

Taken together, the PAR and the Min system are both well studied paradigmatic systems for protein self-organisation. While the Min system has been studied thoroughly in explicit geometries, this was still missing for the PAR system. Hence, my work aims to fill this gap and improve our knowledge and intuition for other pattern forming systems in geometry.

6.2 Theoretical outlook

From the results in this thesis I gained ideas for future theoretical projects. Many ideas arose from extending the model to understand the *C. elegans* zygote development, but most also have the potential to be generalised to a class of systems. In the following subsections these ideas are presented in detail. As an overview, all suggestions can be divided into several categories:

1. More details in the PAR reaction-diffusion model: There is evidence of some more protein interactions in the PAR reaction-diffusion system. The model presented here could be extended to understand additional phenomena, such as bipolar patterns, as well as redundant mechanisms for PAR polarisation.

2. Interaction with mechanical and hydrodynamic mechanisms: The PAR system interacts with the actomyosin network and the centrosomes, which provide triggers for polarisation establishment. The integration of further mechanical and hydrodynamic (accompanied by additional chemical) cues from the actomyosin network and the centrosome into a theoretical model could be insightful to understanding the detailed development of *C. elegans*.
3. Interaction of the PAR reaction-diffusion system with a deforming geometry: During polarisation establishment in the *C. elegans* zygote its cortex ruffles. Thus, the PAR system is a great example to study a reaction-diffusion system in a deforming geometry.
4. Derivation of the flux and corresponding interface minimisation in the here presented PAR model with the help of a flux functional: The flux and interface minimisation which we studied numerically might be enhanced further, if a flux functional can be found and minimised.

6.2.1 Details in the PAR reaction-diffusion model

Recently, Klinkert et al. found that *C. elegans* zygotes lacking of centrosomes or depleted of the Aurora A kinase AIR-1 establish a bipolar pattern [114]. Additionally to AIR-1 depletion, they investigated deformed (triangular) embryos. In these triangularly shaped embryos they found that pPAR domains are located in highly curved regions. These phenomena can be analysed with the help of a small extension of the model proposed in this thesis. The PAR model introduced in this work solely includes some details of recruitment among aPARs. However, it was suggested that also PAR-2 might promote its own recruitment [106]. pPAR self-recruitment could be easily introduced to the model. I would also expect an investigation of the extended model in elliptical geometry to reveal large parameter regimes, where a bipolar pattern with a pPAR domain at each pole establishes. This expectation comes from studying the second even mode in elliptical geometry (for explanation of the second even mode see chapter 3 and my publication printed in chapter 4) which in general can become unstable before other modes, especially when recruitment is present (see also [36]). As illustrated in chapter 3, the second even mode in elliptical geometry resembles a bipolar pattern with one protein domain of the same species at each pole.

I also expect to find more interesting features when integrating more details to the aPAR kinetics. As also mentioned in chapter 5, there is evidence that PAR-3, the scaffold protein, oligomerises on the membrane. While this PAR-3 clustering appears to be suppressed during maintenance phase [112], it might also play a role for an efficient polarisation establishment.

Hence, the group of aPARs could be modelled with an additional scaffold and antagonism activating protein species. It has been suggested that the PAR-6/PKC-3 complex is recruited to the membrane via the scaffold PAR-3 and also binds independently to Cdc42 [115]. Furthermore, it has been proposed that PKC-3 is inactive as

a kinase when bound to PAR-3, i.e. it does not phosphorylate other proteins, but it becomes active once it starts binding to Cdc42 [55, 69].

6.2.2 Interaction with mechanical and hydrodynamic mechanisms

Integration of Cdc42 into a model is tightly related to a GTPase activating protein (GAP) called Chin-1, which down-regulates Cdc42 activity. Chin-1, in turn, interacts with the actomyosin network (mainly via cortical nonmuscle myosin, called NMY-2). Chin-1 clusters on the cortex, and was suggested to guide cortical ruffling [69, 116]. The details of cortical ruffling and specific chemical interactions of the actomyosin network with the PAR proteins are currently subject of experimental research. Models of these interactions have been proposed [31, 100], but have paid little attention to the isolated ability of the PAR reaction-diffusion network to polarise along the long axis of an ellipsoidal zygote. As the work presented here increased the understanding of the reaction-diffusion system alone but in geometry, it could now be combined with a model of a contracting actomyosin network. The interaction of both elements would be either modelled effectively, or even in detail by introducing species like Chin-1 and NMY-2.

6.2.3 The PAR reaction-diffusion system in a deforming geometry

Two colleagues of mine in the Frey work group, *Laeschkir Würthner* and *Andriy Goychuk*, have recently developed a framework to study reaction-diffusion systems living on and interacting with deforming surfaces (publication in preparation). They are currently working out applications to this framework. I took part in discussions when the framework was developed and collected ideas how to apply it to the PAR system in *C. elegans*. A partly similar computational model has been suggested by Mietke et al to investigate "the geometry of deforming materials and active processes" [117].

The idea behind *Laeschkir Würthner's* and *Andriy Goychuk's* framework lies in the coupling of the normal speed of deformation with the protein densities. As the reaction-diffusion system develops a pattern, local densities change. This, in turn, has an impact on the deformation. E.g. with a rigorous parameterisation of a one-dimensional deformable line they could calculate the deformation behaviour of this line interacting with a species diffusing on the line.

For the process of cortical ruffling in the *C. elegans* zygote the framework provides an exciting ansatz for future work. As a start, one could implement the PAR reaction-diffusion model on a deformable, one-dimensional line. As aPARs were reported to interact with the cortex (via Chin-1 and NMY-2), the aPAR density could be coupled to the normal speed of the deforming surface. In the real zygote aPARs are released at a small region around the centrosome, at first. This could be introduced as a point like perturbation of an initially uniform aPAR density on the deforming model surface. A study of the dynamics, which is induced by the coupling of aPARs and the surface, could very likely shed light on cortical ruffling in the anterior half of the

zygote. Different coupling terms between density and the normal speed of deformation should be investigated to identify possible mechanisms of the cortical ruffling and flow in the real zygote.

6.2.4 Flux and interface minimisation

While the result of flux minimisation leading to interface minimisation of the PAR system in three-dimensional cell geometries was proven numerically, this could be analysed in a follow-up project using a different, more mathematically rigorous approach. The idea would be to find a flux functional corresponding to the reaction-diffusion system. In the past, Allen-Cahn equations [118], i.e. specific reaction-diffusion equations which can be derived as the gradient flow of a Ginzburg-Landau free energy functional and which originally described the phase separation in a multi-component alloy, have been used to describe cellular reaction-diffusion systems [119], also the PAR system [42]. However, as Allen-Cahn equations are non-conserved this does not match the PAR reaction-diffusion system presented here. For the PAR system finding a flux functional and minimising it, could still deepen our understanding about why the flux and, as we showed consequently, the interface length are minimised by the PAR system.

6.3 Experimental outlook

The first step towards proving a model suitable is making qualitative predictions. An example of such a prediction could be "a phosphorylated phase leads to long axis polarisation from onset on". While experimental and theoretical results are usually more easily comparable on a qualitative level, e.g. the investigation if there is a phosphorylated phase, a quantitative comparison often needs an advanced plan. A theoretical model should produce testable results. For this, the people developing the theory need to know the capacity of the lab regarding which techniques are at hand and can realistically be developed on the time scales of a doctoral study. As I have only worked in the lab for five weeks, I would not presume to know for sure which experiments on the PAR system are possible on the long run. However, from the perspective of having worked in depth on the PAR system from the theoretical side coupled with some lab experience, I would like to suggest some follow-up experiments.

6.3.1 Suggestions for experiments

Our findings in chapter 4 could be tested experimentally. I predict several key control parameters that affect the axis selection, and can suggest several *in vitro* and *in vivo* studies. Provided that one is at some point able to purify all PAR proteins, an *in vitro* setup would be a breakthrough to compare experiment and theory. To investigate pattern dependencies on the membrane-to-cytosolic-bulk ratios, an *in vitro* setup could be comprised of a flat membrane, buffer (cytosol) including the PAR proteins (*PAR-3*, *PAR-6*, *PKC-3* and *PAR-1*, *PAR-2*) and an exclusive volume, such as a stamp. In this

setup, one should be able to observe a dependency of stable interfaces of *PAR* clusters on several experimental parameters:

- the viscosity of the buffer, which determines the speed of cytosolic diffusion
- the cytosolic phosphatase concentration, which determines the rate of dephosphorylation in the cytosol
- and the ratios of *PAR* proteins in the system.

A *minimal in vitro cell* would also offer a suitable, if more elaborate, setup. It would be comprised of an ellipsoidal membrane, buffer, and the *PAR* proteins. The same parameters as in the flat environment could be varied. An artificial slowing of cytosolic diffusion (obtained by increasing the buffer viscosity) should lead to a switch of the polarity axis.

For the *PAR* system, *in vivo* investigations have been established for decades now. Thus, we suggest the following experiments in a living one-cell state of the *C. Elegans* embryo.

- The model predicts that an increased number of *PAR-3* and *PAR-6* (such as A_1 in the model) destabilise long axis polarisation in favour of short axis polarisation. This might be possible to check via over-/underexpression.
- As *C. Elegans* zygotes survive some deformations (as e.g. performed by Klinkert et al [114]), deforming to different oblate and prolate spheroidal shapes would check our predictions made in chapter 4 for these differently shaped model systems.

However, in order to only investigate the ability of the *PAR* system to maintain polarity, a deactivation of the actomyosin network might be necessary. Additional difficulties might lie in the interaction of other polarity pathways. Current research reveals pathways depending on other proteins such as *CHIN-1*, *LGL-1* and *Cdc42*.

Altogether, *in vitro* or *in vivo* experimental investigations could continue to shed light on the interplay of geometry and the kinetics of *PAR* proteins.

Bibliography

- [1] J. Reinitz. Pattern formation. *Nature* **482**(7386), 464, 2012. DOI: 10.1038/482464a.
- [2] G. Moreno-Bueno, F. Portillo and A. Cano. Transcriptional regulation of cell polarity in EMT and cancer. *Oncogene* **27**(55), 6958–6969, 2008. DOI: 10.1038/onc.2008.346.
- [3] S. Kondo and T. Miura. Reaction-Diffusion Model as a Framework for Understanding Biological Pattern Formation. *Science* **329**(5999), 1616–1620, 2010. DOI: 10.1126/science.1179047.
- [4] M. F. Weber *et al.* Chemical warfare and survival strategies in bacterial range expansions. *J R Soc Interface* **11**(96), 20140172, 2014. DOI: 10.1098/rsif.2014.0172. eprint: <https://royalsocietypublishing.org/doi/pdf/10.1098/rsif.2014.0172>.
- [5] S. Zonies, F. Motegi, Y. Hao and G. Seydoux. Symmetry breaking and polarization of the *C. elegans* zygote by the polarity protein PAR-2. *Development* **137**(10), 1669–1677, 2010. DOI: 10.1242/dev.045823.
- [6] S. Kretschmer, K. Zieske and P. Schwille. Large-scale modulation of reconstituted Min protein patterns and gradients by defined mutations in MinE’s membrane targeting sequence. *PLoS One* **12**(6), e0179582–e0179582, 2017. DOI: 10.1371/journal.pone.0179582.
- [7] F. Zhang, Y. Wen and X. Guo. CRISPR/Cas9 for genome editing: progress, implications and challenges. *Hum Mol Genet* **23**(R1), R40–R46, 2014. DOI: 10.1093/hmg/ddu125. eprint: <https://academic.oup.com/hmg/article-pdf/23/R1/R40/9457639/ddu125.pdf>.
- [8] P. Schwille. Bottom-Up Synthetic Biology: Engineering in a Tinkerer’s World. *Science* **333**(6047), 1252–1254, 2011. DOI: 10.1126/science.1211701. eprint: <https://science.sciencemag.org/content/333/6047/1252.full.pdf>.
- [9] V. Noireaux and A. P. Liu. The New Age of Cell-Free Biology. *Annu Rev Biomed Eng* **22**(1) PMID: 32151150, null, 2020. DOI: 10.1146/annurev-bioeng-092019-111110. eprint: <https://doi.org/10.1146/annurev-bioeng-092019-111110>.
- [10] S. H. Strogatz. *Nonlinear Dynamics and Chaos*. 1994. DOI: 10.1063/1.2807947. arXiv: 1107.1180.
- [11] D. M. Abrams, R. Mirollo, S. H. Strogatz and D. a. Wiley. Solvable model for chimera states of coupled oscillators. *Phys Rev Lett* **101**(August), 1–4, 2008. DOI: 10.1103/PhysRevLett.101.084103. arXiv: 0806.0594.

- [12] M. Cross and H. Greenside. *Pattern Formation and Dynamics in Nonequilibrium Systems*. Cambridge University Press, 2009. DOI: 10.1017/CBO9780511627200.
- [13] J. Halatek and E. Frey. Rethinking pattern formation in reaction-diffusion systems. *Nat Phys* **14**(5), 507–514, 2018. DOI: 10.1038/s41567-017-0040-5.
- [14] A. Turing. The chemical basis of morphogenesis. *Philos Trans R Soc Lond B Biol Sci* **237**(641), 37–72, 1952. DOI: 10.1098/rstb.1952.0012.
- [15] A. Gierer and H. Meinhardt. A theory of biological pattern formation. *Kybernetik* **12**(1), 30–39, 1972. DOI: 10.1007/BF00289234.
- [16] C. Nüsslein-Volhard and E. Wieschaus. Mutations affecting segment number and polarity in *Drosophila*. *Nature* **287**(5785), 795–801, 1980. DOI: 10.1038/287795a0.
- [17] W. Driever and C. Nüsslein-Volhard. A gradient of bicoid protein in *Drosophila* embryos. *Cell* **54**(1), 83–93, 1988. DOI: 10.1016/0092-8674(88)90182-1.
- [18] V. V. Yashin and A. C. Balazs. Pattern Formation and Shape Changes in Self-Oscillating Polymer Gels. *Science* **314**(5800), 798–801, 2006. DOI: 10.1126/science.1132412.
- [19] F. Wu, B. G. C. van Schie, J. E. Keymer and C. Dekker. Symmetry and scale orient Min protein patterns in shaped bacterial sculptures. *Nat Nanotechnol* **10**(8), 719–726, 2015. DOI: 10.1038/nnano.2015.126.
- [20] S. Tahirovic and F. Bradke. Neuronal polarity. *Cold Spring Harb Perspect Biol* **1**(3), a001644–a001644, 2009. DOI: 10.1101/cshperspect.a001644.
- [21] W. T. Gibson and M. C. Gibson. Chapter 4 Cell Topology, Geometry, and Morphogenesis in Proliferating Epithelia. *Curr Top Dev Biol*. Vol. 89. Curr Top Dev Biol. Academic Press, 2009, pp. 87–114. DOI: [https://doi.org/10.1016/S0070-2153\(09\)89004-2](https://doi.org/10.1016/S0070-2153(09)89004-2).
- [22] M. S. Bretscher. On the shape of migrating cells — a ‘front-to-back’ model. *Journal of Cell Science* **121**(16), 2625–2628, 2008. DOI: 10.1242/jcs.031120. eprint: <https://jcs.biologists.org/content/121/16/2625.full.pdf>.
- [23] S. J. Altschuler, S. B. Angenent, Y. Wang and L. F. Wu. On the spontaneous emergence of cell polarity. *Nature* **454**(7206), 886–889, 2008. DOI: 10.1038/nature07119.
- [24] B. Klünder, T. Freisinger, R. Wedlich-Söldner and E. Frey. GDI-Mediated cell polarization in yeast provides precise spatial and temporal control of Cdc42 signaling. *PLoS Comput Biol* **9**(12), 2013. DOI: 10.1371/journal.pcbi.1003396.
- [25] T. Freisinger *et al.* Establishment of a robust single axis of cell polarity by coupling multiple positive feedback loops. *Nat Commun* **4**(1), 1807, 2013. DOI: 10.1038/ncomms2795.
- [26] N. W. Goehring, C. Hoegge, S. W. Grill and A. Hyman. PAR proteins diffuse freely across the anterior-posterior boundary in polarized *C. elegans* embryos. *J Cell Biol* **193**(3), 583–594, 2011. DOI: 10.1083/jcb.201011094.

- [27] F. Wu *et al.* Multistability and dynamic transitions of intracellular Min protein patterns. *Mol Syst Biol* **12**(6), 873, 2016.
- [28] I. R. Graf and E. Frey. Generic Transport Mechanisms for Molecular Traffic in Cellular Protrusions. *Phys Rev Lett* **118**, 128101, 2017. DOI: 10.1103/PhysRevLett.118.128101.
- [29] S. Bergeler and E. Frey. Regulation of Pom cluster dynamics in *Myxococcus xanthus*. *PLoS Comput Biol* **14**(8), e1006358–e1006358, 2018. DOI: 10.1371/journal.pcbi.1006358.
- [30] D. Schumacher *et al.* The PomXYZ Proteins Self-Organize on the Bacterial Nucleoid to Stimulate Cell Division. *Dev Cell* **41**(3), 299–314.e13, 2017. DOI: 10.1016/j.devcel.2017.04.011.
- [31] N. W. Goehring *et al.* Polarization of PAR proteins by advective triggering of a pattern-forming system. *Science* **334**(6059), 1137–1141, 2011. DOI: 10.1126/science.1208619.
- [32] R. Geßele, J. Halatek, L. Würthner and E. Frey. Geometric cues stabilise long-axis polarisation of PAR protein patterns in *C. elegans*. *Nat Commun* **11**(1), 539, 2020. DOI: 10.1038/s41467-020-14317-w.
- [33] F. Brauns, J. Halatek and E. Frey. Phase-space geometry of reaction–diffusion dynamics. Preprint at arXiv:1812.08684 (2018), 2018.
- [34] P. Glock *et al.* Design of biochemical pattern forming systems from minimal motifs. *eLife* **8**, e48646, 2019. DOI: 10.7554/eLife.48646.
- [35] J. Halatek and E. Frey. Highly Canalized MinD Transfer and MinE Sequestration Explain the Origin of Robust MinCDE-Protein Dynamics. *Cell Rep* **1**(6), 741–752, 2012. DOI: 10.1016/j.celrep.2012.04.005.
- [36] D. Thalmeier, J. Halatek and E. Frey. Geometry-induced protein pattern formation. *Proc Natl Acad Sci USA* **113**(3), 548–553, 2016. DOI: 10.1073/pnas.1515191113.
- [37] M. C. Wigbers, F. Brauns, T. Hermann and E. Frey. Pattern localization to a domain edge. *Phys Rev E* **101**, 022414, 2020. DOI: 10.1103/PhysRevE.101.022414.
- [38] J. Halatek, F. Brauns and E. Frey. Self-organization principles of intracellular pattern formation. *Phil Trans B* **373**(1747), 2018. DOI: 10.1098/rstb.2017.0107.
- [39] B. J. Thompson. Cell polarity: models and mechanisms from yeast, worms and flies. *Development* **140**(1), 13–21, 2013. DOI: 10.1242/dev.083634. eprint: <https://dev.biologists.org/content/140/1/13.full.pdf>.
- [40] J. Chant and I. Herskowitz. Genetic control of bud site selection in yeast by a set of gene products that constitute a morphogenetic pathway. *Cell* **65**(7), 1203–1212, 1991. DOI: 10.1016/0092-8674(91)90015-q.

- [41] T. F. Fehm. Master Thesis: Symmetry Breaking in the Early C . *Elegans Zygote*. 2012.
- [42] A. T. Dawes and D. Iron. Cortical geometry may influence placement of interface between Par protein domains in early *Caenorhabditis elegans* embryos. *J Theor Biol* **333**, 27–37, 2013. DOI: 10.1016/j.jtbi.2013.04.024.
- [43] K. Zieske and P. Schwille. Reconstitution of self-organizing protein gradients as spatial cues in cell-free systems. *eLife* **3**, e03949, 2014. DOI: 10.7554/eLife.03949.
- [44] M. Iijima, Y. E. Huang and P. Devreotes. Temporal and Spatial Regulation of Chemotaxis. *Dev Cell* **3**(4), 469–478, 2002. DOI: [https://doi.org/10.1016/S1534-5807\(02\)00292-7](https://doi.org/10.1016/S1534-5807(02)00292-7).
- [45] A. Hutterer, J. Betschinger, M. Petronczki and J. A. Knoblich. Sequential Roles of Cdc42, Par-6, aPKC, and Lgl in the Establishment of Epithelial Polarity during *Drosophila* Embryogenesis. *Dev Cell* **6**(6), 845–854, 2004. DOI: <https://doi.org/10.1016/j.devcel.2004.05.003>.
- [46] B. Goldstein and I. G. Macara. The PAR proteins: fundamental players in animal cell polarization. *Dev Cell* **13**(5), 609–622, 2007. DOI: 10.1016/j.devcel.2007.10.007.
- [47] R. DL, B. T and M. BJ. Introduction to *C. elegans*.(33), 1997.
- [48] P. Goenczy. Asymmetric cell division and axis formation in the embryo. *Worm-Book*, 1–20, 2005. DOI: <https://dx.doi.org/10.1895/wormbook.1.30.1>.
- [49] K. J. Kemphues, J. R. Priess, D. G. Morton and N. Cheng. Identification of genes required for cytoplasmic localization in early *C. elegans* embryos. *Cell* **52**(3), 311–20, 1988.
- [50] K. J. Kemphues. PARsing Embryonic Polarity. *Cell* **101**(4), 345–348, 2000. DOI: 10.1016/S0092-8674(00)80844-2.
- [51] C. F. Lang and E. Munro. The PAR proteins: from molecular circuits to dynamic self-stabilizing cell polarity. *Development* **144**(19), 3405–3416, 2017. DOI: 10.1242/dev.139063.
- [52] F. Motegi and A. Sugimoto. Sequential functioning of the ECT-2 RhoGEF, RHO-1 and CDC-42 establishes cell polarity in *Caenorhabditis elegans* embryos. *Nat Cell Biol* **8**(9), 978–985, 2006. DOI: 10.1038/ncb1459.
- [53] S. Schonegg and A. A. Hyman. CDC-42 and RHO-1 coordinate acto-myosin contractility and PAR protein localization during polarity establishment in *C. elegans* embryos. *Development* **133**(18), 3507–3516, 2006. DOI: 10.1242/dev.02527.
- [54] E. Munro, J. Nance and J. R. Priess. Cortical flows powered by asymmetrical contraction transport PAR proteins to establish and maintain anterior-posterior polarity in the early *C. elegans* embryo. *Dev Cell* **7**(3), 413–424, 2004. DOI: 10.1016/j.devcel.2004.08.001.

- [55] J. Rodriguez *et al.* aPKC cycles between functionally distinct PAR protein assemblies to drive cell polarity. *Dev Cell* **42**(4), 400–415.e9, 2017. DOI: 10.1016/j.devcel.2017.07.007.
- [56] S.-C. Wang *et al.* Cortical forces and CDC-42 control clustering of PAR proteins for *Caenorhabditis elegans* embryonic polarization. *Nat Cell Bio* **19**(8), 988–995, 2017. DOI: 10.1038/ncb3577.
- [57] F. Motegi *et al.* Microtubules induce self-organization of polarized PAR domains in *Caenorhabditis elegans* zygotes. *Nat Cell Biol* **13**(11), 1361–7, 2011. DOI: 10.1038/ncb2354.
- [58] C. Hoege and A. A. Hyman. Principles of PAR polarity in *Caenorhabditis elegans* embryos. *Nat Rev Mol Cell Biol* **14**(5), 315–322, 2013. DOI: 10.1038/nrm3558.
- [59] J. Li *et al.* Binding to PKC-3, but not to PAR-3 or to a conventional PDZ domain ligand, is required for PAR-6 function in *C. elegans*. *Dev Biol* **340**(1), 88–98, 2010. DOI: 10.1016/j.ydbio.2010.01.023.
- [60] B. Li, H. Kim, M. Beers and K. Kemphues. Different domains of *C. elegans* PAR-3 are required at different times in development. *Dev Biol* **344**(2), 745–757, 2010. DOI: 10.1016/j.ydbio.2010.05.506.DIFFERENT.
- [61] Y. Tabuse *et al.* Atypical protein kinase C cooperates with PAR-3 to establish embryonic polarity in *Caenorhabditis elegans*. *Development* **125**, 3607–3614, 1998.
- [62] Y. Hao, L. Boyd and G. Seydoux. Stabilization of cell polarity by the *C. elegans* RING protein PAR-2. *Dev Cell* **10**(2), 199–208, 2006. DOI: 10.1016/j.devcel.2005.12.015.Stabilization.
- [63] B. Etemad-Moghadam, S. Guo and K. Kemphues. Asymmetrically distributed PAR-3 protein contributes to cell polarity and spindle alignment in early *C. elegans* embryos. *Cell* **83**(5), 743–752, 1995. DOI: 10.1016/0092-8674(95)90187-6.
- [64] J. L. Watts *et al.* par-6, a gene involved in the establishment of asymmetry in early *C. elegans* embryos, mediates the asymmetric localization of PAR-3. *Development* **122**(10), 3133–3140, 1996.
- [65] T.-J. Hung and K. J. Kemphues. PAR-6 is a conserved PDZ domain-containing protein that colocalizes with PAR-3 in *Caenorhabditis elegans* embryos. *Development* **126**(1), 127–135, 1999.
- [66] L. Boyd *et al.* PAR-2 is asymmetrically distributed and promotes association of P granules and PAR-1 with the cortex in *C. elegans* embryos. *Development* **122**(10), 3075–3084, 1996.
- [67] A. A. Cuenca *et al.* Polarization of the *C. elegans* zygote proceeds via distinct establishment and maintenance phases. *Development* **130**(7), 1255–1265, 2003.
- [68] A. Beatty, D. Morton and K. Kemphues. PAR-2, LGL-1 and the CDC-42 GAP CHIN-1 act in distinct pathways to maintain polarity in the *C. elegans* embryo. *Development* **140**(9), 2005–14, 2013. DOI: 10.1242/dev.088310.

- [69] A. Sailer *et al.* Dynamic Opposition of Clustered Proteins Stabilizes Cortical Polarity in the *C. elegans* Zygote. *Dev Cell* **35**(1), 131–142, 2015. DOI: 10.1016/j.devcel.2015.09.006.
- [70] I. Visco, C. Hoegge, A. A. Hyman and P. Schwille. In vitro reconstitution of a membrane switch mechanism for the polarity protein LGL. *J Mol Biol* **428**(24), 4828–4842, 2016. DOI: 10.1016/j.jmb.2016.10.003.
- [71] S. Kretschmer and P. Schwille. Pattern formation on membranes and its role in bacterial cell division. *Curr Opin Cell Biol* **38** Cell architecture, 52–59, 2016. DOI: <https://doi.org/10.1016/j.ceb.2016.02.005>.
- [72] D. M. Raskin and P. A. de Boer. Rapid pole-to-pole oscillation of a protein required for directing division to the middle of *Escherichia coli*. *Proc Natl Acad Sci U S A* **96**(9), 4971–4976, 1999. DOI: 10.1073/pnas.96.9.4971.
- [73] J. Lutkenhaus. Assembly Dynamics of the Bacterial MinCDE System and Spatial Regulation of the Z Ring. *Annu Rev Biochem* **76**(1), 539–562, 2007. DOI: 10.1146/annurev.biochem.75.103004.142652.
- [74] M. Ingerson-Mahar and Z. Gitai. A growing family: the expanding universe of the bacterial cytoskeleton. *FEMS Microbiol Rev* **36**(1), 256–266, 2012. DOI: 10.1111/j.1574-6976.2011.00316.x. eprint: <https://academic.oup.com/femsre/article-pdf/36/1/256/18129482/36-1-256.pdf>.
- [75] J. Lutkenhaus. The ParA/MinD family puts things in their place. *Trends Microbiol* **20**(9), 411–418, 2012. DOI: 10.1016/j.tim.2012.05.002.
- [76] L. Hassan. Master Thesis: How MinCDE-Proteins Self-Organize in Vivo and in Vitro for *Escherichia coli*. 2016.
- [77] J. Denk *et al.* MinE conformational switching confers robustness on self-organized Min protein patterns. *Proc Natl Acad Sci USA*, 2018. DOI: <https://dx.doi.org/10.1073/pnas.1719801115>.
- [78] J. Howard, S. W. Grill and J. S. Bois. Turing’s next steps: the mechanochemical basis of morphogenesis. *Nat Rev Mol Cell Biol* **12**(6), 392–398, 2011. DOI: 10.1038/nrm3120.
- [79] Z. Zhou and R. A. Van Gorder. Turing Instability and Colony Formation in Spatially Extended Rosenzweig–MacArthur Predator–Prey Models with Allochthonous Resources. *Bull Math Biol* **81**(12), 5009–5053, 2019. DOI: 10.1007/s11538-019-00667-0.
- [80] G. Meacci *et al.* Mobility of Min-proteins in *Escherichia coli* measured by fluorescence correlation spectroscopy. *Phys Biol* **3**(4), 255–263, 2006. DOI: 10.1088/1478-3975/3/4/003.
- [81] F. O. Bendezú *et al.* Spontaneous Cdc42 Polarization Independent of GDI-Mediated Extraction and Actin-Based Trafficking. *PLoS Biol* **13**(4), 1–30, 2015. DOI: 10.1371/journal.pbio.1002097.

- [82] P. K. Trong *et al.* Parameter-space topology of models for cell polarity. *New J Phys* **16**(6), 65009, 2014. DOI: 10.1088/1367-2630/16/6/065009.
- [83] A. T. Dawes and E. M. Munro. PAR-3 oligomerization may provide an actin-independent mechanism to maintain distinct par protein domains in the early *Caenorhabditis elegans* embryo. *Biophys J* **101**(6), 1412–1422, 2011. DOI: 10.1016/j.bpj.2011.07.030.
- [84] F. Tostevin and M. Howard. Modeling the Establishment of PAR Protein Polarity in the One-Cell *C. elegans* Embryo. *Biophys J* **95**(10), 4512–4522, 2008. DOI: 10.1529/biophysj.108.136416.
- [85] E. Bi and H.-O. Park. Cell Polarization and Cytokinesis in Budding Yeast. *Genetics* **191**(2), 347–387, 2012. DOI: 10.1534/genetics.111.132886. eprint: <https://www.genetics.org/content/191/2/347.full.pdf>.
- [86] J. B. Hurov, J. L. Watkins and H. Piwnica-Worms. Atypical PKC phosphorylates PAR-1 kinases to regulate localization and activity. *Philos Trans R Soc Lond B Biol Sci* **14**, 736–741, 2004. DOI: 10.1016/j.cub.2004.04.007.
- [87] H. Levine and W.-J. Rappel. Membrane-bound Turing patterns. *Phys Rev E* **72**, 061912, 2005. DOI: 10.1103/PhysRevE.72.061912.
- [88] G. Kokkorakis and J. Roumeliotis. Power series expansions for Mathieu functions with small arguments. *Math Comput* **70**, 1221–1235, 2001. DOI: 10.1090/S0025-5718-00-01227-8.
- [89] R. A. Larsen *et al.* Treadmilling of a prokaryotic tubulin-like protein, TubZ, required for plasmid stability in *Bacillus thuringiensis*. *Genes Dev* **21**(11), 1340–1352, 2007. DOI: 10.1101/gad.1546107.
- [90] J. P. Campanale, T. Y. Sun and D. J. Montell. Development and dynamics of cell polarity at a glance. *J Cell Sci* **130**(7), 1201–1207, 2017. DOI: 10.1242/jcs.188599.
- [91] J.-g. Chiou, M. K. Balasubramanian and D. J. Lew. Cell polarity in yeast. *Annu Rev Cell Dev Biol* **15**, 365–391, 2017. DOI: <https://dx.doi.org/10.1146/annurev.cellbio.15.1.365>.
- [92] J. Roignot, X. Peng and K. Mostov. Polarity in mammalian epithelial morphogenesis. *Cold Spring Harb Protoc* **33**, 2013. DOI: <https://dx.doi.org/10.1101/cshperspect.a013789>.
- [93] N. W. Goehring. PAR polarity: from complexity to design principles. *Exp Cell Res* **328**(2), 258–266, 2014. DOI: 10.1016/j.yexcr.2014.08.009.
- [94] F. Motegi and G. Seydoux. The PAR network: redundancy and robustness in a symmetry-breaking system. *Philos Trans R Soc Lond B Biol Sci* **368**(1629), 20130010, 2013. DOI: 10.1098/rstb.2013.0010.
- [95] D. P. Hill and S. Strome. An analysis of the role of microfilaments in the establishment and maintenance of asymmetry in *Caenorhabditis elegans* zygotes. *Dev Biol* **125**(1), 75–84, 1988. DOI: 10.1016/0012-1606(88)90060-7.

- [96] C. R. Cowan and A. A. Cowan. Centrosomes direct cell polarity independently of microtubule assembly in *C. elegans* embryos. *Nature* **431**(7004), 92–96, 2004. DOI: 10.1038/nature02825.
- [97] Z. Petrášek *et al.* Characterization of protein dynamics in asymmetric cell division by scanning fluorescence correlation spectroscopy. *Biophys J* **95**(11), 5476–5486, 2008. DOI: 10.1529/biophysj.108.135152.
- [98] S. Schonegg, A. T. Constantinescu, C. Hoegge and A. A. Hyman. The Rho GTPase-activating proteins RGA-3 and RGA-4 are required to set the initial size of PAR domains in *Caenorhabditis elegans* one-cell embryos. *Proc Natl Acad Sci USA* **104**(38), 14976–14981, 2007. DOI: 10.1073/pnas.0706941104.
- [99] C. Schenk, H. Bringmann, A. A. Hyman and C. R. Cowan. Cortical domain correction repositions the polarity boundary to match the cytokinesis furrow in *C. elegans* embryos. *Development* **137**(10), 1743–1753, 2010. DOI: 10.1242/dev.040436.
- [100] P. Gross *et al.* Guiding self-organized pattern formation in cell polarity establishment. *Nat Phys* **15**(3), 293–300, 2019. DOI: 10.1038/s41567-018-0358-7.
- [101] G. C. Kokkorakis and J. A. Roumeliotis. Power series expansions for Mathieu Functions with small arguments. *Math Comput* **70**(235), 1221–1235, 2000.
- [102] F. B. Robin, W. M. McFadden, B. Yao and E. M. Munro. Single-molecule analysis of cell surface dynamics in *Caenorhabditis elegans* embryos. *Nat Methods* **11**(6), 677–682, 2014. DOI: 10.1038/nmeth.2928.
- [103] J. Nance and J. Zallen. Elaborating polarity: PAR proteins and the cytoskeleton. *Development*, 799–809, 2011. DOI: 10.1242/dev.053538.
- [104] M. Tokunaga, N. Imamoto and K. Sakata-Sogawa. Highly inclined thin illumination enables clear single-molecule imaging in cells. *Nat Methods* **5**(2), 159–161, 2008. DOI: 10.1038/nmeth1171.
- [105] Y. Sako. Imaging single molecules in living cells for systems biology. *Mol Sys Bio* **2**(1), 56, 2006. DOI: 10.1038/msb4100100.
- [106] Y. Arata *et al.* Cortical Polarity of the RING Protein PAR-2 Is Maintained by Exchange Rate Kinetics at the Cortical-Cytoplasmic Boundary. *Cell Rep* **16**(8), 2156–2168, 2016. DOI: 10.1016/j.celrep.2016.07.047.
- [107] A. Achilleos, A. M. Wehman and J. Nance. PAR-3 mediates the initial clustering and apical localization of junction and polarity proteins during *C. elegans* intestinal epithelial cell polarization. *Development* **137**(11), 1833–1842, 2010. DOI: 10.1242/dev.047647.
- [108] L. Timmons and A. Fire. Specific interference by ingested dsRNA. *Nature* **395**(6705), 854, 1998. DOI: 10.1038/27579.
- [109] D. T. Gillespie. Exact stochastic simulation of coupled chemical reactions. *J Phys Chem* **81**(25), 2340–2361, 1977.

- [110] D. T. Gillespie. Stochastic simulation of chemical kinetics. *Annual review of physical chemistry* **58**, 35–55, 2007. DOI: 10.1146/annurev.physchem.58.032806.104637.
- [111] C. Gardiner. *Stochastic Methods: A Handbook for the Natural and Social Sciences*. Vol. 4. Springer-Verlag, 2009.
- [112] D. J. Dickinson *et al.* A Single-Cell Biochemistry Approach Reveals PAR Complex Dynamics during Cell Polarization. *Dev Cel* **42**(4), 416–434.e11, 2017. DOI: <https://doi.org/10.1016/j.devcel.2017.07.024>.
- [113] L. Hubatsch. PhD Thesis: Interplay between Cell Size and Cell Polarity. 2018.
- [114] K. Klinkert *et al.* Aurora A depletion reveals centrosome-independent polarization mechanism in *Caenorhabditis elegans*. *eLife* **8**, e44552, 2019. DOI: 10.7554/eLife.44552.
- [115] M. Beers and K. Kemphues. Depletion of the co-chaperone CDC-37 reveals two modes of PAR-6 cortical association in *C. elegans* embryos. *Development* **133**(19), 3745–3754, 2006. DOI: 10.1242/dev.02544.
- [116] K. T. Kumfer *et al.* CGEF-1 and CHIN-1 Regulate CDC-42 Activity during Asymmetric Division in the *Caenorhabditis elegans* Embryo. *Mol Biol Cell* **21**(2), 266–277, 2010. DOI: 10.1091/mbc.e09-01-0060.
- [117] A. Mietke, F. Jülicher and I. F. Sbalzarini. Self-organized shape dynamics of active surfaces. *Proc Natl Acad Sci USA* **116**(1), 29–34, 2019. DOI: 10.1073/pnas.1810896115.
- [118] S. M. Allen and J. W. Cahn. A microscopic theory for antiphase boundary motion and its application to antiphase domain coarsening. *Acta Metallurgica* **27**(6), 1085–1095, 1979. DOI: [https://doi.org/10.1016/0001-6160\(79\)90196-2](https://doi.org/10.1016/0001-6160(79)90196-2).
- [119] M. Semplice *et al.* A Bistable Model of Cell Polarity. *PLoS One* **7**(2), 1–14, 2012. DOI: 10.1371/journal.pone.0030977.

Acknowledgements

I would like to thank all the people who supported me during my doctoral studies. First of all, I would like to express my deep gratitude to Erwin Frey for supervising me and giving me the opportunity to be part of his group. I very much enjoyed our discussions that helped me to proceed with the projects and to find new research directions. You also gave me the opportunity to take actively part in the research community, by having the chance to go to conferences, summer schools and meet invited guests. Furthermore, based on your instructions, I could strongly improve how to present science (in scientific papers, in a proposal or at a scientific conference) — Thank you very much!

I am very glad that I had the chance to be a member of the graduate school “Quantitative Biosciences Munich” (QBM). This school was an ideal start for me to conduct interdisciplinary research. In particular, I enjoyed networking with PhD students from different fields ranging from Medicine over Bioinformatics to Mathematics. For making this possible, I would like to thank Markus Hohle, Filiz Civril (former QBM organiser and teacher) and Mara Kieke (former QBM organiser) and all the others who have taken care of QBM.

Being a member of Erwin Frey’s group was a great experience. I really liked the open, communicative and supportive atmosphere in the group — a warm thanks to all the present and previous members of Erwin’s chair for making it such a great environment full of curiosity. For plenty of helpful discussions I would like to thank very much in particular: Laeschkir Hassan, Florian Gartner, and Isabella Graf.

A special thanks also goes to Lars Hubatsch, who taught me during a summer school in the lab to dissect *C. elegans* worms, and inspect their embryos using fluorescence microscopy. He was always open to answer my experimental questions even years after that summer school.

Finally, I would like to express a cordial thanks to my parents, Diana Gebele, Michael Kramhöller, and also my stepfather, Detlef Pietrowski, who always supported me with a lot of love, no matter what would happen, and their deep belief in my skills. My mum always stands behind me as a rock in the turbulent waters, is always reachable and listens. Furthermore, I want to emphasise that my father with his great and creative riddles initialised my interest for digging deep into problems and to solve them however long it may take. This ability of problem solving helped me in many situations and strengthened the belief in myself from early childhood on. A very special thanks goes also to my stepfather who really set to spark off towards science, by discussing with me about scientific questions and related philosophical and ethical issues already when I was a teenager. He was the one who taught me to think critical. A very special thanks goes to Philipp Schenk for your love, continuous support and encouragement.